AN ABSTRACT OF THE DISSERTATION OF

Margaret L. Palmsten for the degree of Doctor of Philosophy in Oceanography

presented on December 9, 2010.

Title:

Dune Erosion Models and Swash Zone Kinematics from Remote Video Observations

Abstract approved:

_____

Robert A. Holman

    The subaerial beach, composed of sand dunes and the foreshore, provides a

natural buffer zone between vulnerable land and the dissipation of storm wave energy

due to wave breaking. The natural beauty of this region is attractive to people, and as

a result, significant investment has been placed in this relatively unstable strip between

land and water. During storms, when water levels and waves exceed the base of the

dune and the dunes are vulnerable to erosion, development and ecosystems landward

of the dune are at risk. Ideally, predictive models would forecast potential dune

erosion, allowing appropriate management response.

    One class of existing dune erosion models is based on assumed avalanching

once foreshore slopes exceed a user defined maximum value, although vertical or even

Report Documentation Page

Public reporting burden for the collection of information is estimated to average 1 hour per response, including the time for reviewing instructions, searching existing data sources, gathering and maintaining the data needed, and completing and reviewing the collection of information. Send comments regarding this burden estimate or any other aspect of this collection of information, including suggestions for reducing this burden, to Washington Headquarters Services, Directorate for Information Operations and Reports, 1215 Jefferson Davis Highway, Suite 1204, Arlington VA 22202-4302. Respondents should be aware that notwithstanding any other provision of law, no person shall be subject to a penalty for failing to comply with a collection of information if it does not display a currently valid OMB control number.

1. REPORT DATE	2. REPORT TYPE	3. DATES COVERED
09 DEC 2010		**00-00-2010 to 00-00-2010**

4. TITLE AND SUBTITLE	5a. CONTRACT NUMBER
Dune Erosion Models and Swash Zone Kinematics from Remote Video Observations	5b. GRANT NUMBER
	5c. PROGRAM ELEMENT NUMBER

6. AUTHOR(S)	5d. PROJECT NUMBER
	5e. TASK NUMBER
	5f. WORK UNIT NUMBER

7. PERFORMING ORGANIZATION NAME(S) AND ADDRESS(ES)	8. PERFORMING ORGANIZATION REPORT NUMBER
Oregon State University,Corvallis,OR,97331	

9. SPONSORING/MONITORING AGENCY NAME(S) AND ADDRESS(ES)	10. SPONSOR/MONITOR'S ACRONYM(S)
	11. SPONSOR/MONITOR'S REPORT NUMBER(S)

12. DISTRIBUTION/AVAILABILITY STATEMENT
Approved for public release; distribution unlimited

13. SUPPLEMENTARY NOTES

14. ABSTRACT

The subaerial beach, composed of sand dunes and the foreshore, provides a natural buffer zone between vulnerable land and the dissipation of storm wave energy due to wave breaking. The natural beauty of this region is attractive to people, and as a result, significant investment has been placed in this relatively unstable strip between land and water. During storms, when water levels and waves exceed the base of the dune and the dunes are vulnerable to erosion, development and ecosystems landward of the dune are at risk. Ideally, predictive models would forecast potential dune erosion, allowing appropriate management response. One class of existing dune erosion models is based on assumed avalanching once foreshore slopes exceed a user defined maximum value, although vertical or even overhanging dunes frequently occur in nature, suggesting that a maximum slope is not a universal parameterization. Another approach relates the volume of eroded sediment to the normal force of impact via an empirical coefficient. However, neither of these approaches addresses the fundamental physics controlling dune erosion. The objective of this dissertation is two-fold. The primary objective is to improve our understanding of the physics driving dune erosion and develop new predictive models. The secondary objective is to develop innovative new methods for studying the dune and foreshore using remotely sensed observations that can provide the data needed to improve our understanding of the processes. The first section of this dissertation focuses on developing a stereo video method for making quantitative observations of dune erosion at higher spatial and temporal resolution than traditional measurements allow. Resolution of the technique is 0.1 m in the horizontal and 0.04 m in the vertical. Errors were on the order of 0.02 m to 0.08 m (1 to 2 pixels) when compared with in situ surveys. Newly developed confidence intervals accurately quantified observed scatter from the stereo technique. The method was implemented in a large-scale wave flume experiment designed to reproduce a storm hydrograph. The new observations of dune morphology were used to improve an existing dune erosion model, accounting for the interaction between fluid and sediment by relating the momentum flux from waves onto the dune directly to eroded volume. We improved parameterizations for offshore wave forcing in the model based on an assumed normal distribution of swash on dunes. The model reproduced 64% of the observed variance in observations given known forcing at the dune and 55% of observed variance based on the new parameterizations of offshore forcing.

15. SUBJECT TERMS

16. SECURITY CLASSIFICATION OF:			17. LIMITATION OF ABSTRACT	18. NUMBER OF PAGES	19a. NAME OF RESPONSIBLE PERSON
a. REPORT **unclassified**	b. ABSTRACT **unclassified**	c. THIS PAGE **unclassified**	**Same as Report (SAR)**	**165**	

overhanging dunes frequently occur in nature, suggesting that a maximum slope is not a universal parameterization. Another approach relates the volume of eroded sediment to the normal force of impact via an empirical coefficient. However, neither of these approaches addresses the fundamental physics controlling dune erosion.

The objective of this dissertation is two-fold. The primary objective is to improve our understanding of the physics driving dune erosion and develop new predictive models. The secondary objective is to develop innovative new methods for studying the dune and foreshore using remotely sensed observations that can provide the data needed to improve our understanding of the processes.

The first section of this dissertation focuses on developing a stereo video method for making quantitative observations of dune erosion at higher spatial and temporal resolution than traditional measurements allow. Resolution of the technique is 0.1 m in the horizontal and 0.04 m in the vertical. Errors were on the order of 0.02 m to 0.08 m (1 to 2 pixels) when compared with in situ surveys. Newly developed confidence intervals accurately quantified observed scatter from the stereo technique.

The method was implemented in a large-scale wave flume experiment designed to reproduce a storm hydrograph. The new observations of dune morphology were used to improve an existing dune erosion model, accounting for the interaction between fluid and sediment by relating the momentum flux from waves onto the dune directly to eroded volume. We improved parameterizations for offshore wave forcing in the model based on an assumed normal distribution of swash on

dunes. The model reproduced 64% of the observed variance in observations given known forcing at the dune and 55% of observed variance based on the new parameterizations of offshore forcing.

The second section describes the development of a new dune erosion model based on observations from the dune erosion experiment. In the new model, the dune slumps when the weight of the dune plus the weight of water infiltrated from swash exceeds the resisting strength of the sediment. Eroded volume of sediment is then equal to the infiltrated volume of sediment. Infiltration was modeled using Darcy's Law substituted into the continuity equation. The resulting model explains 72% of the observed variance in eroded volume.

The final section of this dissertation describes a method for observing swash kinematics by tracking foam on the swash. This technique is useful for making observations on the foreshore where in situ instrumentation is difficult to maintain and significantly alters the flow to be measured. The method was compared with in situ observations collecting using an acoustic Doppler velocimeter. Coherence squared between observations and model was between 0.8 and 0.9 over the energetic frequencies, suggesting that this method would be useful for studying hydrodynamic forcing of sediment transport in the foreshore region.

DUNE EROSION MODELS AND SWASH ZONE KINEMATICS FROM REMOTE
VIDEO OBSERVATIONS

by

Margaret L. Palmsten

A DISSERTATION

submitted to

Oregon State University

in partial fulfillment of

the requirements for the

degree of

Doctor of Philosophy

Presented December 9, 2010

Commencement June 2011

Doctor of Philosophy dissertation of Margaret L. Palmsten presented on December 9, 2010

APPROVED:

_____

Major Professor, representing Oceanography

_____

Dean of the College of Oceanic and Atmospheric Sciences

_____

Dean of the Graduate School

I understand that my dissertation will become part of the permanent collection of the Oregon State University libraries. My signature below authorizes release of my dissertation to any reader upon request.

_____

Margaret L. Palmsten, Author

ACKNOWLEDGEMENTS

My career, especially at Oregon State, has not been a solitary endeavor. First and foremost, I wish to thank my husband, Justin for supporting me the entire way. You were willing to move all the way across the country, just so I could go to graduate school. You gave your weekends, evenings, and vacations up so I could work. You have been here through the entire process, encouraging me with your words and actions when I needed reminding that I could do it. Thank you for all of your hard work, you deserve as much credit as I do for making it to the finish line.

The second person, who has been on the front lines of my dissertation for his whole life, is my wonderful son, Huck. You are a little smiling beacon that keeps me going. I hope that in some small way, your life is better because of my studies. Thank you for being patient and supportive while mom finishes her dissertation.

My parents, grandparents, and sisters are another component of the team that got me here. Mom and dad, thank you for encouraging me, and all your daughters, to pursue careers in science. Thanks for not letting me drop out of high school calculus class, as was the fashionable thing for girls to do. You instilled inquisitiveness and a drive to succeed that are absolutely necessary to get through graduate school. To both my grandmothers: you are both intelligent and resilient women who taught me that anything is possible if you choose to pursue it and supported me with your kind thoughts and words along the way. Allison and Kristi, my younger sisters, who are

the best role models I have ever had. I only hope I am as intelligent and hard working as you are.

So many friends have supported me along the way. My lab mates, Kristen and Joe. You guys are my teachers, my counselors, my friends. Hilary, you are a fantastic friend and scientist. I feel lucky to have a colleague like you. Chris, you for talked me through some stressful moments, and you always make me laugh by pushing the joke a little too far. Molly, we have been friends since 5th grade, and you are always there to encourage me and talk me though every life crisis I've had since then. My neighbors in Albany, especially John, DaNette, and Gavin, I have truly enjoyed sharing my life with you these last 5 years.

A number of scientists have mentored me along the way. I am especially thankful that these people have not only taught me about science, but taught me about life as well. Gregg Brooks and Dave Duncan at Eckerd College first got me excited about marine geology, and taught me that at the end of a long day of geology, there was always a nice, cool beer. Peter Howd, not only advised my master's degree, but was the reason I met my husband. Abby Sallenger, for teaching me about how to talk so that people will listen and getting me excited about applied coastal research, and always staying from the beginning to the end of my parties.

Once I got to Oregon State University, I was fortunate enough to be mentored by Rob and Tuba. You two are a dynamic duo. We have run the equivalent of at least the distance to Minnesota over the course my graduate career. Over that time, you

have pushed me to think and create new knowledge far beyond what I thought I was capable of doing.

In the CIL, John, you are a master of the Socratic method, you keep my data safe from harm and teach me about the ways of the world. After 6 years under your tutelage, there is nothing that scares me. I will always come back to visit you. To the other members of the CIL, each one of you has taught me and made me laugh. I would not have been able to do this without you. To Kathy, mother to all of us in the CIL, thank you for welcoming us, and taking care of us.

CONTRIBUTION OF AUTHORS

The three manuscripts making up this dissertation have been or will be submitted for publication. Chapter 2 was submitted for publication at Coastal Engineering. Linden Clarke was instrumental in early development of the stereo technique and Peter Ruggiero collected the in situ data for comparison with stereo observations. Chapter 3 will be submitted to the Journal of Geophysical Research shortly after I defend. Chapter 4 was published as a conference proceeding for the International Conference on Coastal Engineering 2006 in San Diego, CA. The method was developed based on ideas from Rob Holman, Todd Holland contributed video data, and Britt Raubenheimer contributed in situ observations.

TABLE OF CONTENTS

TABLE OF CONTENTS (Continued)

LIST OF FIGURES

LIST OF FIGURES (Continued)

LIST OF FIGURES (Continued)

LIST OF TABLES

DUNE EROSION MODELS AND SWASH ZONE KINEMATICS FROM REMOTE

VIDEO OBSERVATIONS

1. INTRODUCTION

1.1 Societal Motivation

Sand dunes are a ubiquitous feature of the world's coastlines (Figure 1.1).
They exist on all continents and at all latitudes (Martínez and Psuty, 2004). Much of
the United Sates coastline, including the east coast, Gulf coast, and Pacific Northwest,
is backed by sand dunes. Erosion of these dunes is an ongoing process as barrier
beaches adjust to changing waves and water levels.

From a societal prospective, beaches are important because they have long
been important for recreation (Sallenger, 2009) and the source of significant revenue
for coastal communities (Committee to Assess the U.S. Army Corps of Engineers
Water Resources Project Planning Procedures, 1999). Because sand dunes are
typically the highest point of elevation on a beach, they offer natural protection for
landward ecosystems, buildings, and infrastructure. As such, dunes have become an
important feature in coastal engineering.

When the combination of waves, storm surge, and tides exceed the base of the
dune, dunes are subject to erosion, and anything lying behind the dune is at risk for
damage. Therefore, understanding the physical processes driving dune erosion and
developing a predictive capability for modeling dune erosion is a societally relevant

endeavor, particularly as the hydrodynamic forcing of dune erosion may change with global climate change.

1.2 Dune Erosion Models

Several models exist for studying dune erosion. They range from simple models that may easily be applied over large areas of coastline with little computational effort to relatively complex models that may be applied over only small regions and short timescales because of their computational requirements. However, no single model fully captures the physical processes controlling dune erosion. In this section, I introduce three different approaches.

Sallenger (2000) described a storm impact scale, relating the total water level to the elevation of morphologic features on the beach as a method for characterizing dune erosion (Figure 1.2). Four regimes are defined based on these relationships, and Sallenger argues that within each regime the patterns and magnitude of erosion is unique. The first impact level is the swash regime where wave runup does not exceed the base of the dune, and there is no erosion of the dune. The second level is the collision regime where runup exceeds the base of the dune, and net erosion of the dune is observed. The third impact level is the overwash regime where runup exceeds the top of the dune and net sediment transport from the dune is directed landward. The final impact level, the inundation regime occurs when storm surge completely submerges the island, and net sediment transport from the dune is onshore. The dune is completely obliterated. While this approach provides a useful tool for estimating

the likelihood that dune erosion is possible, it does not directly address the physical processes causing dune erosion, estimate the magnitude of erosion, or account for the time dependence of wave forcing.

A second approach to modeling dune erosion is the wave force model, first proposed by Fisher and Overton (1986). In this model, the impact of waves normal to the dune face is linearly proportional to the volume of sand eroded from the dune. Larson et al. (2004) extended this approach to define forcing in terms of offshore wave conditions, and Erikson et al. (2007) combined this approach with a slope stability model for the specific case of overhanging dunes. Although this approach directly addresses the interaction between waves and eroded volume, the assumption that the volume of eroded sediment is dependent upon the normal force impacting the dune face is not obvious, since slumping is caused by the balance of forces acting along failure planes within the dune not on normal forces.

An alternative approach to studying dune erosion are process-based sediment transport models, where the physical processes believed to be driving cross-shore sediment transport are represented with a series of coupled models for waves, currents, and sediment transport . The most recent example of this type of model is XBeach (Roelvink et al., 2009b). These models have reached a high level of sophistication below the mean water level. However, in the swash zone, the region intermittently covered and exposed by waves, and on the dune, the processes driving sediment transport are not well quantified. The mechanism for dune erosion in these models is

either to extrapolate the transport based on model results at the mean water level, or to apply a user defined maximum beach slope, allowing the sediment to erode if the slope becomes steeper than the maximum slope.

1.3 A Data Starved Problem

Few observations of active dune erosion exist owing to the difficulty of collecting data under storm conditions. Traditional surveying techniques for measuring dune erosion require access to the beach on foot, and remote sensing methods like airborne lidar require calm conditions for flying. As a result, dune erosion is typically observed before and after a storm occurs, but no data is collected when waves are interacting with the dune.

In order to make observations of actively eroding dunes, observationalists have turned to large scale dune erosion laboratory experiments. Laboratory experiments provide the necessary observations, but current surveying techniques in the laboratory require stopping waves to make those observations. In most laboratory settings, a cross-shore profile of the beach is collected on average once per hour during the experiment (Dette et al., 2002; van Thiel de Vries et al., 2008). Increasing frequency or number of profiles becomes prohibitive due to time and cost constraints.

A related problem exists for making observations of velocity in the swash zone. Under storm conditions, it is impractical to make in situ observations due to exposure of instrumentation to large waves and rapid adjustment of the swash zone

sediments to wave forcing. Also the presence of instrumentation may significantly alter flow.

1.4 Dissertation Objective and Approach

The objective of this dissertation is two-fold. The first objective is to develop innovative methods for studying dune erosion that can lead to breakthroughs in our understanding of dune erosion processes. The second objective is to improve our understanding of the forces driving dune erosion, and incorporate those forces into a model.

In Chapter 2, a stereo video algorithm for observing dune erosion is developed based on established stereo theory. A new method for calculating error bars on stereo observations is also developed and implemented. Then, the stereo method is applied to a large scale laboratory experiment. Observations from the experiment are used to test parameterizations for wave forcing of dune erosion, and improve an existing wave force model for dune erosion.

The third chapter focuses on development of a new model for dune erosion based on observations from Chapter 2. The driving mechanism for dune erosion in this model is changes in slope stability based on wave driven infiltration of water into the dune. The newly developed model is then compared to observations from the experiment described in Chapter 2.

In the fourth chapter of this dissertation, a new method for estimating water velocity in the swash zone is developed and compared with in situ observations. This method could ultimately be applied to investigate the transport of sediment from the dune to the surf zone.
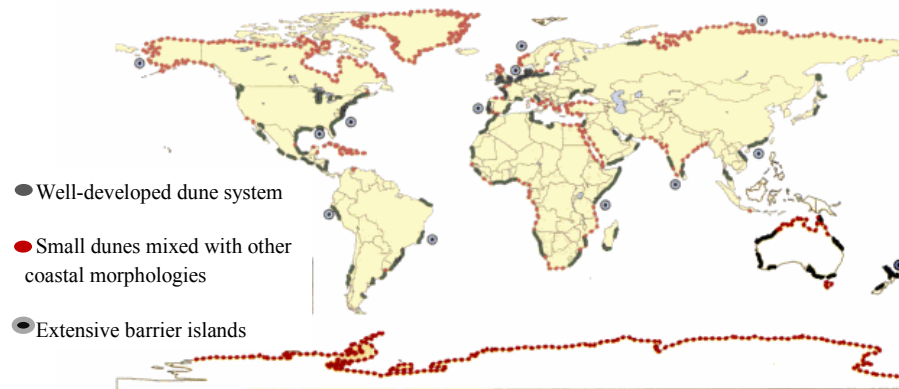
Figure 1.1 Map showing the distribution of sand dunes along the world's coastlines. Modified from Martinez and Psuty (2004).
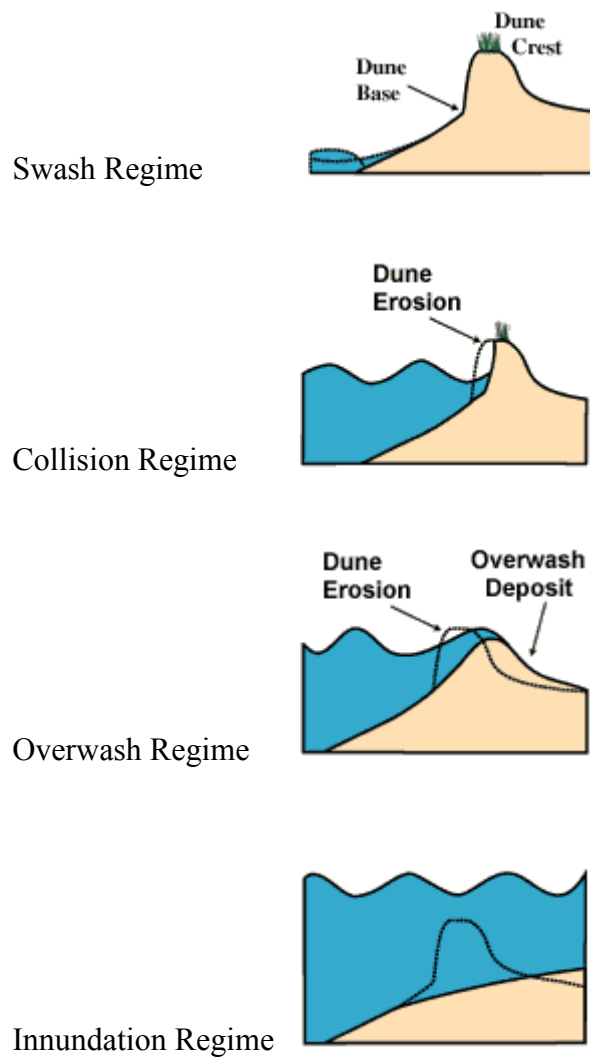
Figure 1.2 Definition sketch of the storm impact regimes. Modified from Sallenger (2000).

2. LABORATORY INVESTIGATION OF DUNE EROSION USING STEREO
   VIDEO

2.1 Abstract

Simple parameterizations of dune erosion are useful for forecasting erosion potential prior to an oncoming storm. Dune erosion may be parameterized in terms of the elevation of the total water level (composed of surge, tide, and wave runup) above the dune base and period of exposure of the dune to waves. In this work, we test several versions of this model using observations from a large wave tank experiment designed to model a storm hydrograph, and we develop a new method for acquiring the appropriate data with confidence intervals using stereo video techniques.

The new stereo method results in observations of dune morphology at higher spatial and temporal resolution than traditional survey methods allow. Resolution of the stereo technique was 0.1 m in the horizontal and 0.04 m in the vertical, and errors in stereo observations were on the order of 0.02 to 0.08 m (1 to 2 pixels) when compared with surveys and were accurately quantified with newly developed confidence intervals.

Observations from the stereo method were used to quantify wave runup and dune erosion. We tested a variety of runup statistics based on a Gaussian distribution of swash properties, and found that the most predictive statistic for dune erosion was the 16% exceedance elevation above the dune base, lower than the often used 2% exceedance value. We found that the parameterization of runup was sensitive to beach slope, and that the most accurate beach slope for predicting runup was from a

regression through the region of the beach profile defined by the mean water level plus one standard deviation of swash. The dune base retreated along a relatively constant trajectory that was half the initial beach slope. Finally, a simple model for dune erosion was tested and found to have good predictive skill given both measured and parameterized offshore forcing.

2.2. Introduction

Coastal sand dunes are known as the "first line of defense" against the combination of high water levels and large waves generated by extreme storms. When water levels overtop the dune crest, sensitive habitat and structures are at risk. In order to plan for and mitigate damage caused by extreme storms, a firm physical understanding of the interplay between fluid and sediment transport causing dune erosion must be developed. The matter is even more pressing in the face of the potential for higher waves (Ruggiero et al., 2010), and increased water levels (IPCC, 2007) and changing storm tracks caused by climate change (Graham and Diaz, 2001).

This paper has two objectives. Our primary goal is to test models and a number of concepts of dune erosion using data from a wave tank experiment in which forcing conditions mimicked a well-documented natural storm. Our second goal is to develop and test a new stereo-based approach that allows collection of high-resolution data without the interference normally associated with in situ sampling.

There are three classes of models that may be used for dune erosion. The simplest models include only the relationship between water level and specific dune

features, without including information about time dependent forcing or feedback with morphology. This is best illustrated by the Storm Impact Scaling (Sallenger, 2000) which defines a set of erosion risk conditions based simply on whether the height of the total water level exceeds the elevation of the dune base, z_b, (collision regime) or dune crest, z_c (overtopping regime). While erosion rate is not specified, it is assumed that magnitude of erosion is strongly dependent on regime so that regime identification will be an adequate indicator of net erosion.

The total water level includes contributions from tide and surge that can be computed using regional models, and a contribution from wave runup. Sallenger (2000) suggested the use of the 2% exceedance value of runup, R_2, as appropriate to dune impact assessment, although alternative exceedance values were not tested. Determining the most appropriate exceedance value will be one focus of this study.

Based on an extensive data set of video observations from ten experiments from a variety of beaches, Stockdon et al. (2006) provided an equation relating R_2 to bulk environmental conditions assuming a slightly non-Gaussian relation between runup and swash

$$R_2 = 1.1\left(0.35\beta(H_0L_0)^{1/2} + \frac{[H_0L_0(0.563\beta^2 + 0.0004)]^{1/2}}{2}\right) \qquad (2.1)$$

H_0 is the offshore significant wave height, L_0 is the offshore wavelength and β is the foreshore beach slope. The first term in equation (2.1) represents the contribution of mean water level, $\langle\eta\rangle$, to runup, and the second term represents the contribution due to

two standard deviations of swash, $2\sigma_s$. In the original paper, Stockdon et al. (2006) used the mean slope in the region of active swash (defined as the region between $\langle\eta\rangle\pm 2\sigma_s$) as the value for the foreshore beach slope, $\beta_{2\sigma}$. However, storm waves are likely to rapidly flatten the foreshore profile rendering climatological measurements of $\beta_{2\sigma}$ irrelevant for predicting subsequent dune erosion. To compensate for the change in location of the swash zone during storms, Stockdon et al. (2007) approximate a storm value of $\beta_{2\sigma}$, β_s, as the mean slope between the still water line and the base of the dune. The definition of β_s is further complicated under dune erosion conditions, when swash is acting over both a foreshore and scarp slope, which may vary rapidly as the dune slumps. Feedback between storm runup, the foreshore slope and the resulting dune erosion will be a focus of this study.

While the Storm Impact Scaling provides a useful classification of the potential for dune erosion, it does not quantify the magnitude of erosion, or account for time–varying wave forcing. Edelman (1968; 1972) developed a model for dune erosion where the beach profile shifts landward as a function of maximum storm surge. Vellinga (1986) extended this approach with an empirical equation for erosion as a function of surge, wave height and sediment fall velocity based on a series of large and small scale wave flume tests. Although the magnitude of erosion is estimated, there is no explicit recognition of storm duration.

A second class of models, time-dependent cross-shore sediment transport models, is capable of quantifying the details of dune erosion under time-varying

forcing. Within this second class of models, EDune (Kriebel and Dean, 1985) and SBeach (Larson and Kraus, 1989) are based on equilibrium profile assumptions. These models have the advantage of not being computationally demanding, while including the effects of time dependence and water level. A second group of time-dependent models are process-based, including Durosta/Unibest DE (Steetzel, 1993), CROSMOR (van Rijn, 2009), and XBeach (Roelvink et al., 2009a). Each includes different assumptions about hydrodynamics and sediment transport, but all quantify the time-dependent dune erosion by interpolating the offshore transport from the shallowest grid location where hydrodynamics may be modeled or assuming an avalanching mechanism to approximate the actual dune erosion. In general, these models are more computationally intensive than the Storm Impact Scaling, the Vellinga equation, or Edune and SBeach, but provide quantitative estimates of time dependent dune erosion and are capable of modeling the feedback between forcing and response on the beach. However, none attempt to model the physics of fluid interaction with the dune.

A third approach that does model swash-dune interactions is the wave impact model (Fisher et al., 1986; Overton and Fisher, 1988; Overton et al., 1994a). This model hypothesizes that the volume erosion rate of the dune is linearly proportional to the momentum flux impacting the dune face, or

$$\Delta V = \sum C_c F \qquad (2.2)$$

where ΔV is the volume of eroded sediment, C_c is a calibration coefficient, and F is the force of impact per wave. The wave impact model was extended by Larson et al. (2004; hereafter LEH04) to include an explicit dependence on both the runup elevation, R, and the duration of exposure, t

$$\Delta V = 4C_s(R - z_b)^2 \frac{t}{T} \qquad (2.3)$$

where C_s is an empirical coefficient, T is the wave period and z_b is the elevation of the dune base. In LEH04, the appropriate value of runup, R_L, is assumed to be

$$R_L = 1.58\sqrt{H_{0rms}L_0} \qquad (2.4)$$

where H_{0rms} is deep water root mean square wave height. Unlike equation (2.1), LEH04 neglected β and calibrated R_L for experiments where the mean value of β was 0.16. However, equation (2.1) assuming a constant β of 0.16 produces results nearly identical to (2.4) so the LEH04 effectively provides R_2 statistics. The coefficient, C_s, which parameterizes the physics of the interaction between hydrodynamics and sediment, depends on the ratio between H_{0rms}, and the median grain diameter.

The LEH04 formulation is attractive because it is derived from a physics-based impact model but is expressed in simple, intuitive terms. It seems sensible that dune erosion should be related to the magnitude of exposure of the dune face, $(R-z_b)$, and also to the duration of that exposure, t/T, which can be thought of as the number of collisions between the runup and the dune. Ruggerio et al. (2001) and Pye and Blott (2008) also found that the best predictor of magnitude of dune erosion on the Oregon and United Kingdom coasts was length of exposure to waves. In this paper we will

test the LEH04 equation both in terms of the individual dependencies and the overall performance of the equation.

Dune erosion research has been slowed by the limited availability of data. Typically, only pre- and post-storm observations of dune erosion are available from the field, because harsh conditions preclude making observations during storms. As a result, most of the observations used to develop and validate dune erosion models have come from near-prototype wave flume experiments. Large-scale experiments have the advantage of controlling both offshore wave conditions and sediment characteristics, and reducing the dune erosion problem to two dimensions. Dette (2002) provides an extensive review of large scale experiments. More recently, van Ghent et al. (2008) and van Thiel de Vries (2008) describe a 2006 large scale dune erosion experiment in the Delta Flume, De Voorst, the Netherlands.

While previous large-scale flume experiments form the basis of our knowledge of dune erosion, the survey methods have limitations. Traditional surveys require stopping the experiment to collect profiles, a time consuming process that potentially affects pore water processes in the dune. Individual slumping events, the basic unit of dune erosion, are not captured or their physics understood. Traditional surveying techniques are transect-based and may poorly represent alongshore-variable slumps or the volumetric rates of dune erosion. These methods also usually sample vertically so cannot capture undercutting and may include a response lag at the steep edges of a

dune front because a measuring rod falls at a finite rate, so may only poorly represent the details of the eroding dune edge.

Optical remote sensing methods provide a robust alternative tool for monitoring the harsh nearshore environment (Holman and Stanley, 2007) when traditional surveying is not feasible. Video techniques are low-cost and non-intrusive and allow continuous sampling without interruption of an experiment. Stereo video allows us to measure the beach surface with vertical spatial resolution comparable to traditional survey techniques, but at much higher horizontal and temporal resolution. In this paper, we develop and test an optical remote sensing method to observe dune morphology on slump event timescales and estimate the net cross-shore transport across the dune and foreshore on timescales faster than traditional surveys allow and without interruption of wave forcing.

Previous large scale experiments have tested constant wave conditions until an equilibrium profile develops. However, this approach precludes understanding the sequencing of forcing. In this paper, we quantify time dependent dune erosion and wave runup by modeling a storm hydrograph during a dune erosion experiment. Later, we will show that the length of exposure to waves is nearly as important as knowing the details of water level for modeling dune erosion.

In the section 2.3, we introduce the theory of stereo sampling and adapt the principles of Holland and Holman (1997) to develop a binocular method for observing foreshore morphology based on time varying runup signals. Section 2.4 of this paper

describes a near-prototype dune erosion experiment conducted at the O.H. Hinsdale

Wave Research Lab. Section 2.5 describes the accuracy of the stereo remote sensing

technique and quantifies changes of beach morphology. The final sections discuss

implications of results for dune erosion models and describe conclusions.

2.3 Stereo Methods

2.3.1 Stereo Technique

Stereo analysis relies on the matching of features seen from two different

camera views, analogous to each eye viewing a scene slightly differently to give depth

perception. The stereo method is composed of two main components, an automated

feature matching algorithm, and a triangulation algorithm. First, we will describe the

triangulation method, which is well-known, and second, we will describe two feature

matching algorithms, one for the subaerial beach, where many features are available

for matching, and one algorithm for the swash zone, which is relatively featureless and

is complicated by optical reflections.

2.3.1.1 HOMOGENEOUS COORDINATE FORMULATION AND TRIANGULATION

The analysis and manipulation of computer images is best formulated using the

concept of homogeneous coordinates, a mathematical formalism developed specially

for computer vision (see, for example, Hartley and Zisserman (2004), the source for

the following discussion). In the homogeneous coordinates formulation, a vector of

real world positions is augmented by adding an additional coordinate of 1, $X = (x, y, z,$

$1)^T$. The homogeneous representation of the real world position is transformed to the image plane, $x = (u, v, 1)^T$, via a camera projection matrix, P, as

$$x = PX \qquad (2.5)$$

where the equality is true to within a multiplicative constant. P is a 3 x 4 matrix containing camera position, pointing angles and calibration information that may be decomposed into

$$P = K\Omega\left[I \mid -C\right] \qquad (2.6)$$

where K is the camera calibration matrix, Ω is the rotation matrix representing the camera look angles, I is the identity matrix, that is augmented by C, the camera position in real-world coordinates.

If a feature is identified in each of two images, the world location, X, of the feature may be determined via linear triangulation. Combining and rearranging equation (2.5) for each camera, $x_1 = P_1X$ and $x_2 = P_2X$ yields the equation $AX = 0$ where,

$$A = \begin{bmatrix} u_1 p_1^{3T} - p_1^{1T} \\ v_1 p_1^{3T} - p_1^{2T} \\ u_1 p_2^{3T} - p_2^{1T} \\ (v_1 + D)p_2^{3T} - p_2^{2T} \end{bmatrix} \qquad (2.7)$$

p_n^{iT} are the rows of P transposed to column vectors, and D is the pixel distance between feature matches in camera 1, C_1, and camera 2, C_2, known as disparity.

Finally, $AX = 0$ may be solved via a least squares solution for X, where X is the eigenvector associated with the smallest eigenvalue from the singular value decomposition of A.

2.3.1.2 THEORETICAL STEREO RESOLUTION AND ERROR

Error in determining the pixel location of a matching feature in a camera (ΔD) will result in an error in the elevation of the stereo measurement (Δz),

$$\Delta z = \frac{dz}{dD} \Delta D \qquad (2.8)$$

where dz/dD is the stereo resolution of the camera defined as C_1 in equation (2.7). This equation has two applications. First, the vertical resolution of a single pixel for a particular stereo camera configuration can be determined by assuming a one-pixel shift in ΔD. Second, if errors in D are quantified, equation (2.8) gives the corresponding vertical stereo error. dz/dD is estimated numerically by differencing stereo estimates for adjacent disparities.

2.3.1.3 IMAGE ALIGNMENT

Traditionally, stereo photography was carried out using a specialized stereo rig on which two identical cameras, separated by a baseline distance, b, are mounted with image planes carefully aligned. Because of the special image geometry of the idealized rig, the search for feature matches between the image pair is limited to the corresponding columns in each image, a considerable simplification. In practice, it is unlikely that the image planes for both cameras will be parallel to the baseline or that

focal lengths of two cameras will be identical, even for lenses of the same make. For more typical viewing geometries, the search for matching features is still one-dimensional, along image transects called epipolar lines (Hartley and Zisserman, 2004), but the search is cumbersome. However, imperfectly oriented images can be transformed into idealized image pairs, similar to the traditional stereo rig, using concepts of homogeneous coordinate transformations (Hartley and Zisserman, 2004).

The method is based on transforming the original images using new projection matrices that correspond to the idealized stereo rig. This requires defining a set of viewing angles (hence rotation matrix, Ω) that are orthogonal to the baseline, b, with image columns aligned with b. Thus, the first axis of the new frame, x_s is set equal to b. Next, the principal axis, z_s, directed toward the camera front, is defined as

$$z_s = \begin{bmatrix} 0 & 1 & 0 \end{bmatrix} \times b.$$ (2.9)

The third vector making up the new coordinate frame is then defined as

$$y_s = x_s \times z_s$$ (2.10)

Finally, a new rotation matrix, Ω_s, is defined as

$$\Omega_s = \begin{bmatrix} y_s \\ x_s \\ z_s \end{bmatrix}^T$$ (2.11)

The idealized intrinsic camera calibration matrix, K, that describes the focal length and image center, can in principle be chosen as K matrices corresponding to one of the two

cameras. However, it is sensible to choose the focal length for the stereo pair that will make the pixel footprint in the rectified view approximately equal to the pixel footprint in the original view. The identical K and Ω_s matrices are then combined with the individual camera positions to produce projective matrices P_{s1} and P_{s2} for equivalent idealized stereo cameras.

Finally, a projective transform (homography, H) that maps each image from the original camera view (P) to the idealized view defined by P_s is found by

$$H = P_s P^+ \tag{2.12}$$

where P^+ is the pseudo-inverse of P. Then points in the original view are mapped to the stereo view as

$$x_s = Hx \tag{2.13}$$

After transformation of each image, the search for matching stereo features is again limited to corresponding columns.

2.3.2 Feature Matching Techniques

Accurate feature matching is the key component to producing precise stereo results (equation (2.8)). Because there are abundant contrast features on the dune, traditional methods can be used. However the foreshore environment is typically smooth and generally lacks image contrast features, so requires an alternate methodology. In this section, we describe the algorithms, including improvements, used for each domain.

2.3.2.1 DUNE AREA-BASED STEREO METHOD

Stereo analysis of the dune face and top was based on a cross-correlation and dynamic programming algorithm originally developed by (Sun, 2002b). The algorithm is composed of several steps but is primarily based on finding the disparity, D (pixel distance between feature matches), that maximizes optical similarity, E (called evidence), for each pixel over the entire domain. Because evidence is based on a two dimensional convolution of fixed size, the images are first high-pass filtered to remove variance at larger scales. The map of evidence over the domain is then found for a range of plausible disparities. Finally an optimum path is found through the evidence space so that unique values of disparity, hence world location, from equation (2.7), can be found for every imaged location.

A number of measures of feature similarity (evidence) have been proposed in the literature. We have based our analysis on the simple measure of lagged cross-correlation,

$$
\rho = \frac{1}{\sqrt{\sigma_1^2 \sigma_2^2}} \sum_{i=u-m}^{u+m} \sum_{j=v-n}^{v+n} \left(I_1(i,j) - \overline{I_1}(u,v)\right)\left(I_2(i,j+D) - \overline{I_2}(u,v+D)\right)
$$

$$
\sigma_1^2 = \sum_{i=u-m}^{u+m} \sum_{j=v-n}^{v+n} \left(I_1(i,j) - \overline{I_1}(u,v)\right)^2 \tag{2.14}
$$

$$
\sigma_2^2 = \sum_{i=u-m}^{u+m} \sum_{j=v-n}^{v+n} \left(I_2(i,j+D) - \overline{I_2}(u,v+D)\right)^2
$$

I_1 and I_2 are the high pass filtered grayscale images from cameras C_1 and C_2. Over bars denote the mean image intensity within the m x n correlation window. The

optimum size of the correlation window is a trade-off between resolution and

statistical stability and depends on image texture. Optimum window size was

determined by conducting a sensitivity test to minimize scatter in range direction on

the beach surface. Correlation window sizes between 3 by 7 (rows by columns) and

41 by 41 were tested. The window size was set to 35 by 25 pixels since this was the

highest resolution window that minimized scatter. Finally, since search algorithms

typically find cost function minima, evidence (E) is defined as normalized negative

correlation,

$$E = \frac{-\left(\rho + \min\left(-\rho\right)\right)}{\max\left(-\rho\right)} \tag{2.15}$$

Figure 2.1 (c) shows the evidence map, for a single epipolar line (cross-shore

transect), shown in black (a,b). Regions of dark blue correspond to regions of strong

optical correlation, so are likely feature matches. However, there are often many

possible matches at any location (v pixel coordinate), most of which will not yield a

continuous or sensible dune surface. To produce a single, continuous transect along

this image column, we implement a two stage dynamic programming algorithm

following the method of Sun (2002a). In the first stage, a cost function, $Y_v(u,v,D)$ is

computed (Figure 2.1d), that minimizes the summed values of $E(u,v,D)$ along image

columns (epipoles) from offshore to onshore and is defined as

$$Y_v(u, v, D) = E(u, v, D) + \min(Y_v(u, v-1, D + \Delta D_v)) \tag{2.16}$$

where $\Delta D_v = [\text{-}1\ 0\ 1]$, the shift in D required to follow the minimum cost path along columns. In the second stage of the algorithm, the cost function $Y_v(u,v,D)$ is summed across epipoles (alongshore),

$$Y_{uv}(u,v,D) = Y_v(u,v,D) + \min(Y_v(u-1,v,D+\Delta D_{uv})) \qquad (2.17)$$

ΔD_{uv}, the shift in disparity required to follow the minimum cost path along rows, is recorded. Finally, the global maximum path (Figure 2.1c, black line) through $Y_{uv}(u,v,D)$ is determined by beginning at $u = \min(u)$, identifying the D where $Y_{uv}(u,v,D)$ minimum, and summing ΔD_{uv} along image rows (constant v) according to

$$D(u+1,v) = D(u,v) + \Delta D_{uv}(u+1,v). \qquad (2.18)$$

The global minimum path through $E(u,v,D)$ defines the disparities of matches between pixels in C_1 and C_2. Finally, the stereo solution is determined using the method described in the previous section.

2.3.2.2 RUNUP-BASED STEREO ANALYSIS

In contrast to the dune, the foreshore environment is typically smooth and generally lacks features that may be matched between camera views to make stereo measurements. Analysis is further complicated by the frequent presence of a thin layer of water that generates specular reflectance, acting like a mirror. Stereo analysis of features seen in a planar mirror will yield the position of the virtual object location behind the mirror (beneath the beach) and will be significantly in error. In contrast, the strong scattering of light by the foam edge of wave runup is Lambertian, therefore

seen identically in each camera, so is appropriate for stereo analysis. Since the runup edge lies along the foreshore by definition, time-varying runup position can be exploited to map the foreshore following the method of Holland and Holman (1997). Given the sensitivity of the stereo method equation (2.8), the accuracy criteria for runup measurement for stereo use are more stringent than those for simple runup time series analysis, so a two-step analysis is used. First the approximate runup location is found using traditional runup methods, then the locations are fine-tuned using a one dimensional matching algorithm equivalent to that used above.

Runup data were extracted from cross-shore time stacks (Holman and Stanley, 2007), created from cross-shore pixel arrays located at the centerline of the wave tank. In this experiment, the centerline transect was nearly but not identically co-linear with an epipolar line. However, deviations of up to +/- 2 pixels in the alongshore or approximately +/-2 cm in the foreshore region were considered insignificant since the runup edge is not expected to vary significantly over 2 cm in the alongshore direction.

The foam edge of a wave approaching the shoreline is visible as a bright streak through the time stack (Figure 2.2). A semi-automated runup algorithm defines pixel location of the runup edge (v_r) as the landward-most location where the difference intensity, δI , between the image intensity, $I(v,t)$, and a background running average intensity, $I_{back}(v,t,)$ exceeds a user-specified threshold. This location is reliable for time series analysis of runup, but is often several pixels landward of the base of the steep image intensity gradient marking the runup front. A better estimate of position

of the advancing runup front, v_{rf}, is given by the location of maximum curvature in the intensity profile, $\partial^2 I / \partial v^2$ in a search region defined by the inflection points in $\partial I / \partial v$ onshore and offshore of the digitized runup edge. Of the two signals, the one with the greater curvature is taken as the reference runup, v_{rf}.

To find the matching location, a lagged correlation is used to shift the runup position in the camera with lower signal strength (curvature) to match v_{rf}. Following the work of Sun (2002b), the correlation coefficient is recast as E. Minimum E defines the corrected pixel location of run-up in the camera with the weaker signal. Once the pixel coordinates giving the best match between runup features in both cameras are obtained (v_{rf1}, $v_{rf1}+D$), the 3D position of the feature is determined using equation (2.7).

2.3.3 Subpixel Resolution

The resolution of a surface derived from the above stereo techniques is limited by the discrete pixel resolution. However, fitting methods can be used to achieve subpixel resolution, thereby improving accuracy. Again following Sun (2002b), subpixel resolution for each feature match was determined by fitting a quadratic equation of the form

$$E = \alpha_1 (D - \alpha_2)^2 + \alpha_0 \qquad (2.19)$$

in a +/-2 pixel neighborhood centered at $D(u,v)$. Nonlinear least squares curve fitting is used to solve for the coefficients, and α_2 defines the subpixel value for D.

2.3.4 Error Thresholds

Error in stereo estimation may be grouped into three categories: 1) error due to camera hardware, including lens distortion and sensor noise; 2) error due to the stereo algorithm, including resampling, correlation window size, matching algorithm, 3) error due to the scene, including image geometry, lighting, and low image texture (Egnal et al., 2004). The first category is dependent on intrinsic camera properties, and not directly on the stereo algorithm or image contrast. In this section, we define three objective thresholds obtained from the feature matching process to quantify and minimize errors described in the last two categories. First, we removed all feature matches where correlation between features was negative ($\rho < 0$). Second, we removed all feature matches where the high-passed image variance was too low to produce good feature matches ($\sigma^2 < 0.01$). Finally, we removed all matches where curvature of the $E(v,D)$ surface was low ($\alpha_l < 0.01$), indicating a poorly defined feature match caused by low image texture, low resolution, or poor lighting. Later, in the results section, we define a relationship between α_l and scatter to define error in terms of D that is related to error in real world coordinates via equations (2.7) and (2.8).

2.3.5 Interpolation

Results from the stereo method were spatially smoothed in space and time to reduce noise. Since errors in stereo estimates occurred in range direction (r) from C_1, data were interpolated in (u,v,r) space, then transformed to (x,y,z) via the look

direction from the center of C_1 to each pixel. An advantage of interpolating in range direction is resolution of the steep or potentially overhanging dune scarp, which would be obscured if the data were interpolated in the across-shore direction. Interpolation was carried out in both space and time using a linear smoother with a Hanning filter (Plant et al., 2002) in space and boxcar averaging in time. For the dune region, the length scales of spatial smoothing window were set to the same length as the correlation window (35 pixels, 25 pixels) in (u,v) to achieve a final horizontal cross-shore resolution of approximately 0.1 m. Estimates were also time-averaged over 5 images, collected over 120 s (sub-samples taken every 30 s) to reduce noise. For the foreshore, the length scale of smoothing was 25 pixels in v. Stereo estimates collected over 15 minute intervals were averaged to fully map the beach profile and reduce noise.

2.3.6 *Run-up Elevation Measurements*

The vertical elevation of run-up was determined by projecting the beach profiles generated by the stereo method back into image coordinates. From the vertical elevation data associated with each pixel location, runup time series pixel data were converted to vertical elevation by linear interpolation.

2.4 Experiment Description

2.4.1 O.H. Hinsdale Large Wave Flume

The dune experiment was conducted at the Oregon State University O.H. Hinsdale Wave Research Lab in the Large Wave Flume. The flume is 107 m in length, 3.7 m in width, and 4.6 m in depth at the wave maker. The hinged wave maker was capable of producing monochromatic and random waves with a maximum wave height of 1.6 m at a period of 3.5 s. The origin of the wave flume coordinate system is located at the center of the base of the wave maker. A beach was created at the far end of the wave flume using 611 m^3 of Oregon beach sand with median grain size of 0.23 mm. The initial beach profile (Figure 2.3) consisted of a flat bottom for 35 m shoreward of the wave maker, a relatively planar sand beach intersecting with the still water level near $x = 80$ m, a steep foreshore ($\beta_s = 0.17$) and dune.

2.4.2 Wave Conditions

The experimental wave conditions were designed to be representative of a Northeaster' storm conditions that occurred offshore of Assateague Island, MD/VA, USA on February 3-8 1998. This storm was chosen as the prototype for our experiment because offshore wave conditions were recorded and pre- and post-storm beach topography was collected with lidar. Prototype wave conditions at NOAA Buoy 44004, located at (38.48 N, 70.43 W), 370 km east of Cape May, NJ, indicated a maximum significant wave height of 7.35 m; maximum peak period of 12.5 s; and maximum storm surge of 1.03 m. Conditions modeled in the laboratory were

determined by Froude scaling (Dean and Dalrymple, 2002) with a model length scale 1/6 of prototype and resulting time factor of $1/\sqrt{6}$. In Figure 2.4, the thick lines represent wave conditions modeled in the lab. Maximum significant wave height modeled in the flume was 1.3 m; maximum peak wave period was 4.90 s; and maximum storm surge was 0.17 m. The duration of maximum storm conditions during the experiment was 6 hours. The wave maker was programmed with a TMA spectrum of appropriate significant wave height and peak period and random phase. The experiment was carried out in 15 minute increments; then the standing wave energy was allowed to settle before the test continued. Results from hours 8 - 20 of the experiment, when dune erosion occurred, will be discussed in this paper. Prior to hour 8 of the experiment, low wave conditions, representing pre-storm conditions, resulted in minimal sediment transport and no dune erosion. Dune erosion occurred when waves exceeded the dune base, and the primary mechanism of erosion was slumping of sediment from the dune that was then carried offshore via swash zone processes.

2.4.3 Profile Surveys

In situ beach profiles were collected using two methods depending upon the region of the beach being measured. The subaqueous profile was determined using an acoustic sensor, while the subaerial profile was collected using a laser range finder. The profiling equipment was mounted on a motorized cart at $y = -0.86$ m in the alongshore. The cart was driven along the length of the flume to collect a profile.

Profiles were collected every hour throughout the experiment. Vertical and horizontal resolution of the profiling system was estimated to be 0.02 m. The scatter of observations made with the laser range finder for ground truth of the stereo method was also estimated. A cement step at the back of the wave flume was surveyed 31 times over the course of the experiment. Standard deviation of elevation observations was 0.007 m.

2.4.4 Cameras

A stereo pair of Point Gray Scorpion charge-coupled device cameras was mounted on the roof of the wave flume looking downwards into the flume from an elevation of 15 m (Figure 2.3) above the flume floor (about 9 m above the still water line). Image resolution was 960 x 1280 pixels. The cameras were calibrated and surveyed to determine image geometry. Cross-shore resolution of the cameras was approximately 3 cm and alongshore resolution was approximately 1 cm near the foreshore and dune. Theoretical stereo resolution, determined using equation (2.8), was approximately 0.10 m and 0.04 m in the horizontal and vertical, respectively for the foreshore and dune region of interest (Figure 2.5). Cross-shore transects of pixel intensity were collected from both cameras at 10 Hz at $y = 0$ m, down the center of the wave flume for runup measurement (Figure 2.2) Synchronous full images were collected by each camera at 2.5 Hz for stereo analysis.

2.5 Stereo Results

2.5.1 Spatial Coverage, Scatter, and Bias

The most significant advantage of the stereo method is the high spatial

resolution on the beach surface (Figure 2.6), combined with estimates of error from

the stereo method (Figure 2.7), all at higher temporal resolution than traditional

surveys allow. Point density of raw stereo estimates was 1589 points/m^2 over the dune

top, 2698 points/m^2 over the dune scarp, and 3756 points/m^2 over the foreshore.

Scatter of raw stereo estimates was normally distributed (significant at the 95% level)

in range direction about the mean dune surface.

To estimate confidence intervals on stereo estimates, 200 realizations of

unchanging top of the dune (away from the dune crest) were collected and the

standard deviation in disparity, σ_D, was found at each pixel location from the

ensemble. These values were regressed against a number of quality variables. In the

end, the linear relationship

$$2\sigma_D = -26.66\alpha_1 + 2.55 \qquad (2.20)$$

was found to explain 90% of the data and provides a useful method of estimating

confidence intervals exclusively from image data.

To further test the efficacy of the confidence interval calculated according to

equation (2.20) at parameterizing scatter in the data, the error bars for this ensemble of

unchanging locations were normalized as

$$\sigma_n = \frac{2|r - \mu_r|}{\sigma_r} \tag{2.21}$$

where σ_r is the confidence interval described in equation (2.20) projected to range from C_1, r is the range for each individual estimate, and μ_r is the mean location of the dune surface in range direction. Assuming scatter is normally distributed, and confidence intervals are uniformly distributed, the standard deviation of the normalized error bars should be 1 for error bars that perfectly parameterize scatter. 98 % of σ_n ranged between 0 and 2 over the region of interest and 62 % of σ_n ranged between 0 and 1 (Figure 2.8) indicating that σ_r is representative of scatter about the mean.

2.5.2 Stereo-Survey Comparison

To test the quality of stereo results, bias and root mean square error (RMSE) in elevation were calculated for the stereo observations coincident with the 16 surveyed dune profiles during the experiment (Figure 2.9), along with errors over the foreshore, scarp, and dune top. Over the full profile, average bias was -0.01 m, but ranged between -0.03 m and 0.02 m throughout the experiment, and the average RMSE was 0.05 m, but ranged between 0.03 m and 0.08 m. These errors are equivalent to errors of 1 to 2 pixels, based on stereo resolution (Figure 2.5), so the magnitude of error is reasonably small. Of the three subsections of the dune, bias and RMSE were largest over the dune scarp where the stereo method typically produced an overhanging dune, while an overhange was not observed qualitatively or in surveys. The mean horizontal

error caused by the overhang was 0.09 m and RMSE was 0.13 m, equivalent to errors of approximately 1 pixel. The overhang was created by the smoothing effect of the correlation window in disparity space as the correlation window passed over the dominant optical feature associated with the dune scarp. When the smoothed surface was translated from disparity space to real world coordinates via equation (2.7), the overhang was produced (Figure 2.7). The resulting dune scarps have dune crests shifted offshore of the true position. The overhang effect is most pronounced on images with low contrast on the dune front and when the dune is farthest from the camera, resulting in low pixel resolution. Error bars slightly undersestimate the magnitude of the overhang effect (Figure 2.7).

2.6 Experimental Results

Our analysis will be framed around equation (2.3), which related eroded volume of the dune to the fluid forcing in terms of the magnitude and duration of runup exceedance above the dune base. First, we examine each forcing element in terms of observations and expectations from parameterizations. Next, we compare each element with observed dune erosion. Finally, we couple the observed and parameterized forcing elements using the equation (2.3) and compare results with observed dune erosion.

2.6.1 Beach Profiles and Dune Erosion

Beach profiles were extracted from stereo data down the tank center every 15 minutes while the dune was slumping. Figure 2.10 shows the retreat of the dune over

the course of the experiment. The dune crest (x_c, z_c) and dune base (x_b, z_b) were manually digitized for each profile as the points of maximum curvature.

The main parameter of interest for quantifying dune erosion is the volume eroded per unit beach width per unit time. This was estimated as

$$\Delta V = \sum_{z_b}^{z_c} \Delta x(z) \ \Delta z \qquad (2.22)$$

where ΔV was estimated over consecutive 15 minute time segments (Figure 2.11).

Maximum dune erosion occurred at hour 10, when wave height, period, and water level were increased (Figure 2.4). Erosion from the dune decreased as waves maintained a constant height between hours $10 - 12$, and flux increased again after hour 12, when wave height, period and water level were increased to the maximum for the experiment. The maximum flux after hour 12 was less than that immediately after hour 10, despite the larger waves and higher surge level. The large magnitude flux at hour 17.25 is likely due to error in position of the dune during a time when image contrast was low. Video observations indicate that slumping did not occur during this period.

2.6.2 Wave Runup

The first parameterization for estimating dune erosion volume is $(R - z_b)$. While Sallenger (2000) recommended the 2% exceedance as the relevant runup statistic for dune erosion, the appropriateness of this statistic has never been tested.

We have investigated the performance of 2%, 7%, 16%, 23%, and 30% exceedance values. Observed exceedance values were calculated from the cumulative probability distribution of R, the elevation of individual maxima above the still water line identified from the time series of runup elevations (Stockdon et al., 2006). Assuming a Gaussian distribution of swash statistics (Stockdon et al., 2006), the exceedance values tested correspond to the combined mean water level plus $n_\sigma = 2$, 1.5, 1.0, 0.75, and 0.5 times the standard deviations of the swash time series (σ_s).

Observed exceedance elevations were compared with equation (2.1), modified to account for the different exceedance elevations by including n_σ, the coefficient to adjust the number of σ_s considered

$$R_n = 1.1\left(0.35\beta(H_oL_o)^{1/2} + \frac{\left[H_oL_o\left(0.563\beta^2 + 0.0004\right)\right]^{1/2}}{2}\frac{n_\sigma}{2}\right). \qquad (2.23)$$

β in equation (2.23) was parameterized in four ways: 1) with the time-varying mean beach slope between the still water line and the base of the dune, β_s, 2) with the observed beach slope at hour 8, prior to the onset of dune erosion, β_0, 3) and 4) with the time varying mean beach slopes appropriate to in the active swash regions (Figure 2.12), $\langle\eta\rangle \pm n_\sigma\sigma_s$, denoted $\beta_{1\sigma}$ and $\beta_{2\sigma}$ for R_{16} and R_2, respectively. Only results for R_2 and R_{16} will be presented in detail, because later it will be shown that R_{16} was most proficient at predicting volume of sediment eroded from the dune. In addition, beach slopes can be computed by least squares or as end-point mean values. Each method weights the foreshore profile data differently.

First, we present results for observations of R_2 which was lowest between hours 8 and 10 (Table 2.1), corresponding to minimum storm wave conditions and water level. R_2 increased at hour 10 when wave conditions and water level increased then remained relatively constant (standard deviation of R_2 was 0.03 m) through hour 20, although wave conditions and water level increased at hour 12 and decreased at hour 18. Based on observations of the horizontal excursion of runup past the dune crest, it is apparent that overtopping was occurring between hours 10 and 20. The probability density function of R between hours 12 and 14 was truncated once runup reached the dune top (Figure 2.13). This truncation precludes testing runup models for 2% exceedance. Therefore, we will focus on observations and parameterizations of R_{16} for the rest of this section.

Like R_2, R_{16} was lowest between hours 8 and 10 (Figure 2.14). In contrast to R_2, R_{16} was never truncated by reaching the dune crest, so responded to changing wave conditions and water levels at hours 10, 12, and 18. Although incoming wave height and period were constant between hours 12 and 18, observed runup energy dropped significantly after hour 14.5 (Figure 2.14, thick black line). Possible reasons for this anomalous drop are included in the later discussion section. Runup results are presented in two-hour blocks to allow isolation of these unknown effects. All other sections are based on the entire dataset.

Next, we compare observations of R_{16} with predictions from equation (2.23) but using different definitions of beach slope. Results are plotted in Figure 2.14 and

summarized in Tables 2.2 and 2.4 (bias) and Tables 2.3 and 2.5 (RMSE). The experiment included periods for which runup minimally exceeded the dune base (hours 8 - 10 and 18 - 20; the Sallenger, 2000, swash regime) and times of significant runup impact with the vertical dune face (hours 10 - 18; the Sallenger collision regime). Since the equation (2.23) was based on swash regime processes on simple foreshores, it should provide reasonable predictions for the swash regime periods but may be systematically in error during times of collision regime. Examining data from swash regime conditions, it is apparent that $\beta_{1\sigma}$ provides the best predictions (Table 2.2 and 2.3, second column), followed by β_0 (Tables 2.2 and 2.3, fourth column). While Stockdon et al. (2006) study used $\beta_{2\sigma}$ to model their statistic of R_2, it seems appropriate that $\beta_{1\sigma}$ should be more appropriate for the $1\sigma_s$ statistic, R_{16}. In fact, $\beta_{2\sigma}$ under-predicts R_{16} throughout the experiment.

During collision regime conditions, hours 10 - 14, all estimates under-predict the observed runup. Since equation (2.23) is based on foreshore profiles seaward of dunes, this under-estimate is not a surprise but could be empirically adjusted to correct for dune impact by multiplication by dune factor, K_d. Mean values of K_d for hours 10 - 14 are listed in Table 2.6. Again, $\beta_{2\sigma}$ strongly underestimates observed R_{16} and is not considered an attractive option from either a theoretical or observational point of view. β_s provides estimates that are reasonable but noisy, especially when used in the end-point mode. The best choices seem to be $\beta_{1\sigma}$ and β_0 as these provide stable

estimates that can be easily corrected for dune runup by multiplication by K_d. Best

results are from least-squares estimation methods. End point methods are more noisy.

2.6.3 Position of the Dune Base

The elevation of the dune base, z_b, combined with the runup elevation is used

to estimate the fluid forcing of dune erosion (LEH04; equation 2.3). If the dune base

elevation rises as the dune erodes, the erosion rate will be reduced. This could be an

important feedback in the system. Thus, successful prediction of dune erosion

requires knowledge of the expected trajectory of the eroding dune toe.

If we describe the dune toe trajectory as following a slope, β_T, two end member

retreat trajectories exist. The first would be direct landward erosion so that z_b never

changes

$$z_b(t) = z_b(0)$$
$$\beta_T = 0$$

(2.24)

The second end member trajectory is that erosion moves the dune toe directly up the

foreshore slope

$$z_b(t) = \beta_T(t)x(t) + z_b(0)$$
$$\beta_T = \beta_f(0)$$

(2.25)

More generally, we can express the observed trajectory as a fraction of the foreshore

beach slope. Previous laboratory observations suggest that a retreat along the

foreshore beach slope ($\beta_T/\beta_f(0) = 1$) is reasonable (LEH04).

The measured trajectory of z_b is shown in Figure 2.15. On average the dune toe trajectory follows a slope of 0.09 ($R^2 = 0.87$, significant at the 95% confidence interval), but with some variations associated with slump events. Compared to the initial foreshore slope, $\beta_f(0)$, of 0.17 the ratio $\beta_T/\beta_f(0)$ averaged over the experiment was 0.54, clearly inconsistent with the LEH04 results. The effect of assuming this trajectory on the estimate of eroded volume will be tested in later in the results section.

2.6.4 Period of Exposure to Runup

The final parameterization in estimating dune erosion using LEH04 is the non-dimensional period that dunes were exposed to runup. Period of exposure was parameterized in equation (2.3) as t/T which is a proxy for the number of collisions with the dune. We also tested an alternative parameterization, where the number of collisions was quantified by incorporating information about the probability distribution of wave runup, $p(z_R)$, and z_b. In this parameterization, the number of collisions, N_c is defined as

$$N_c = \left[P\!\left(z_R + z_{SWL} > z_b \right) \right] \cdot \frac{t}{T_p} \tag{2.26}$$

where $P(z_R)$ is assumed to be the cumulative Gaussian distribution defined by $\langle \eta \rangle$ and σ_s derived from equation (2.1). z_R is the runup elevation, and z_{SWL} is the elevation of the still water level. z_b was estimated assuming a retreat of the dune base along β_T and a known cross-shore dune position.

Observations of the number of collisions are shown in Figure 2.16 (heavy line) and were determined by counting the times the digitized runup edge exceeded the dune base. N_c was highest between hour 8 - 8.25 when wave period was shortest of any time during the storm (3.1 s) and the z_b was lowest. N_c decreased rapidly as z_b increased during the first 2 hours of storms waves. The number of collisions increased at hours 10 and 12, when wave conditions and water levels increased, then decreased as z_b increased between hours 12 and 20. Finally, N_c dropped to only 2 - 3 collisions after hour 20, when waves and water level were decreased.

The parameterization for number of collisions as t/T significantly over-estimated the observed value (bias = 155 collisions, RMSE = 160 collisions, R^2 = 0.53). The over estimation was largest at the end of the experiment, when few waves reached the dune. Results improved using equation (2.26) and assuming retreat of the dune along β_T and R_2 parameterized by equation (2.1) with the $\beta_s(t)$ (bias = -27 collisions, RMSE = 34 collisions, R^2 = 0.75). Estimates were good for hours 8 to 12. Later in the experiment, z_b was overestimated by equation (2.25) and N_c was consequently underestimated.

2.6.5 Comparison with Observed Erosion

The observations of (R_n - z_b) and N_c were compared with observed dune response to determine contribution of each variable to eroded volume (Figure 2.17). The assumption that (R_n - z_b) was linearly related to dune erosion volume was tested first. The correlation-squared for all runup exceedance levels, n, was between 0.30

and 0.60, all significant at the 95% level (Figure 2.18). However, the correlation-squared for R_{16} was highest. Next, the observations of N_c were compared to dune response. The correlation-squared was 0.37, significant at the 95% level. These observations suggest that the components of equation (2.3) have predictive skill.

Equation (2.3) was compared with observations of dune erosion in two ways: using observed forcing and known beach profiles to demonstrate the model reliability given known conditions, and using the initial beach profile and parameterized forcing based on offshore conditions, to demonstrate how the model would perform in a forecast or hindcast scenario where runup and beach profile throughout the storm were not measured.

Given known forcing from R_{16}, beach profiles, and $C_s = 1.34 \times 10^{-3}$ (following LEH04) equation (2.3) reproduced 64% of the observed variance in dune erosion volume (Figure 2.19, upper plot). Bias in eroded volume for LEH04 was 0.03 m^3/m/15 min and was 0.05 m^3/m/ 15 min. Initially, eroded volume was over-predicted but eroded volume rapidly tapered as the dune base eroded upward and was less exposed to runup. Between hours 10 and 12 the model overestimated eroded volume, but the trend towards decreasing erosion with time matched observations. Between hours 12 and 20, the model tracked observed eroded volume well. The observed eroded volume was noisier than the model; some of the observed noise is due to errors in the stereo technique.

Given parameterized forcing from offshore wave conditions, initial beach slope and equation (2.23) with $n = 16$, equation (2.25) with $\beta_T = 0.54$, and equation (2.26), the eroded volume was calculated, then the profile was updated assuming retreat along β_T, and eroded volume calculated for the next 0.25 hr interval. The modeled explained 49% of observed variance in eroded volume (Figure 2.19, lower plot). Bias was 0.00 m^3/m/15 min, and RMSE was 0.05 m^3/m/15 min. In terms of dune morphology, the model underestimated retreat of the dune base by only 0.36 m out of 5.04 m of erosion over the full 12 hours of active erosion.

2.7 Discussion

2.7.1 Stereo Video Analysis

Stereo video appears to provide a good tool for the non-intrusive measurement of an eroding foreshore and dune system. Resolution is excellent and accuracies are good in most circumstances. In most cases, regions of weak performance are flagged by an objective confidence estimate that is based totally on video observations, so can be appropriately smoothed over. However, two areas of improvement could be made. First, lighting for the experiment was sub-optimal in two ways. At times, strong morning sunlight saturated image intensities, particularly on the dune crest. With limited contrast, estimates were noisy (although confidence intervals were correspondingly large). Similarly, under some lighting conditions, there was little optical contrast on the eroding dune front. This was a particular problem in the

vicinity of the strong contrast signal at the dune crest, and correlation windows were often dominated by the dune crest optical signal over a broad range of lags.

Similarly, performance of the stereo algorithm depends on the resolution of the images. As shown in Figure 2.7, the application of a correlation window over the discrete feature of the dune crest resulted in an overhang. Error due to this issue was initially very small, but increased as the dune eroded towards the lower resolution section of the image. Low image variance at the scarp combined with lower resolution precluded using a smaller correlation window to improve the overhang in this experiment. Issues of resolution should be considered when designing a stereo installation.

While the described stereo methods could provide an elegant solution to field sampling of an eroding dune during a storm, it must be recognized that field installations will have some challenges. The principle issue would be the placement of cameras to provide views of a seaward facing dune front. This will only be possible if seaward mount points are available, for example a pier or piling. Similarly, lighting cannot be controlled for outdoor applications but will vary with sun angle and alter image contrast throughout the day.

2.7.2 Run-up and Dune Erosion

This experiment is one of the first where wave run-up was quantitatively observed during both collision and overtopping conditions. The Sallenger (2000) model defines these erosion regimes in terms of the 2% exceedance level of runup, R_2,

while LEH04 defines a level that is functionally equivalent to R_2. However, there has been little investigation into the sensitivity of erosion predictability to the selected exceedance level.

Our observations suggest that the collision and overtopping regimes as well as erosion rates are better predicted by a lower exceedance level, R_{16}. Regression coefficients comparing runup statistics to eroded volume are maximum for R_{16}. While the maximum is not strong, there is no evidence that R_2 is better. Similarly, while R_2 measurements at times exceeded z_c, indicating the overtopping regime, there was no evidence for significant onshore sediment transport, as implied by Sallenger (2000) and Stockdon et al. (2007). Therefore, we suggest that although all the runup exceedance values tested were significantly related to the magnitude of dune erosion, the relevant statistic for dune erosion risk assessment should be lower than R_2. We recommend the use of R_{16} for predictive purposes.

Runup is known to depend on foreshore beach slope, but since natural beach profiles are typically concave, a number of interpretations of slope are possible. We examine predictability of runup (equation (2.23)) based on four different definitions of beach slope. In addition, slopes can be defined either by least squares or by end-point calculation. For hours 8 - 10 and 18 - 20 when runup was mostly confined to the foreshore, equation (2.23) serves as a good test of the various choices of slope. But for times of active dune erosion, the fit to equation (2.23) is not as good since this equation does not purport to represent runup statistics on such a complicated profile.

Comparisons of parameterized R_{16} with observations suggest that foreshore beach slope $\beta_{1\sigma}$, defined between $\langle\eta\rangle\pm\sigma_s$, produces better results than mean slope defined between the still water line and the dune base, β_s. However, the predictions associated with β_0, the time-independent slope from still water level to the dune base at the beginning of the storm, are almost equally as good and are considerably easier to estimate. Thus, the comparison supports the hypothesis of Stockdon et al. (2007), that the initial mean beach slope is a useful parameterization of slope when time dependent slope is unknown. The success of the parameterization with the initial beach slope also suggests that feedback between beach slope and runup may be of secondary importance.

Both least squares and end point methods for estimating beach slope were tested. The end point method was found to be noisier, consistent with the reduced degrees of freedom of the two-point solution. Least squares methods also typically yielded shallower slopes by reducing the relative weight of the steeper dune face compared to the flatter foreshore slope.

Runup data from hours 14.5 to 18 appear anomalous. Despite uniform wave conditions from hours 12 - 18 at the wave paddle (Figure 2.4), after hour 14.5 the foreshore beach slope rapidly steepens and runup levels drop. Since equation (2.23) predicts a positive relationship between these two variables, predictive models are unable to mimic this behavior, so error statistics are larger. It is not entirely clear why observed runup decreased, although it appears to be related to changes in the surf zone

beach profile. For the time period in question, in situ beach profiles indicate that a sand bar developed and moved offshore (Figure 2.20). Visual observations showed incident wave breaking over this bar through the peak wave period, hours 12-18, likely reducing incident swash magnitudes. Similarly, measured infragravity energy in the tank was also reduced, perhaps related to changes in the breakpoint-generated infragravity motions at the particular bar position (Symonds and Bowen, 1984). The physics of these observed changes deserves further investigation.

The parameterization of the dune base trajectory with equation (2.25) was reasonably accurate. However, the elevation of the dune base appears to be the weakest parameterization in the model. At hour 14, there is a rapid change in z_b, possibly due to the decrease in infragravity energy that is not accounted for by the assumption in equation (2.23). A strong connection appears to exist between trajectory of the dune base and eroded volume from the dune. We observed that the dune eroded to the point where the elevation of the base minimized contact between runup and the dune face and that the dune base and foreshore beach slope adjusted over the course of the experiment. This may indicate a change from slumping dominated transport at the dune face to energetics dominated transport of sediment off the foreshore. A model combining the processes of dune slumping through slope instability and swash zone sediment transport is needed to model the gradients in sediment transport resulting in exposing or limiting the dune scarp to runup. Further work is needed to parameterize the dune base trajectory in simple models, and

including dune slumping as a separate process may be necessary to model trajectory in a full cross-shore sediment transport model.

Given known forcing at the dune, equation (2.3) reproduced 64% of the observed variance in the observations. This suggests that many of physics of dune erosion are encapsulated by the forcing and C_s in equation (2.3). We also implemented equation (2.3) using offshore forcing and initial beach slope in a way that would be representative of a forecasting or hindcasting exercise. In this case, the model explained 49% of the observed variance, a 15% drop over known forcing, and bias and was nearly the same as for the known forcing, indicating that the parameterizations of forcing are relatively accurate.

In contrast to many dune erosion models which invoke an avalanching criteria based on a user defined maximum beach slope, we hypothesize that dune slumping should be modeled using an understanding of slope stability. For example, runup was in contact with the dune for approximately 45% of the time between hours 8 and 8.25, yet no slumping and little erosion of the dune was observed. At that time, the dune was relatively low sloping (tan β = 0.5), and although this exceeds the avalanching criteria for some models, no slumping occurred, suggesting that the slope was relatively stable. Later in the experiment, a steep scarp developed in the region where waves were active. Using the avalanching criteria, a steep scarp on a wet slope should not exist. In contrast, knowledge of slope stability suggests that the increase in shear strength due to capillary forces in the wet dune should produce the scarp that was

observed. Further work must be conducted to study the effect of infiltration of water into the dune, and the balance of forces on the scarp.

2.8 Conclusions

We have developed a new remote sensing technique for making three dimensional observations of the subaerial beach and dune under conditions of storm dune erosion. Observations were made at higher temporal and spatial resolution (every 15 minutes for the full profile; 0.04 and 0.10 m resolution in the vertical and horizontal, respectively, over the entire dune and foreshore surface) than is possible with traditional surveying methods. Bias of the stereo technique ranged between -0.03 m and 0.02m, depending on location of the dune and foreshore in the image. Root mean square difference between stereo observations and surveyed observations ranged between 0.03 m and 0.08 m, depending on image variance and smoothing of the dune crest by the correlation window. Errors were on the order of one to two pixels. A method to estimate confidence intervals based solely on image information was developed and found to be accurate.

We quantified the time-dependent wave runup and dune erosion during a wave tank-based dune erosion experiment modeled after an actual storm hydrograph. Based on observations, we found that R_{16} was the appropriate runup statistic for quantifying dune erosion, a less extreme statistic than the normally-accepted 2% exceedance value, R_2. We tested the dependency of R_{16} on beach slope with a number of beach slope estimators and found best results using $\beta_{1\sigma}$, the time-dependent least-squares

slope for the region within one standard deviation of the mean swash. Surprisingly, β_0, the time-independent least-squares slope between the still water line and the dune toe at the beginning of erosion, was nearly as skilled (and much easier to estimate), supporting the hypothesis of Stockdon et al. (2007) that β_0 is a reasonable estimate of foreshore beach profile during a storm.

The dune base eroded at a relatively constant trajectory along β_T, which was 0.54 β_0, roughly half way between a simple up-slope and a totally horizontal trajectory. This simple relationship has predictive skill for estimating retreat trajectory in the absence of detailed model for cross-shore sediment transport ($R^2 = 0.87$).

LEH04 includes a parameterization, t/T that is a proxy for number of runup collisions with the dune. An improved parameterization was developed, incorporating a Gaussian distribution for runup and elevation of the dune base. Most of the error in N_c can be attributed to error in elevation of the dune base

A simple model of dune erosion (a modified version of LEH04) that combines estimates of dune face exposure to runup with a proxy for the number of swash impacts successfully reproduced 64% of the observed variance with known forcing at the dune and 49% of the observed variance using parameterized offshore forcing. This suggests that forcing is well parameterized in the model, and that practical prediction using offshore wave conditions will be useful.
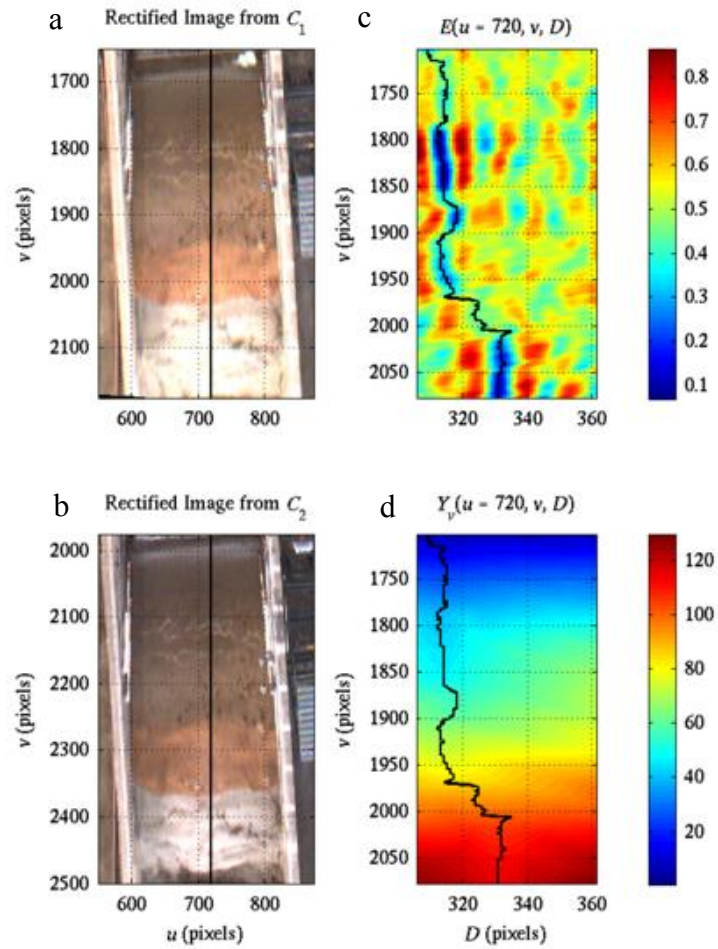
Figure 2.1. (a,b) Raw stereo pair of images with matching epipolar lines plotted, (c) evidence in the cross-shore direction for the epipolar line, (d) summed cost path for the epipolar line, with the minimum cost path plotted in black.
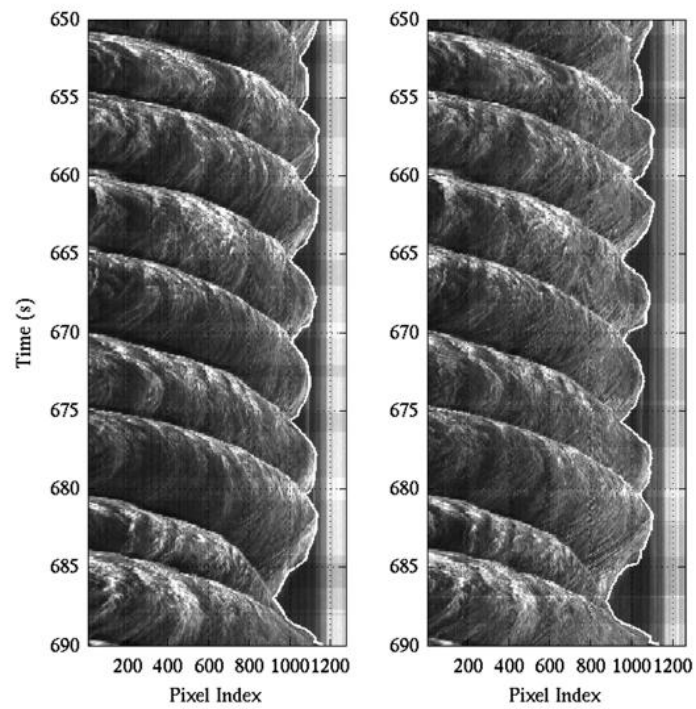
Figure 2.2 Time stacks of the cross-shore transect of pixels for C_1 (left) and C_2 (right). Bores are visible as the bright streaks moving from left to right across the images. The digitized runup edge is denoted by the solid line white line.
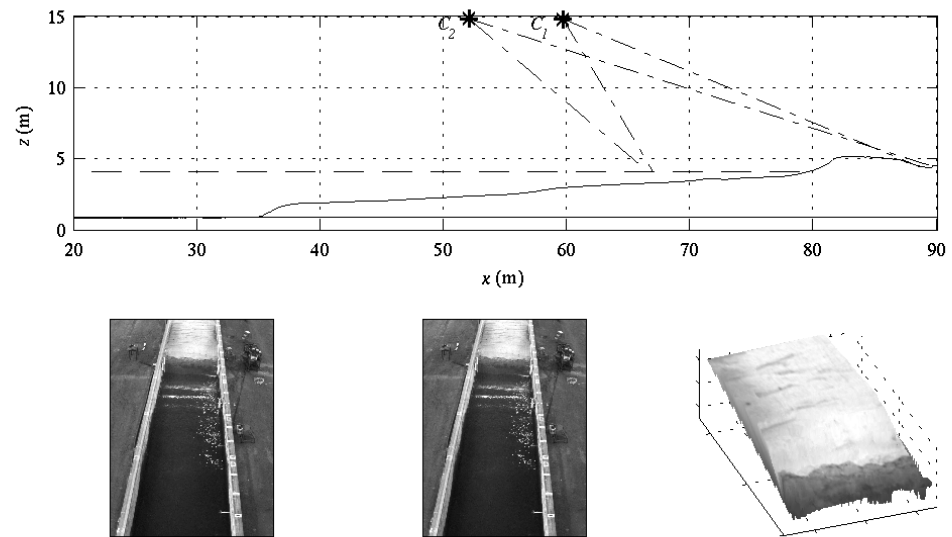
Figure 2.3 Elevation view of the beach profile and camera positions (upper panel). View from C_1 (left) and C_2 (middle), and stereo view of the dry beach with draped image (right).
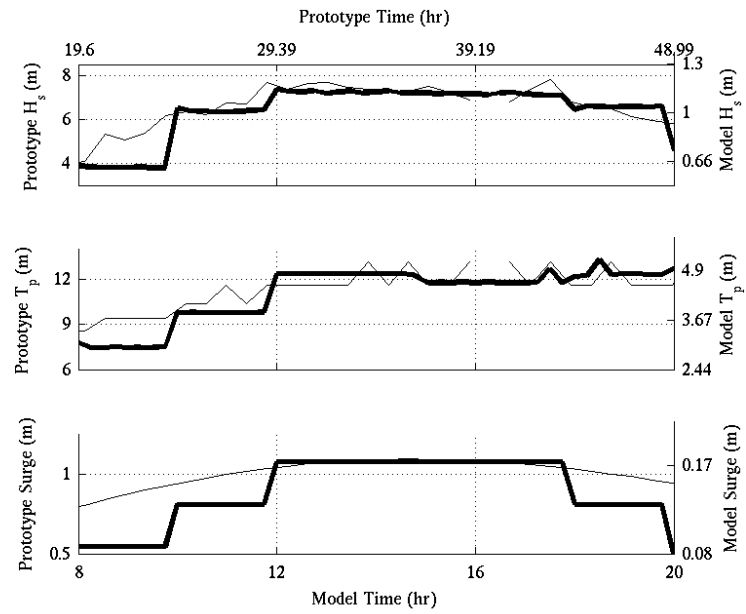
Figure 2.4 Prototype (thin line) and modeled wave conditions (thick lines) at the wave maker throughout the dune erosion experiment were based on observations of a Northeaster storm to reproduce the effect of variable conditions acting on a dune.
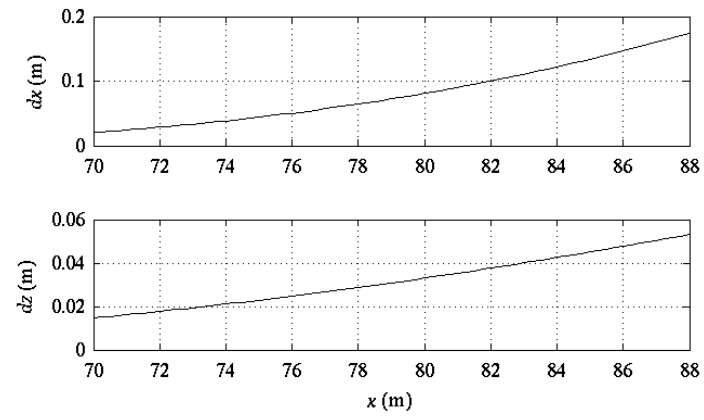
Figure 2.5 Theoretical resolution near the dune top from equation (2.8).
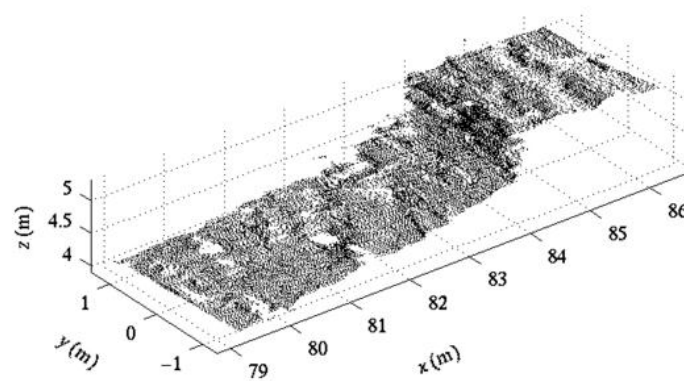
Figure 2.6 Each point represents a raw stereo estimate from a pixel for a scarped dune. Half of the raw points are plotted to allow better visibility of the dune.
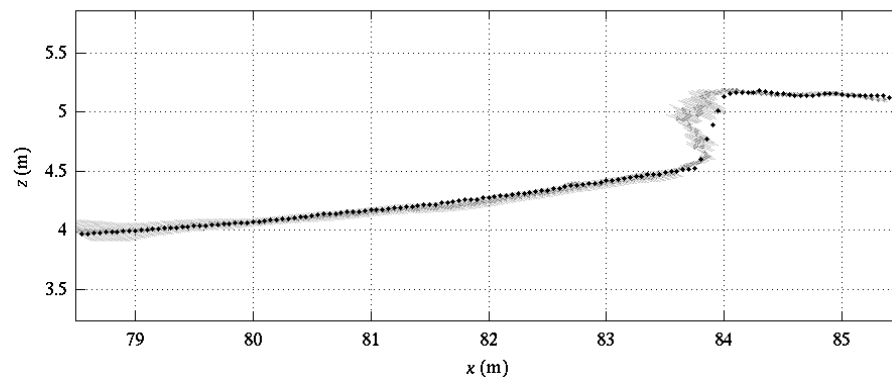
Figure 2.7 The smoothed stereo observations (gray dots) and error bars (gray lines) and a surveyed profile (black dots) at 13 hours into the experiment, when RMSE was largest for the whole experiment.
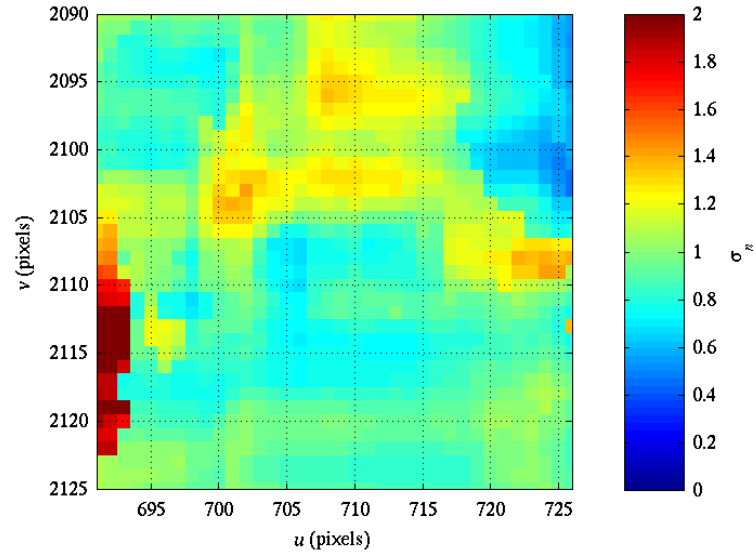
Figure 2.8 Plot of σ_n, the scatter in stereo results scaled by error bars. The error bars are representative of scatter in stereo observations because standard deviation of scatter scaled by error bars is 1 if error bars perfectly quantify scatter.
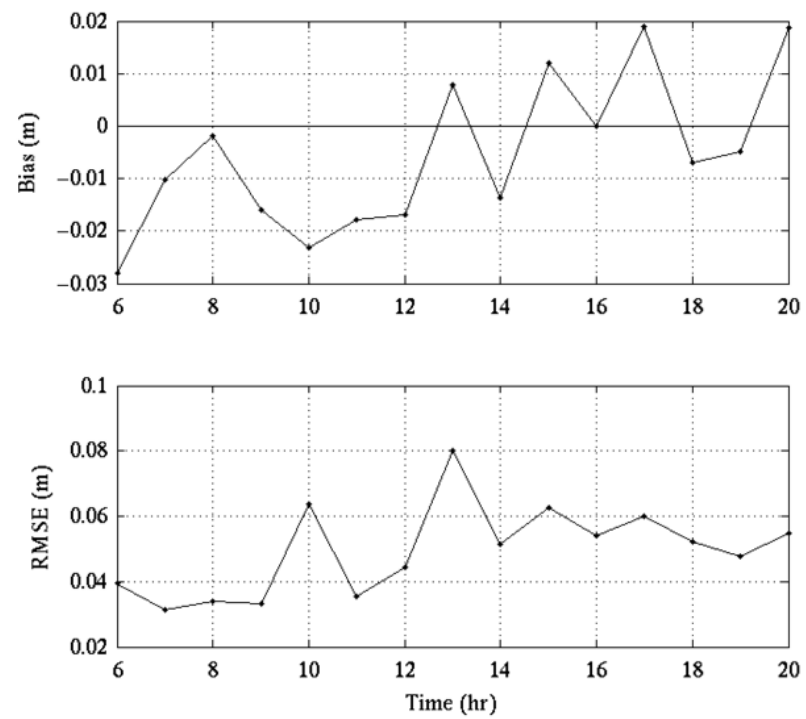
Figure 2.9 Plot of bias and RMSE between the stereo and surveyed profile over the experiment.
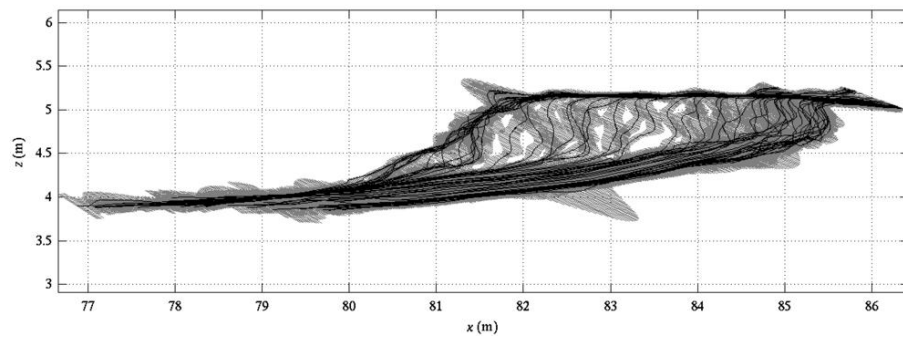
Figure 2.10 Beach profiles from stereo plotted every 15 minutes throughout the experiment with error bars plotted in gray. The dune base rapidly retreated leaving a steep scarp that migrated landward throughout the experiment.
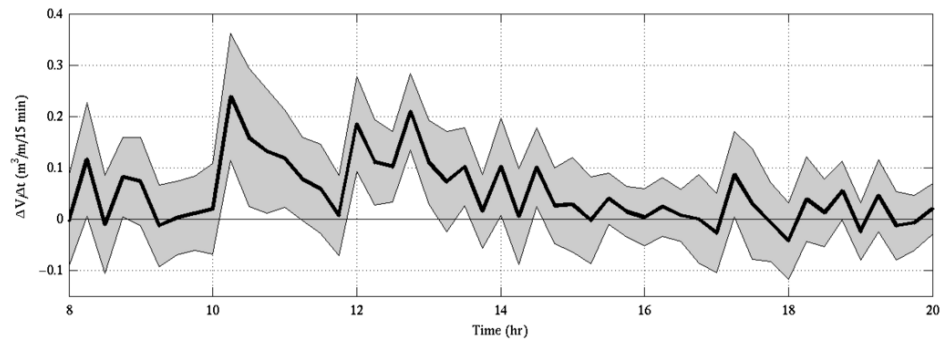
Figure 2.11 Volume of sediment eroded from the dune calculated with equation (2.22). Gray region defines the 95% confidence interval on volume change.
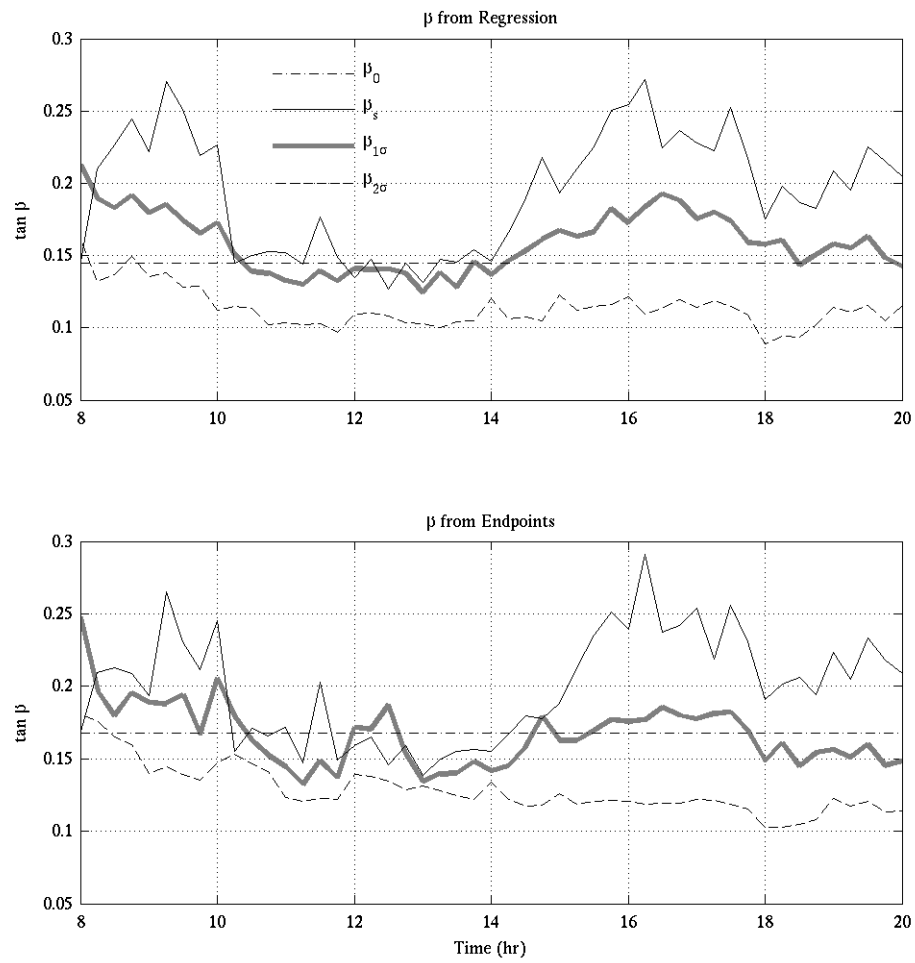
Figure 2.12 β from the four different definitions calculated using both the regression and endpoint methods.
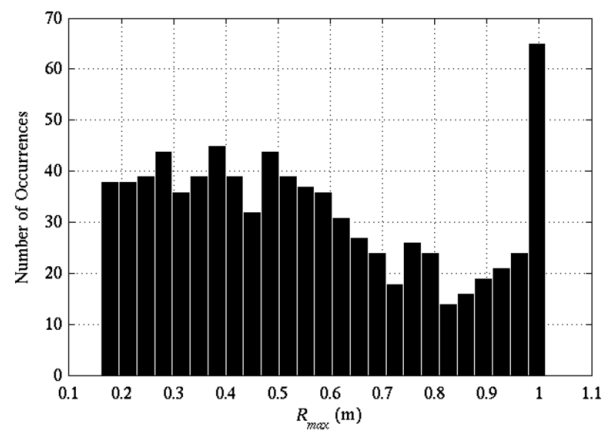
Figure 2.13 Truncated histogram of runup maxima between hours 12 and 14 when waves were overtopping the dune.
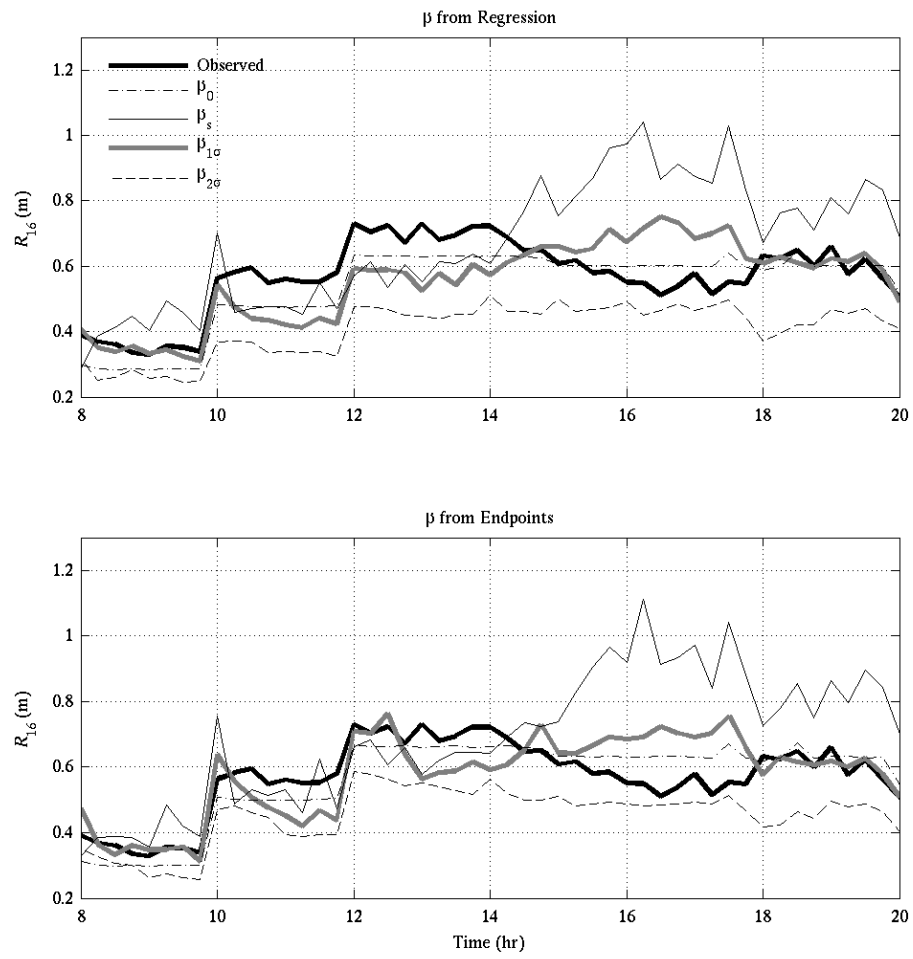
Figure 2.14 Observed R_{16} for the four different definitions of beach slope calculated using regression and end point methods.
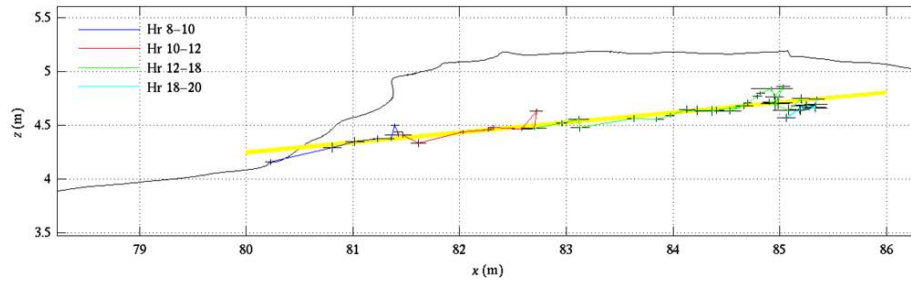
Figure 2.15 The initial beach profile and trajectory of the dune base over the experiment are plotted with error bars on the position of the dune base. The yellow line is the best fit line to the retreat trajectory (β_T).
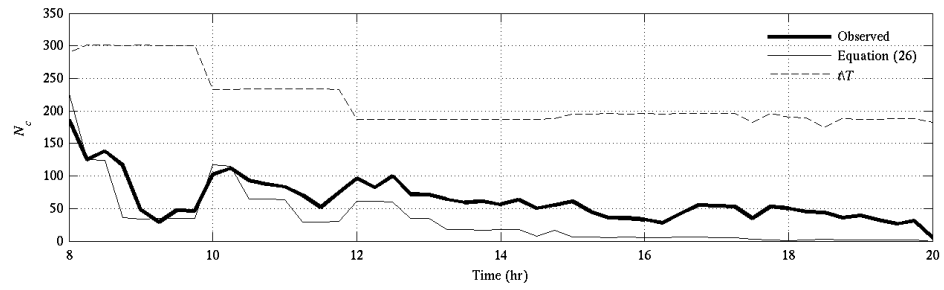
Figure 2.16 N_c observed compared with N_c modeled using equation (2.26) and N_c estimated using LEH04 parameterization of t/T.
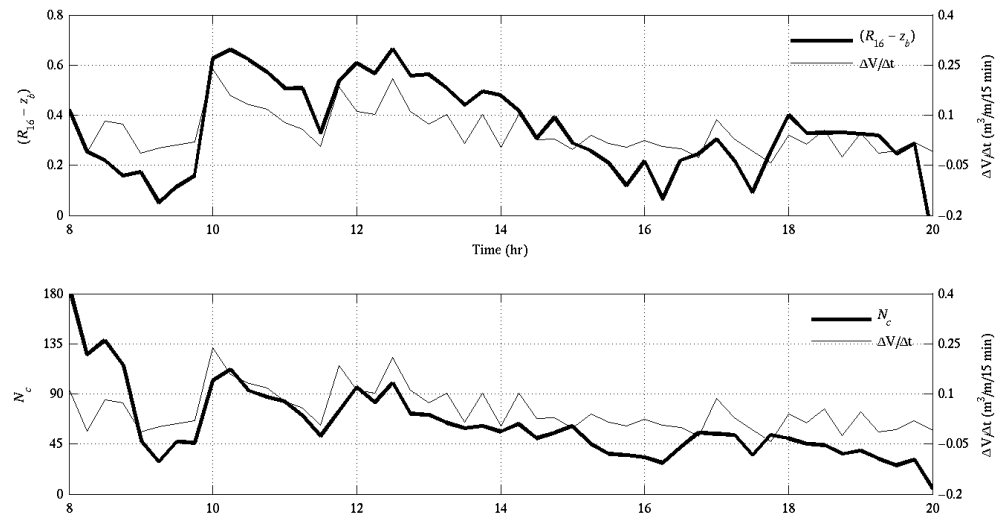
Figure 2.17 Observed forcing, $(R_{16} - z_b)$ (lower plot) and N_c (upper plot), compared with observed dune erosion volume. The squared-correlation were 0.60 and 0.37, respectively.
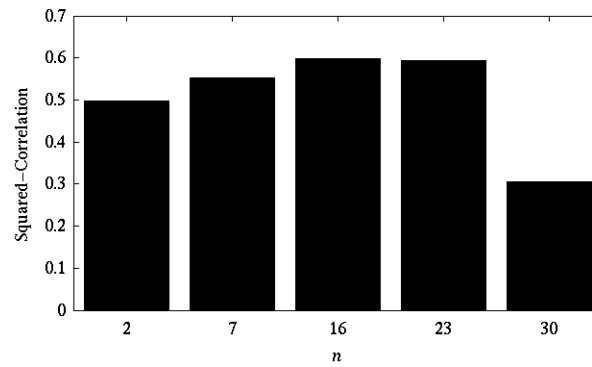
Figure 2.18 Bar graph showing squared-correlation between eroded volume and ($R_n -$ z_b) for the different exceedance values tested. R_{16} explained the most observed variance in eroded volume.
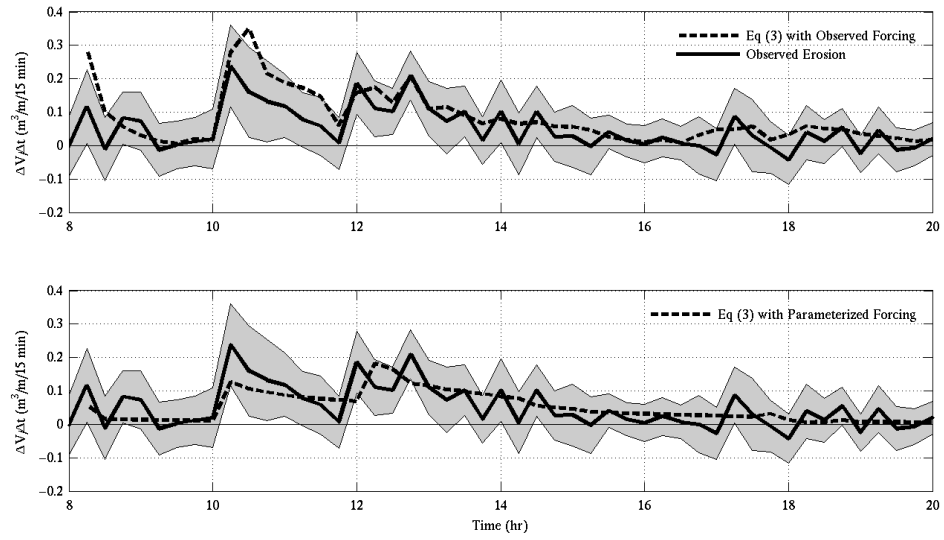
Figure 2.19 Results of LEH04, equation (2.3), with known forcing and beach profiles (upper plot) and LEH04 with parameterized forcing (lower plot) compared with observed dune erosion.
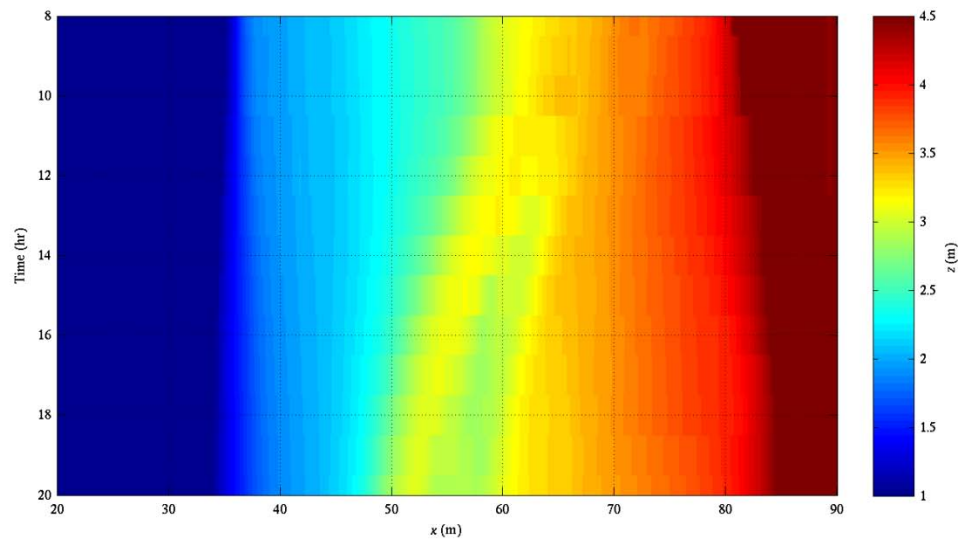
Figure 2.20 Time stack of the surveyed beach profile including the subaqueous beach. Between hours 10 and 12, a bar developed near $x = 62$ m then moved off shore for the remainder of the experiment.

Table 2.1 Wave conditions and measured runup during dune erosion.

Time (hr)	H_s (m)	T_p (s)	$\overline{R_2}$ (m)	σR_2 (m)
8 – 10	0.62	3.01	0.56	0.03
10 - 12	1.01	3.85	1.03	0.01
12 - 18	1.13	4.68	0.97	0.03
18 - 20	1.04	4.83	1.01	0.02

Table 2.2 Parameterization bias during dune erosion using regression slope.

Time (hr)	$\overline{\Delta R_{16}}$ equation (2.23) $\beta_s(t)$	$\overline{\Delta R_{16}}$ equation (2.23) $\beta_{1\sigma}(t)$	$\overline{\Delta R_{16}}$ equation (2.23) $\beta_{2\sigma}(t)$	$\overline{\Delta R_{16}}$ equation (2.23) $\beta_s(0)= 0.17$
8 – 10	0.06	0.01	-0.09	0.07
10 - 12	-0.06	-0.11	-0.22	-0.09
12 - 14	0.11	-0.13	-0.25	-0.08
14 - 16	0.16	0.01	-0.16	-0.02
16 - 18	0.38	0.16	-0.07	0.06
18 - 20	0.16	0.00	-0.19	-0.01
8 - 20	0.1	-0.01	-0.16	-0.03

Table 2.3 Parameterization rmse during dune erosion using regression slope.

Time (hr)	rmse ΔR_{16} equation (2.23) $\beta_s(t)$	rmse ΔR_{16} equation (2.23) $\beta_{1\sigma}(t)$	rmse ΔR_{16} equation (2.23) $B_{2\sigma}(t)$	rmse ΔR_{16} equation (2.23) $\beta_s(0)= 0.17$
8 – 10	0.09	0.02	0.09	0.07
10 - 12	0.10	0.12	0.22	0.09
12 – 14	0.12	0.14	0.25	0.08
14 - 16	0.21	0.08	0.17	0.04
16 - 18	0.39	0.17	0.08	0.07
18 - 20	0.17	0.03	0.19	0.03
8 - 20	0.21	0.10	0.17	0.06

Table 2.4 Parameterization bias during dune erosion using end point slope.

Time (hr)	$\overline{\Delta R_{16}}$ equation (2.23) $\beta_s(t)$	$\overline{\Delta R_{16}}$ equation (2.23) $\beta_{1\sigma}(t)$	$\overline{\Delta R_{16}}$ equation (2.23) $\beta_{2\sigma}(t)$	$\overline{\Delta R_{16}}$ equation (2.23) $B_s(0) = 0.17$
8 – 10	0.04	0.01	-0.06	0.02
10 - 12	-0.02	-0.01	-0.14	-0.05
12 - 14	-0.07	-0.06	-0.16	-0.06
14 - 16	0.14	0.02	-0.13	-0.04
16 - 18	0.41	0.16	-0.05	0.01
18 - 20	0.20	-0.01	-0.16	0.09
8 - 20	0.12	0.01	-0.11	0.00

Table 2.5 Parameterization rmse during dune erosion using end point slope.

Time (hr)	rmse ΔR_{16} equation (2.23) $\beta_s(t)$	rmse ΔR_{16} equation (2.23) $\beta_{1\sigma}(t)$	rmse ΔR_{16} equation (2.23) $B_{2\sigma}(t)$	rmse ΔR_{16} equation (2.23) $\beta_s(0) = 0.17$
8 – 10	0.06	0.03	0.06	0.05
10 - 12	0.10	0.10	0.14	0.06
12 – 14	0.08	0.09	0.16	0.05
14 - 16	0.20	0.08	0.13	0.04
16 - 18	0.41	0.16	0.06	0.10
18 - 20	0.25	0.03	0.16	0.04
8-20	0.21	0.09	0.12	0.06

Table 2.6 Empirical runup correction factor (K_d).

Time (hr)	K_d equation (2.23) $\beta_{1\sigma}(t)$	K_d equation (2.23) $\beta_s = 0.17$
10 - 12	1.26	1.12
12-14	1.23	1.19

3. AN INFILTRATION AND SLOPE STABILITY MODEL FOR DUNE EROSION

3.1 Abstract

Forecasting dune erosion prior to a storm or over longer periods requires knowledge of the forces driving dune erosion. To improve our predictive capability for dune erosion, we propose a new model where dune slumping occurs when water, which infiltrates horizontally into the dune, increases the over-burden sufficiently to destabilize the dune. Horizontal infiltration is driven by suction of water into the dune via capillary action and is a surprisingly strong process with rapid time scales. We also propose that the elevated pore water concentrations increase cohesion of the wetted sediments so that the entire volume of wetted sand slumps as a unit so erosion can be modeled based on the force balance on a sliding block. Several versions of this model were tested, including a numerical infiltration model, a simplified infiltration model, and a model based on offshore wave forcing, rather than known forcing at the dune.

The model was tested using data from a large scale laboratory experiment with a storm hydrograph to investigate the time dependence of dune erosion. The numerical infiltration and slope stability model with known forcing explained 72% of the observed variance in erosion rate, while the simplified infiltration and stability model explained 58% of the observed variance in erosion rate. Error statistics suggest that we capture the majority of the physics controlling dune erosion in this laboratory experiment and that the simplified model will be useful as a forecasting tool.

3.2 Introduction

Coastal sand dunes, like those found on the east coast of the United States, provide natural protection for landward lying assets including buildings, infrastructure, and ecosystems. When the combination of tide, surge, wave setup, and wave runup during extreme storms exceed the base of the dune, the system is vulnerable to erosion and landward-lying assets are at risk of being damaged. A predictive capability for modeling the vulnerability of dunes to extreme conditions would improve the quality of risk assessments in threatened areas. Probabilistic dune erosion forecasts of this type are needed on both short and long-term timescales to address storm event dune erosion as well as the cumulative effects of storms and sea-level rise. In both cases, simple models are needed for forecasting.

A useful quantity for estimating the vulnerability of a dune is the potential volume of sediment that may be eroded during a storm. Typically, these erosion rates are modeled based on one of two approaches. In the first, including the models EDune and XBeach (Kriebel and Dean, 1985; Roelvink et al., 2009a), dune erosion is dependent on an avalanching criterion when the dune face steepness exceeds a user-defined threshold. Changes in the sub-aqueous profile are based on cross-shore sediment transport models up to the shallowest location where hydrodynamics may be modeled, and a prescribed extrapolation from there to the shoreline. Each model of this type contains a different set of assumptions about which hydrodynamic process are important (Kriebel and Dean, 1985; Roelvink et al., 2009a; van Rijn, 2009; Vellinga, 1986) but all invoke an arbitrary avalanching criterion for the actual dune.

The second type of time-dependent dune erosion model is known as the wave

impact model (Fisher et al., 1986; Overton and Fisher, 1988; Overton et al., 1994a).

This model hypothesizes that volume of sediment eroded, ΔV, is proportional to the

force of wave impact, F

$$\Delta V = C_c \sum F \qquad (3.1)$$

where C_c is a calibration coefficient. F is the force of the bore at impact ($F = \rho u^2 h$)

where ρ is the water density, u is the velocity of the bore just prior to impact, and h is

the height of the wave just prior impact. Overton et al. (1994b) found that C_c

depended on grain size and compaction.

The wave impact model provided a basis for the dune erosion model of Larson

et al. (2004). In this model, ΔV is parameterized in terms of wave runup, R, above the

dune base, z_b, and time of exposure, t,

$$\Delta V = 4C_s (R - z_b)^2 \frac{t}{T} \qquad (3.2)$$

where C_s is a calibration coefficient dependent upon grain size and wave height and T

is incident wave period. Palmsten and Holman (in review) tested equation (3.2) using

detailed observations of runup and dune erosion from a large wave flume experiment.

They found that equation (3.2) explained 64% of the observed erosion volume.

Although the wave impact model has the advantage of directly addressing the

interaction between waves and sediments of the dune face, the assumption that the

volume of eroded sediment is dependent upon the normal force impacting the dune

face is not obvious, since slumping is caused by the balance of forces acting along failure planes within the dune not on normal forces. In fact, a normal force directed into the dune should provide a stabilizing rather than a destabilizing effect.

Erikson and Larson (2007) investigated the instability of undercut dunes that lead to slumping in their laboratory investigation of dune erosion. The size of the overhang was determined using an approach similar to equation (3.2). The presence of the overhang caused a bending moment and tension crack that were modeled using using elastic beam theory (Erikson et al., 2007). Using this approach, they were able to accurately model scarp recession distance (R^2 between model and observation was 0.90). However, their theory and observations were limited to the case of overhanging dunes and little erosion would occur in the absence of undercutting.

In a recent dune erosion experiment (Palmsten and Holman, in review), we made three observations that inform the hypotheses for a new dune erosion model. First, we observed that dune slumping occurred only after water had infiltrated the dune. Second, we observed that the slump usually involved only the wet portion of the dune sediments, leaving the scarp surface drier (Figure 3.1). Finally, we observed that the dune reached a stable state when the dune base eroded upward, so scarp height became smaller than some critical scarp height. These observations suggest the hypothesis that the excess weight of the pore water in the dune may provide the excess force needed for dune failure.

The overall objective of this work is to develop a simple model for dune erosion that accounts for the effect of infiltration due to the time-dependent exposure of dune sediments to waves. In the proposed dune erosion model, we invoke slope instability as the driving mechanism for dune slumping and infiltration of water into the dune as the dominant control on strength of the sediment and excess weight. We hypothesize that the dune erodes when the destabilizing force along the failure plane exceeds the resisting strength of the sediment. Furthermore, based on our observation that the wetted dune tended to slump, we hypothesize that the volume of material eroded from the dune is equivalent to the volume of material that has been infiltrated by waves, thus the eroded volume will be equal to the infiltrated volume, a simple principle for practical estimation.

In the next section of the paper, we describe the equations for infiltration of water into the dune and slope stability. In sections 3.4 and 3.5, we describe the experimental methods used in the wave flume experiment and the results of the experiment compared with different versions of the proposed dune erosion model. Finally, in sections 3.6 and 3.7, we discuss results and make conclusions.

3.3 Dune Erosion Model

We propose that dune slumping occurs when water, which infiltrates horizontally into the dune, increases the over-burden sufficiently and destabilizes the potential sliding mass. Horizontal infiltration is driven by the capillary action of water wicking into the dune and is a surprisingly strong process with rapid time scales. We

also propose that the elevated pore water concentrations increase cohesion of the wetted sediments so that the entire volume of wetted sand slumps as a unit so can be modeled based on the force balance on a sliding block.

3.3.1 Infiltration Model

In order to model infiltration of water into the dune, we use Darcy's Law for the flux of water, q (units of meters cubed per second per square meter of surface), through porous media

$$q = -K(\psi)\frac{\partial \psi}{\partial x} \qquad (3.3)$$

where K is the hydraulic conductivity in units of meters per second, ψ is the pressure head in units of meters of water, and x is the cross-shore axis. Both K and ψ are dependent on the volumetric water content of the pore spaces, θ. The relationship between these variables is given later in this section.

The flux of water into a relatively dry dune is driven by a process called matric suction. Matric suction is caused by the capillary force (twice the ratio between surface tension of the water and radius of curvature of the meniscus) when both water and air occupy the space between sand grains. In partially saturated sediment, the surface tension causes a compressive force on the sand grains, acting to hold the grains tightly together (McCarthy, 2007). As the amount of air in the pore space decreases, the radius of curvature of the meniscus increases, and as a result the matric suction decreases. By convention, pore water pressure head, ψ, under matric suction is

negative, so that the gradient in pressure between swash and unsaturated sediments drives flow into the dune.

Equation (3.3) is substituted into the continuity equation to determine infiltration of water into the dune (Richards, 1931)

$$\frac{\partial \theta}{\partial t} = -\frac{\partial}{\partial x} K(\psi) \frac{\partial \psi}{\partial x} \tag{3.4}$$

θ is the volumetric water content in units of m^3/m^3.

K describes the relative ease with which water flows through sediment and is a function of ψ, and both are a function of θ. Therefore, an expression for K is needed to solve equation (3.4). van Genuchten (1980) derived an analytical expression for K,

$$K(\psi) = \frac{1-(\nu\psi)^{n-2}[1+(\nu\psi)^n]^{-m}}{[1+(\nu\psi)^n]^{2m}} \tag{3.5}$$

where ν and n are parameters which must be estimated from sediment data and $m = 1-1/n$. ψ is related to θ (van Genuchten, 1980) as

$$\theta = \theta_r + \frac{(\theta_s-\theta_r)}{[1+(\nu\psi)^n]^m}. \tag{3.6}$$

where θ_r is residual water content, and θ_s is saturated water content.

When hydraulic properties are not directly measured, the values of the hydraulic properties θ_r, θ_s, ν, n, and $K(\psi)$ for a particular sediment type may be determined using a pedotransfer function (PTF) which relates hydraulic properties to sediment characteristics including percentage of sand, silt, and clay, median grain size,

bulk density, or percentage of organic content. Choice of PTF is important because it ultimately determines the rate of infiltration into the dune.

PTFs are typically developed using regression or neural network analysis on datasets where both the sediment and hydraulic properties are known. PTFs depend strongly on the dataset from which they are developed. Ideally, a PTF developed from a large database with a variety of sediment types, or one with similar sediment characteristics to the sediment of interest should be used (Wösten et al., 2001). We selected the PTF developed by Schaap and Leij (2000) since 43% of the samples from the calibration dataset were classified as sand. Plots of equations (3.5) and (3.6) using sediment characteristics and the Schaap and Leij (2000) PTF are shown in Figure 3.2.

Given sediment and hydraulic properties, equation (3.4) may be solved numerically using a model, for example Hydrus1D (Šimůnek et al., 2005), and the following boundary conditions. The pressure at the surface of the dune is taken to be 0 ($\psi = 0$ at $x = 0$) when waves are in contact with the dune since hydrostatic pressure below the swash surface is not included. When waves recede from the dune face, the boundary condition is altered to require that the flux of water into the dune is 0

($q = K(\psi)\dfrac{\partial \psi}{\partial x} = 0$ at $x = 0$) when waves recede from the dune. This no-flux boundary condition is also applied continuously at the interior boundary of the solution domain, away from infiltration. The dune is initially assumed to have $\theta = \theta_r$. The dune face

boundary conditions were alternated as a function of the presence or absence of wave runup on the dune scarp based on the measured runup time series from the experiment.

3.3.2 Simple Infiltration Model

The most accurate solution comes from solving equation (3.4) numerically using measured runup time series. However, this full solution is both complicated to execute and impossible to use in a predictive sense when time series data are unavailable. As a practical solution, we also explored a simplified representation of infiltration. In this representation, the dune face boundary was assumed to be constantly wetted ($\psi = 0$) for the integrated time that the dune was exposed to waves, then was assumed to be dry (no flux) for the remainder of each 15-minute analysis period representing the integrated time that the dune face was exposed to air.

This approach has two advantages. First, infiltration may be modeled using the full solution to equation (3.4) when the time series of swash on a dune is unknown, but an estimate of exposure period from offshore wave conditions is known. Second, a significantly more simple equation for infiltration into the dune may be implemented for the case of constant exposure, one which does not require a numerical model to solve.

Green and Ampt (1911) derived this simplified approach by assuming that the water infiltrated into the dune can be approximated by a region of constant water content, $\Delta\theta$, that has infiltrated a distance, Δx. The flux of infiltrated water, q, is related to the change in position of the wetted front as

$$q = \Delta\theta \frac{\partial x}{\partial t}. \qquad (3.7)$$

Green and Ampt (1911) assumed that the pore spaces in soil could be modeled as capillary tubes under steady flow conditions. Thus, the pressure gradient in Darcy's Law (equation (3.3)) can be represented by the bulk gradient, $\Delta\psi/\Delta x$. Combining Darcy's Law and equation (3.7), we can represent the horizontal distance of infiltration, Δx as a function of period of exposure, Δt,

$$\Delta x(t) = \left(\frac{2K\Delta\psi\Delta t}{\Delta\theta}\right)^{1/2} \qquad (3.8)$$

Green and Ampt (1911) showed that the wetted region is not entirely saturated for horizontal infiltration, so $\Delta\theta$ was set to 0.70, based on the average value of $\Delta\theta$ from solution of the Richards equation (equation (3.4)). Values for K and $\Delta\psi$ were determined using the same PTF as in the full model, but assuming full saturation, since the driving pressure head is the difference between the saturated swash and the dry dune sand.

The application of equation (3.8) is strictly for the cumulative time for which the dune was exposed to swash and will underestimate infiltration since diffusion that will continue to occur between swashes is neglected. We accounted for these differences in infiltration distance due to diffiusion by multiplying Δx from equation (3.8) with an empirical constant.

$$\Delta x_\Lambda = \Lambda\Delta x \qquad (3.9)$$

The value for Λ was calibrated using data collected between hours 10 and 10.25 of the dune erosion experiment.

3.3.3 Wave Runup Model

Ideally, the observed continuous time series of wave runup on the dune would be used as boundary conditions for the infiltration model. However, in most cases direct observations of wave runup are unavailable and only offshore wave data are available. One solution would be to run a time-dependent model over the known nearshore bathymetry to determine a full time series of runup. However, the bathymetry data required to execute this approach are rarely available. This approach would also add significant computational effort to the model.

An alternative, simpler to approach is to use empirical relationships for the surf zone transformation process to predict the statistics of runup based only on offshore wave conditions and a bulk measure of beach slope. Stockdon, et al. (2006) developed an equation relating the elevation of the highest 2% of wave runup, R_2, to offshore wave conditions based on video observations from 10 field experiments covering a range of beach types and wave conditions. The equation is based on the assumption of a normal distribution of swash elevations. The runup is composed of a contribution from the mean water level, $\langle \eta \rangle$,

$$\langle \eta \rangle = 0.35\beta(H_oL_o)^{1/2} \tag{3.10}$$

and a contribution from the standard deviation of swash, σ_s.

$$\sigma_s = \frac{[H_oL_o(0.563\beta^2+0.0004)]^{1/2}}{4} \tag{3.11}$$

where H_0 is the deep water wave height, L_0 is the deep water wave length, and β is the

pre-storm beach slope determined by regression on the beach profile between the still

water line and the dune base. The elevation of the highest 2% of runup is

$$R_2 = 1.1(\langle\eta\rangle + 2\sigma_s) \tag{3.12}$$

consistent with the statistics of a normal distribution.

Because equation (3.12) is based on the normal distribution, it may be

reformulated to give the cumulative time that elevation, z, on the dune was exposed to

swash

$$\Delta t(z_R + z_{swl} > z) = [P(z_R + z_{swl} > z)]t \tag{3.13}$$

where z_R is the elevation of the swash edge about the still water line, z_{swl} is the

elevation of the still water line, P is the cumulative normal distribution defined by $\langle\eta\rangle$

and σ_s, and t is the length of time modeled. Δt, may be inserted into equation (3.8) to

solve for depth of infiltration. Although equations (3.11), (3.12), and (3.13) were

developed assuming a single beach slope, Palmsten and Holman (in review) found

them to be reasonable estimators of extreme runup statistics on the dune.

3.3.4 Dune Stability and Eroded Volume

Once the weight of wetted sediment was determined using an infiltration

model, the frequency of slumping was determined by slope stability. Slope stability

depends upon the magnitude of forces which tend to produce failure and the forces that resist failure along the potential failure plane.

Here, we investigate the force balance to determine the stability of an unsaturated dune as water horizontally infiltrates the dune. The dune will be composed of two regions, one wetted by infiltration of water from waves and a second, drier region. The wetted region has a greater average density than the drier region because of the added weight of water. Up to the point of near saturation, the wetted region will have increased shear strength, and so will be assumed to behave as a single unit, resulting in a trapezoidal sliding block (Figure 3.3). Two planes define the sliding block, one plane passing through the base of the dune, with a second failure plane caused by vertical cleavage in the upper portion of the dune. The second plane is located at the boundary between the portion of the dune that has been infiltrated and the portion of the dune that remains at the initial moisture content.

The ability of the sediment to resist movement depends on the critical shear strength, τ_{cr}, for unsaturated sediment may be modeled as

$$\tau_{cr} = c + (\sigma_n - P_a)\tan\phi + (P_a - P_w)\Theta\tan\phi \qquad (3.14)$$

where c is cohesion with units of Pascals (Vanapalli et al., 1996). σ_n is normal stress on the plane of failure,

$$\sigma_n = \frac{W_w\cos^2\alpha}{\Delta x} \qquad (3.15)$$

where W_w is the weight the potentially unstable block in Newtons, due to both the weight of the sediment and infiltrated water. α is the failure plane. Δx is the length of the horizontal component of the failure plane in units of meters and $\Delta x/\cos\alpha$ is the length of the failure plane. P_a is pore air pressure expressed as gage pressure and is assumed to be 0 Pa. P_w is the pore water pressure in Pascals, and $P_w = \rho g \psi$. P_w is a negative value for unsaturated sediment as discussed in section 3.3.1, $\Theta = \left(\frac{\theta - \theta_r}{\theta_s - \theta_r}\right)$, and ϕ is the internal friction angle.

τ_{cr} is composed of three terms. The first term accounts for cohesion, the additional strength provided to sediment by electrostatic forces or cementation, which is near 0 Pa for dune sand containing a minimal amount of clay. The second term accounts for the stabilizing frictional force on the shear plane, due to the reaction to weight of overlying sediment.

The final term accounts for the effect of apparent cohesion, sometimes known as the "sandcastle effect", due to the presence of unsaturated pore space (Hornbaker et al., 1997). This term is significant because the additional shear strength gives unsaturated dunes and sandcastles the ability to produce very steep scarps, or overhangs, as water content increases, up to a point where strength begins to decrease (Figure 3.4). Apparent cohesion is a function of the normalized surface area over which matric suction acts. Vanapalli et al. (1996) found that the normalized area was well predicted by the relative volumetric water content, Θ.

α, the failure plane, is the least stable angle within the dune. It is the angle where the difference between the destabilizing shear stress, τ_s, and the critical shear stress is the maximum, and may be determined by finding the zero derivative of τ_s - τ_{cr} as a function of α. τ_s is

$$\tau_s = \frac{W_w \sin \alpha \cos \alpha}{\Delta x} \qquad (3.16)$$

in Pa/m alongshore. Solving the derivative yields,

$$\alpha = \frac{\pi}{4} + \frac{\phi}{2} \qquad (3.17)$$

relating the failure plane to ϕ, the internal friction angle, a characteristic of the sediment. The failure plane is assumed to pass through the base of the dune. Assuming a failure along α has been shown to accurately quantify the stability of bluffs (Lohnes and Handy, 1968) and was also shown to contribute to the failure of overhanging dunes (Erikson et al., 2007).

Unlike water, pressure in sediment is anisotropic because its matrix supports a fraction of its weight. In a vertical scarp, the resulting lateral earth force is directed outward. In engineering, retaining structures are frequently built to resist lateral earth force (McCarthy, 2007). The magnitude of the lateral earth force, for cohesive soil at the moment when a vertical scarp will fail was derived by Terzaghi and Peck (1967). Here, we substitute equation (3.14) into the derivation, to describe the shear strength of unsaturated sediment, where both the apparent cohesion due to the presence of

water opposes the lateral earth pressure, as well as cohesion. Integrating over the dune

face yields the net lateral force, E. Using geometry to relate shear strength (τ_{cr}) and

normal stress (σ_n) to the horizontal (σ_h) and vertical (σ_v) components of stress

(McCarthy, 2007) when τ_{cr} and τ_s are balanced,

$$\tau_s = \frac{\sigma_h - \sigma_v}{2} \sin 2\alpha \qquad (3.18)$$

and

$$\sigma_n = \frac{\sigma_h + \sigma_v}{2} + \frac{\sigma_h - \sigma_v}{2} \cos 2\alpha \qquad (3.19)$$

Substituting equations (3.18) and (3.19) into equation (3.14) yields

$$\sigma_h = \frac{2c}{\tan \alpha} + \frac{\sigma_v}{\tan^2 \alpha} + (-P_w)(\Theta)\left(1 - \frac{1}{\tan^2 \alpha}\right) \qquad (3.20)$$

The fraction of vertical pressure transferred to the horizontal direction is $\tan^{-2} \alpha$ and is

known as the coefficient of earth pressure (Terzaghi and Peck, 1967). σ_v at depth (z_c-

z), where z_c is the elevation of the dune crest, depends on pressure of the sediment

above, so $\sigma_v = \rho_s g(z_c\text{-}z)$, where ρ_s is the bulk density of sediment, and g is gravitational

acceleration. Integrating σ_h over the dune face yields

$$E = \frac{\rho_s g \Delta z_D^2}{2 \tan^2 \alpha} - (-P_w)\Theta\left(1 - \frac{1}{\tan^2 \alpha}\right) \Delta z_D \qquad (3.21)$$

The effect of the second term allows the direction of E to vary based on the

magnitude of the apparent cohesion and the height of the dune scarp. When the first

term in equation (3.21) is larger than the second, E will be directed out of the dune and

contribute to the destabilizing force along the shear plane. However, when the contribution from the apparent cohesion exceeds the lateral earth force, E will be directed into the dune and provide a stabilizing force along the shear plane.

Lohnes and Hardy (1968) derived a force balance for loess bluffs composed of homogeneous, cohesive sediments with tension cracks assuming a trapezoidal sliding block. Here, we take a similar approach, but substitute equation (3.14) into the derivation, and assume a tension crack did not exist. The forces producing and resisting failure will be compared to determine when the dune will be subject to failure.

Given the typically steep slopes associated with eroding dunes, dunes may become unstable due to shear failure when the destabilizing force, D_w, exceeds the resisting force associated with shear strength of the sediment (S_w) (Figure 3.3).

D_w is defined as,

$$D_w = W_w \sin \alpha + E \cos \alpha \qquad (3.22)$$

To determine stability of the dune under homogeneous conditions, the shape of the unstable slab is assumed to be trapezoidal so

$$W_w = (\rho_s g + \rho g)\left(\Delta z_D - \frac{\Delta x \tan \alpha}{2}\right) \qquad (3.23)$$

Where ρ_s is the bulk density of sediment and ρ is the density of water. E is the net lateral earth force acting on the scarp in Newtons. E will be derived and discussed

further later in this section. Δx now represents the average distance of infiltration into the dune, assuming that the wetted sediment may be treated as homogeneous, and the dune scarp is vertical.

The resisting force on the wetted block, S_w, depends on both the shear strength along the plane, α, and includes a term due to the tensile strength of the dry sand resisting movement along the vertical plane of weakness between Δz_v. The tensile strength may be determined by substituting apparent cohesion, the third term from equation (3.14) into the definition for tensile force from Lu et al. (2009) yielding $T = 2(-P_w)\Theta \tan \phi \tan \left(\frac{\pi}{4} - \frac{\phi}{2}\right)\Delta z_v$, resulting in the final equation for shear strength of the wetted block

$$S_w = \left(W_w \cos \alpha + E \sin \alpha + (-P_w)\Theta \frac{\Delta x}{\cos \alpha}\right)\tan \phi +$$

$$2(-P_w)\Theta \tan \phi \tan \left(\frac{\pi}{4} - \frac{\phi}{2}\right)\Delta z_v \quad . \tag{3.24}$$

When the D_w exceeds S_w, we assume all sediment transport from the dune is due to the slumping caused by slope instability. Next, the wetted volume of sediment is defined as $\Delta V_w = \sum \Delta x(z)\Delta z_r$, where Δx is the horizontal distance water has infiltrated the dune and Δz_r is the vertical resolution of the dune scarp. Based on observations, we assume that when the wetted volume slumps the eroded volume is $\Delta V_E = \Delta V_w$.

3.4 Dune Erosion Experiment

Observations of dune erosion in nature are not readily available because of challenges in acquiring data during storm conditions. Therefore, we conducted a dune erosion experiment in the large wave flume at the Oregon State University Hinsdale Wave Research Lab. The large wave flume is 103 m in length, 3.7 m wide, and 4.6 m deep. The offshore end of the tank was equipped with a flap wave maker, and the onshore end of the tank had a beach made of Oregon beach sand (D_{50} = 0.23 mm). The sediment consisted of 94.50% sand 2.51% silt, and 1.99% clay, based on grain size analysis of dune sediment, and organic materials composed < 0.01% of the sediment. Bulk density of the sediment was 1.67 g/cm^3. The initial beach profile consisted of a low sloping subaqueous beach (tan β = 0.04), and a more steeply sloping dune (tan β = 0.5). Wave conditions were designed to be representative of a Northeaster Storm that occurred near Assateague Island, MD/VA in February 1998. Wave height, period, and water level in the tank were adjusted to reflect prototype storm conditions observed at National Buoy Data Center Buoy 44004 off Cape May, NJ. Irregular waves were generated by the wave-maker using a TMA spectrum. The time series of wave conditions at the wave maker and the initial beach profile are shown in Figure 3.5.

Wave forcing on the dune was determined by making observations of the time varying vertical elevation the shoreline. The location of the runup edge along the center of the wave flume was determined as a function of time by digitizing the

wave/beach intersection from video observations (Holman and Stanley, 2007) using a semi-automated routine (Palmsten and Holman, in review). Then the digitized pixel location of the runup edge was projected onto the beach profile to determine the continuous time series of wave runup on the beach. The time series of runup elevation was used as input to the Hydrus1D model for horizontal infiltration of water into the dune.

The dune response to wave forcing was determined using stereo video observations of the beach surface every 15 minutes throughout the experiment (see Palmsten and Holman (in review), for a full description of the experimental setup and data quality). Full profiles of the subaerial beach, along with error estimates were calculated from the video observations. Resolution of the dune was 0.1 m in the horizontal and 0.04 m in the vertical. Errors in the stereo technique were on the order of 0.02 – 0.08 m when compared with in situ surveys. Volume of eroded sediment was determined by subtracting consecutive profiles and integrating the difference in elevation between the dune base and the dune crest.

3.5 Results

Our analysis of the infiltration and slope stability model will be divided into three major sections. First, we will present experimental observations of dune erosion and wave forcing. Next, we will evaluate the infiltration and the slope stability model solved using the Richards equation and forced with known conditions by comparing predicted erosion rate with observations. The numerical model will test our

understanding of the physical processes causing dune slumping, although we do not measure infiltration. Finally, in order to develop a practical approach to modeling dune erosion, the simplified modeling approach will be compared with observed erosion rates in two steps. This simplified approach is representative of a situation where dune erosion must be forecast over a large region, just prior to passage of a hurricane when only offshore wave forecasts are available. In the simplified approach, erosion will first be determined using the combined infiltration and stability model where infiltration is determined by the modified Green-Ampt equation, equation (3.9), with known forcing to test the reliability the equation. Then, the infiltration and stability model will be solved with modified Green-Ampt equation forced with offshore wave conditions, equation (3.13), to test the efficacy of using the parameterized forcing.

3.5.1 Observations of wave forcing and dune erosion

Dune erosion is forced by swash interaction with the dune. Here, we present observations of swash duration on the dune and resulting dune erosion. The fraction of time that the dune was observed to be exposed to swash is shown in Figure 3.6. Regions of the beach below the dune base are shown in white. The beach profiles from stereo observations and erosion rate are shown in Figure 3.7 and frequency of slumping events is shown in Figure 3.8.

Combining information from Figures 3.6, 3.7, and 3.8, the complex relationship between wave forcing and dune response may be synthesized. Initially,

the base of the dune was low on the beach, and swash contacted the dune more than 30% of the time. As the dune base eroded upwards between hours 8 - 9, dune exposure to swash decreased. Between hours 9.25 – 10, no slumping occurred, but the dune base elevation decreased.

When wave forcing and surge increased at hour 10, the dune base decreased in elevation, increasing dune exposure to waves. During constant conditions between hours 10 – 12, the elevation of the dune base again increased, limiting dune exposure to swash, resulting in a corresponding decrease in eroded volume of sediment. Slump frequency was 1 slump per 15 minute period, except at hour 11.25, when two slumps were observed. Slump volume decreased over this 2 hour period of constant wave conditions.

Flux from the dune increased after hour 12, when wave height, period and still water level increased to a maximum. Then flux decreased as the dune base eroded upward under continued constant wave conditions between hours 12 - 14. After hour 14, slumping events became more intermittent and eroded volume decreased. Between hours 16 and 18, the elevation of the dune base decreased. Stereo calculations suggest the dune eroded between hours 17 and 17.25 although no slump was observed in the video observations. Also, this rapid erosion is followed by a relatively large dune accretion event between hours 18 and 18.25. Since no mechanism for dune erosion was observed, and it was followed by an accretion event that was also not observed, it is likely that the event between hours 17 and 17.25 was

erroneous. Finally, the elevation of the dune base increased between hours 18 – 20.5, limiting exposure of the dune to waves. Dune slumping ceased after hour 19.5.

3.5.2 Comparison of Full Model Results and Observed Erosion

The basic premise of this dune erosion model is that infiltration of water into the dune adds excess weight, causing it to slump. We first assumed the dune was unstable for the entire experiment to test the model assumption that volume of sediment infiltrated by water is proportional to the volume of sediment eroded from the dune. In this approach the Richards equation, equation (3.4), was solved using known forcing and beach profiles and the force balance the ratio of destabilizing to stabilizing forces, S_w / D_w, is assumed to be less than 1.

The volume of infiltrated sediment was compared with observations of eroded volume throughout the experiment (Figure 3.9, upper panel). Simply assuming that the dune was unstable throughout the experiment and the infiltrated volume determined with the Richards equation was proportional to eroded volume reproduced 64% of the observed variance in erosion, suggesting that infiltration is an important component of dune slumping. Bias in eroded volume from the Richards equation was 0.02 m^3/m/15 min and root mean square error (RMSE) was 0.04 m^3/m/15 min. The peaks in erosion at hours 10.25, 12, and 12.75 were underestimated, while erosion after hour 14 was overestimated.

Next, rather than assume that the dune was always unstable, it was only allowed to erode when the magnitude of D_w exceeded S_w. The ratio of S_w to D_w is

shown in Figure 3.9 (lower panel). Setting modeled erosion rate to 0 m^3/m/15 min

when the dune was stable yields an estimate of dune erosion including slope stability

(Figure 3.9, middle panel). This model explained 72% of the observed variance in the

observed eroded volume, an improvement over the assumption of a constantly

unstable dune. Including slope stability, the model predicted little erosion after hour

14.75 better matching observations, rather than over-predicting erosion as in the

previous case. Including a slope stability estimate decreased bias to -0.01 m^3/m/ 15

min, while RMSE remained the same at 0.04 m^3/m/15 min. However, the dune was

predicted to be stable hours 8.5 – 9, while dune slumps were observed during this

period.

3.5.3 Simplified Infiltration Model

In an effort to produce the most simple dune erosion model possible, we

explored the Green-Ampt equation, equation (3.8), as an alternative to the numerical

solution of the Richards equation. The most significant difference between these two

equations is that equation (3.8) neglects the diffusion of water. To determine the

effect of neglecting diffusion, particularly for the periods when the dune was not

exposed to swash, we solved the Richards equation using three different time

dependent boundary conditions for the period between hours 10 and 10.25 and

compared the results with distance of infiltration determined using the Green-Ampt

equation. Distance of infiltration was quantified as the minimum distance into the

dune where moisture content remained at θ_r. The results of this test are plotted in

Figure 3.10. First, the depth of infiltration was determined using Richards equation and known runup conditions (Figure 3.10, left bar) as the control. Next, infiltration was modeled using the Richards equation and a boundary condition where the dune was exposed to water continuously for the same period as in known conditions, the model continued to run while the water level was dropped for the remainder of the 15 minute period modeled to allow continued diffusion of water into the dune (Figure 3.10, center left bar). Then, infiltration was modeled using a boundary condition where the dune is exposed to water continuously for the same period as in known conditions then the simulation is stopped (Figure 3.10, center bar), so that diffusion when water was not in contact with the dune did not occur.

Two simpler approaches were also tested. First, infiltration was determined using a boundary condition where dune was exposed for the same period as in known conditions and infiltration was determined with the Green-Ampt equation assuming the wetted region of the dune was saturated (Figure 3.10, center right bar). Second, infiltration was determined with the same boundary condition and Green-Ampt equation. However, the wetted region was assumed to be 70% saturated rather than fully saturated, consistent with the average saturation of the wetted portion of the dune at the last time step of the Richards equation solutions for infiltration.

The model results for the different boundary conditions were compared with the control. Assuming the dune was continuously exposed to runup, then, dry for the remainder of the 15 minute period modeled (Figure 3.10, center left bar), the

infiltration was 94% of that modeled with the known runup time series. This result demonstrates that the actual runup time series is not required to reproduce most of the infiltration into the dune.

Assuming continuous exposure, but not including the extra time for diffusion of moisture when the wave was not in contact with the dune produced an infiltration distance that was 56% of the infiltration distance modeled with the known time series (Figure 3.10, center bar). Therefore, diffusion into the dune is an important component of the total infiltration of water into the dune.

Modeling infiltration with the Green-Ampt equation assuming the wetted portion of the dune was saturated resulted in an infiltration distance that was 67% of the infiltration distanced modeled with the Richards equation and the known time series (Figure 3.10, center right bar). The Green-Ampt equation, which does not include diffusion of water into the dune, resulted in and infiltration distance that was within 11% percent of the Richards equation solution when diffusion of water into the dune when during non-contact times was excluded.

Infiltration modeled with the Green-Ampt equation assuming 70% saturation produced an infiltration distance that was 83% of the infiltration distance modeled using the Richards equation and the known time series (Figure 3.10, right bar). This suggests that neglecting diffusion can be partly accounted for by decreasing the water content from full saturation to 70% saturation.

Based on the ratio between infiltration distance from the Green-Ampt equation with 70% saturation and the infiltration from the Richards equation, the coefficient, Λ, in equation (3.9) was set to 1.2. The combination of setting the saturation to 70% and appling the coefficient, Λ, accounts for the diffustion

The modified version of the Green-Ampt equation, equation (3.9), with the assumption that the dune was always unstable, was compared with observations of eroded volume (Figure 3.11, upper panel). The simplified version of the infiltration model produced error statistics nearly identical to the full infiltration model. The modified Green-Ampt equation reproduced 66% of the observed variance in erosion, approximately the same results as the Richards equation. Bias in eroded volume from the modified Green-Ampt equation was 0.00 m^3/m and RMSE was 0.04 m^3/m. As in the full model, peaks in erosion at hours 10.25, 12, and 12.75 were under estimated, and erosion was over predicted after hour 14.

Next, the slope stability model was included with the simplified model (Figure 3.11, middle panel). In this case, the erosion model reproduced 71% of the observed variance, a similar improvement as was found with the full model. Bias in eroded volume from the combined simplified slope stability model was -0.02 m^3/m/15 min and RMSE was 0.05 m^3/m/15 min. After hour 14.75, D_w exceed S_w (Figure 3.11, lower panel) and the dune no longer eroded, again matching well with observations of minimal slumping during this period.

3.5.4 Offshore Wave Forcing

Now that the ability of the Richards equation and slope instability to capture the physics of dune erosion has been demonstrated, and the simplification to the infiltration model has been made, the effect of using offshore wave forcing to predict exposure of the dune to swash, equation (3.13), and resulting dune erosion was tested. Wave height and wave period measured at the wave-maker were used as offshore forcing. First, modeled mean water level, standard deviation of swash, and equation (3.13) were compared with observations (Figure 3.12) to determine the error associated with statistically representing the transformation of waves through the nearshore region. Modeled mean water level explained 81% of the observed variance, model bias was 0.14 m, and model RMSE was 0.14 m. Modeled standard deviation of swash explained 81% observed variance, model bias was -0.05 m^3/m/15 min and RMSE was 0.06 m^3/m/15 min. These error statistics demonstrate that although the original runup parameterization by Stockdon et al. (2006) was developed for conditions where waves did not interact with the dune, it can be extended to the case of interaction with the dune with significant skill.

Next, erosion was determined using infiltration from the modified Green-Ampt equation, offshore wave forcing, and the assumption of an unstable dune, to test the effect of parameterized forcing (Figure 3.13). This model formulation explained 38% of the observed variance, a decrease from known forcing. Bias was 0.03 m^3/m/15 min, and RMSE was 0.06 m^3/m/15 min. Peaks in erosion at hours 10.25 and 12 were

underestimated, and eroded volume was nearly always over-estimated after hour 13. Including the slope stability component of the model improved explanation of observed variance to 58%. Bias was reduced to 0.00 m^3/m/15 min, and RMSE was reduced to 0.05 m^3/m/15 min.

3.6 Discussion

The dune erosion model developed in this paper is based on the idea that the infiltration of water into the dune and slope stability are the driving mechanisms for dune slumping. The comparison between observations and the full model suggests that these processes contribute significantly to the slumping ($R^2 = 0.72$), and we have captured the bulk of the processes causing dune erosion. It is informative to consider the three different periods during the experiment when the model under-predicted the observed erosion, to understand which processes might control the observed variance in erosion that were not explained.

Slumps occurred between hours 8.5 and 9 that were not explained by the stability model, and, in fact, the ratio of S_w to D_w suggests that the dune should be quite stable. Three observations suggest that slump forcing was slightly different at this time. First, runup was confined to the lower portion of the dune, and did not cover the entire dune scarp as it did later in the experiment. Second, video observations suggest that the dune may have undercut during this time. Finally, the dune slumped, the failing block overturned and did not erode back to dry sediment, as it did in the rest of the experiment. Together, these observations suggest that

overturning moments may have caused the dune to slump between hours 8.5 and 9. In order to model this situation, a mechanism for undercutting and elastic beam theory (Erikson et al., 2007) should be included.

The model under-predicted the eroded volume at hours 10.25, 12, and 12.75. At these times, the images show that a significant amount of dry sediment continued to fall after the wetted portion of the dune gave way. Slumping of dry sediment continued until the next wave impacted the dune, increasing shear strength of the sediment. Ideally, once the initial slump of wet sediment occurred, slope stability of the remaining dry sediment could be determined. Using the model developed here, this is difficult for two reasons. First, after the wet sediment slumps, the elevation of the dune base increases due to the slumped material in front of the scarp. Our model assumes the dune is composed of a vertical scarp, and does not account for this change in morphology. Second, we do not resolve slope stability on a wave time scale, so the sequence of wet slump, dry slump, and then runup of the wave to increase shear strength of the dry sediment is not explicitly modeled.

The slope stability model predicted little slumping after hour 14.75. Video observations suggest that a small volume of sediment eroded after this period when the scarp height increased and the dune became unstable. However, stereo observations show both positive and negative change, but at most small net erosion. Since there is no known mechanism for dune re-building, we credit the increase in volume at hour 18 to measurement noise, consistent with the error bars shown in Figure 3.11.

In order to develop this simple model, several assumptions were made for both the infiltration model and the slope stability model. The following paragraphs describe those assumptions.

The above solutions to the infiltration model required the choice of a PTF to relate observed soil characteristics to required hydraulic properties. The chosen PTF (Schaap and Leij, 2000) was selected as the most representative of the dune sand used in this experiment. However other PTF functions have been published (Rawls and Brakensiek, 1985; Vereecken et al., 1990) based on generally different soil types that would have yielded different hydraulic properites, hence predicted erosion rates. Similarly, even the selected PTF will be sensitive to errors or variability in soil properties. For example, in the practical application of a dune erosion model over a large area, just before a storm, the grain size distribution needed as input to the PTF may not be known. To get an initial feel for the sensitivity to errors in sediment characterization, we investigated the variations in infiltration with example variations in sediment properties.

Given sediment characteristics of dune sand (94.5% sand, 2.51% silt, and 1.99% clay in this study), we found the Shaap and Leij (2000) PTF to be sensitive to the fraction of sand in the grain size distribution. To demonstrate this sensitivity we calculated infiltration distance between hours 10 and 10.25 in the experiment using 6 different grain size distributions in addition to the observed distribution. The model predicts a 42% decrease in infiltration distance if the sand fraction is decreased from

100% to 95%, and a 43% decrease in infiltration when the sand fraction was decreased from 95% to 90%. The model was less sensitive to variation in the small fraction of silt and clay expected in dune sand. Assuming a grain size distribution with 95% sand, 5% silt, and 0% clay produced infiltration distances within 8% of the infiltration produced by a grain size distribution with 95% sand, 2.5% silt, and 2.5% clay. The range of sand fraction in the two replicate measurements for our dune sands was 0.08%, suggesting that deviation in measured grain size distribution should contribute relatively little to model error.

We assumed the initial condition of the dune was nearly dry. However, in the experiment, waves were run in 15-minute increments, and then waves were stopped for at least 45 minutes (and potentially overnight or over a weekend) to allow low frequency energy in the tank to subside before the experiment was continued. During the interim between waves impacting the dune, water would have continued to diffuse. Because of the presence of water from previous runs, our estimate of stability may be too conservative. The dune may have been heavier than we modeled because of the added weight of water from previous runs.

A second assumption was needed to model infiltration based on the Green-Ampt equation, the coefficient to account for the intermittency of swash. Based on the comparison with the full model, $\Lambda = 1.2$. While accurate for our experiment, this coefficient may not be universally applicable; it depends upon both the magnitude of

swash above the dune base, and the frequency of swash. Therefore it is recommended that the dependence of Λ on the characteristics of swash be tested further.

This dune erosion experiment was designed to test existing theories for dune erosion. Because no previous theory included infiltration as a controlling factor on dune stability, water content, pore water pressure, and infiltration were not measured directly. We dealt with the lack of infiltration observations by assuming infiltration was related to erosion. Further experimentation is needed to verify this assumption.

The second component of the dune erosion model, slope stability also required several assumptions. First, it was assumed that the dune scarp was vertical prior to slumping. This suggests that swash zone processes were assumed to remove all of the slumped sediment from the front of the dune, although they were not explicitly modeled. This assumption was based on the observation that slumped material at the dune base was always eroded before the next slump occurred. Including the dune erosion model described here within a swash zone sediment transport model would remove the need for this assumption and allow the full relationship between dune slumping and foreshore dynamics to be modeled.

Because we applied a relatively simple force balance for slope stability, we assumed that the dune was composed of a wetted region of the dune and a dry region of the dune, each with different, homogeneous values water content and pore water pressure. However, the infiltration model suggested that water was not evenly dispersed throughout the wet portion of the dune (Figure 3.14). In fact, infiltration can

be sufficient to reach near saturation conditions at the base of the dune, leading to a loss of cohesive strength and potentially dune collapse. Adopting a more complex slope stability model, for example Morgenstern and Price (1965), would allow the stability of a dune with heterogeneous pore water content to be determined.

Several factors may affect dune erosion under natural conditions that were not addressed in this laboratory experiment. First, the experiment was conducted in an indoor wave flume with an unvegetated dune constructed with earth moving equipment. A natural dune would likely be produced by aeolian transport (although many dunes are rebuilt by bulldozers after storms), and maybe covered with vegetation. The method of dune construction would affect porosity, and thus the rate of infiltration and slope stability. Likewise, vegetation affects both infiltration and slope stability. In a natural setting, dune erosion would likely accompanied by rain, affecting the initial conditions for the infiltration model and slope stability.

Although the laboratory experiment did not include these factors, the infiltration model could account for differences in porosity by changing the sediment characteristics when solving for hydraulic properties with the PTF. The effect of vegetation may also be included in the infiltration and slope stability models. A significant body of literature for including the effects of vegetation exists.

In our experiment, the magnitude of the pressure gradient due to matric suction controlled infiltration. In field conditions, the pressure of waves impacting the dune may be larger than in the wave flume. This effect could easily be modeled by

increasing the pressure acting on the dune face in the infiltration model boundary condition.

Despite the simplifications made in this model, the two basic processes of infiltration and slope stability capture the majority of observed variance in erosion rate. The model could be further extended in two ways. First, we chose to model slope stability at discrete times, every 15 minutes throughout the experiment. By coupling the slope stability and infiltration model, the timing of slumps may be modeled by determining slope stability at higher resolution. Second, we found that eroded volume could be modeled with significant accuracy knowing only cumulative wetting time, and not the actual time series of wave runup. Here we coupled the slope stability model with a simple parameterization for runup. The model may also be coupled with a more complex phase resolving model for runup to force infiltration. Including a swash zone sediment transport model would allow the full feedback between dune, swash and foreshore to be modeled.

3.7 Conclusions

We have developed a simple model for dune erosion by slumping based on two concepts. The first is that water from swash horizontally infiltrates the dune, increasing total weight of the dune and promoting its instability and collapse. Infiltration was modeled using a numerical solution to Darcy's Law for flow through porous media substituted into the continuity equation and known forcing conditions. The second important concept in the model is governance of slope stability by the

force balance on the wetted region of the dune. The dune becomes unstable due to the added weight of water from infiltration. The increased shear strength due to the infiltration of water into the dune causes the dune to slump as a single mass of sediment when the destabilizing forces exceed the stabilizing forces. Finally, the slumped volume is assumed to be transported offshore by swash zone processes.

The model was tested in a large scale laboratory dune erosion experiment using time dependent wave forcing. Error statistics ($R^2 = 0.72$, bias = -0.01 m^3/ m/15 minutes, and RMSE = 0.04 m^3/m/15 minutes) suggest that we capture the majority of the physics controlling dune erosion in this experiment

In order to produce a model for practical application to dune forecasting, two levels of simplifications were explored. The first simplification was replacing the numerical solution for infiltration with Green and Ampt's (1911) equation for infiltration. Error statistics for the simplified model were similar to full model results ($R^2 = 0.71$, bias = -0.02 m^3/ m/15 min, and RMSE = 0.05 m^3/m/15 min), suggesting the simplified model can be applied with as much confidence as the full model.

Finally, the simplified model was tested using forcing from a parameterized runup model given only offshore wave conditions (Stockdon et al. 2006). The parameterized model reproduce the mean and standard deviation of observed swash well ($R^2 = 0.81$ for both the mean and the standard deviation of swash). The increase in error for this model ($R^2 = 0.58$, bias = 0.00 m^3/m/15 min, and RMSE = 0.05 m^3/m/15 min) is caused by use of the parameterized runup model. Still the simplified

model with parameterized forcing explains enough variance to potentially be useful
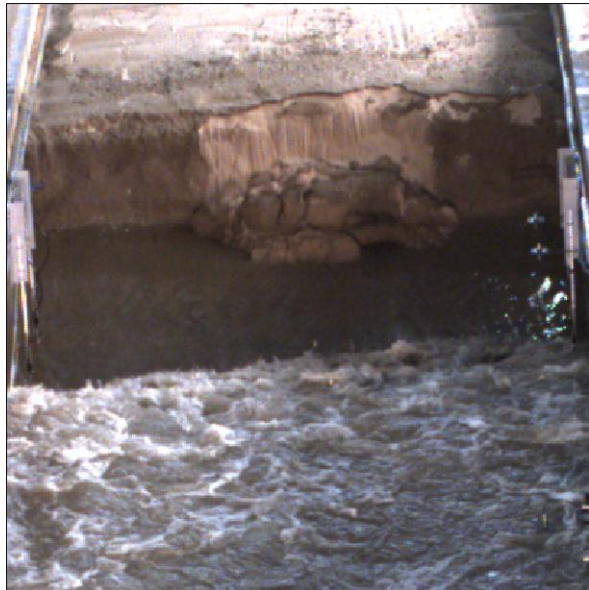
for short and long term predictions of dune erosion.

Figure 3.1   Image of the dune just after a slump occurred. The wet slumped material is visible on the foreshore, along with the dry material on the dune scarp.
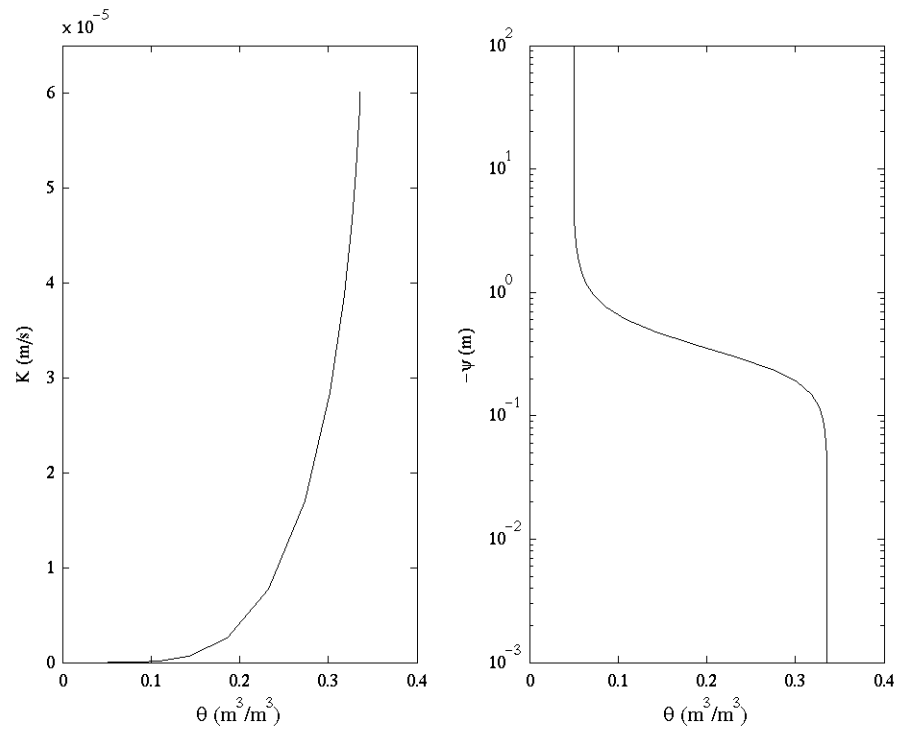
Figure 3.2 Plots of equation (3.5) and (3.6) using the hydraulic properties the Schaap and Leij (2000) PTF.
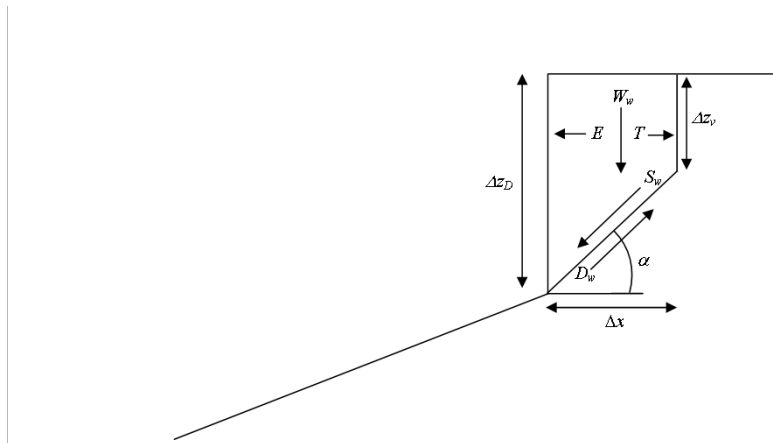
Figure 3.3   Schematic drawing of dune failure including vertical cleavage.
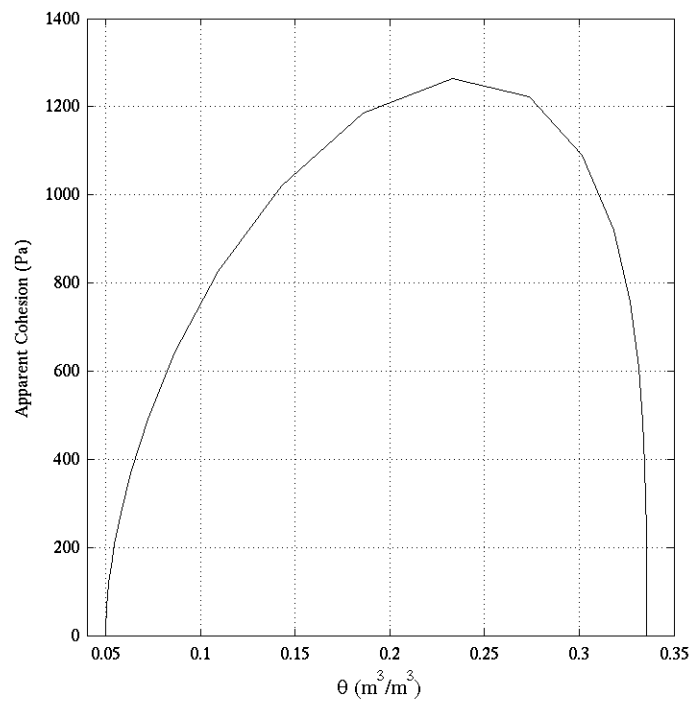
Figure 3.4 Apparent cohesion as a function of water content for the sand used in this experiment. Shear strength of the sediment increases up to 63% saturation, then begins to decrease.
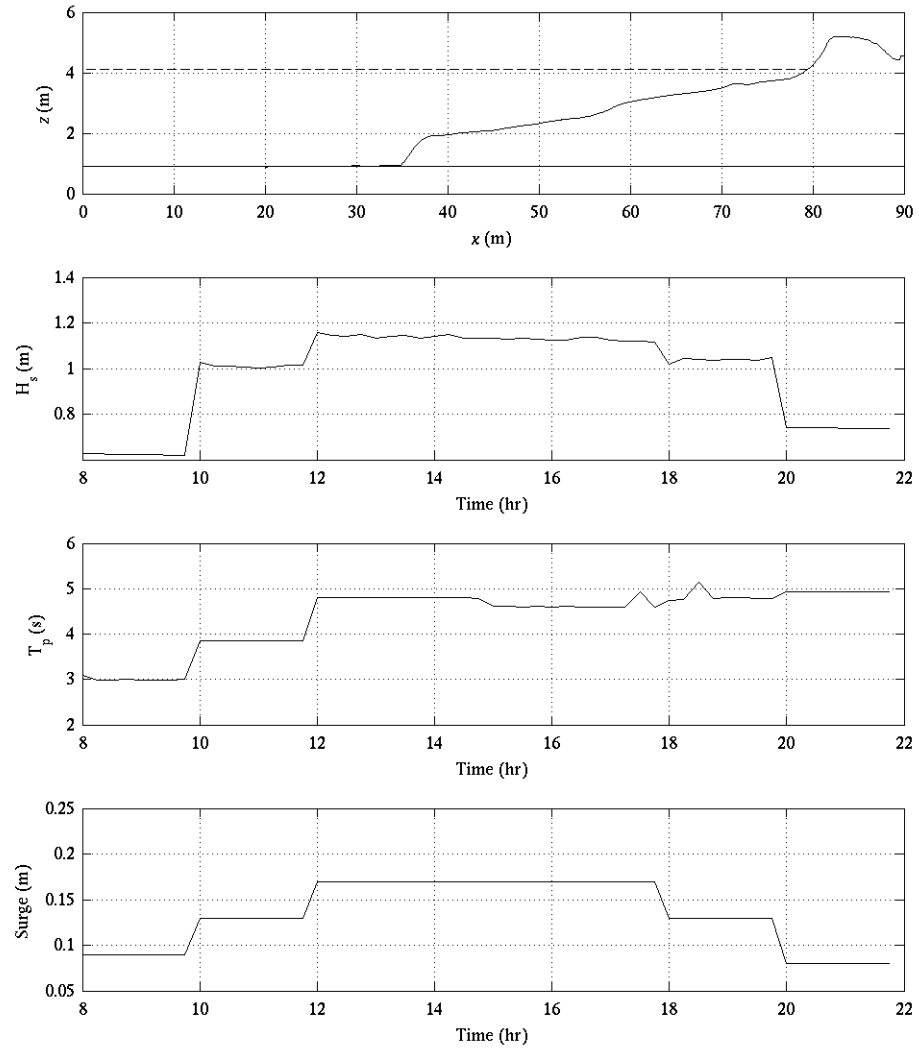
Figure 3.5 Plot of initial beach profile (upper panel), wave height at the wave maker (second panel from top), peak wave period (third panel from top), and surge (lower panel) throughout the experiment.
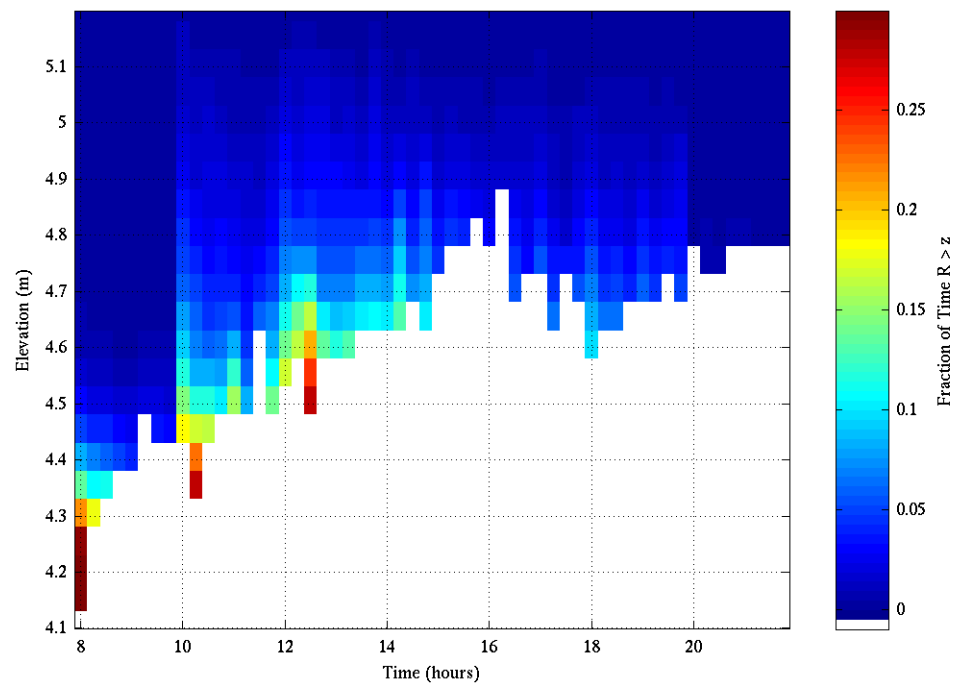
Figure 3.6 Duration that each elevation on the dune was exposed to swash based on video observations of the swash edge. The white region represents regions of the beach below the dune base.
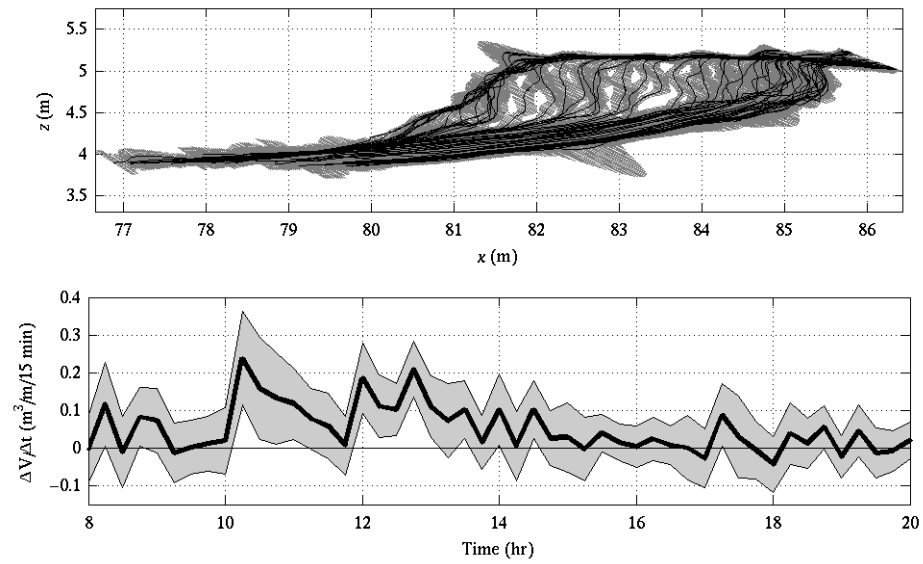
Figure 3.7   Beach profiles with 95% confidence interval derived from stereo observations (upper panel) and observations of sediment flux from the dune with 95% confidence interval (lower panel).
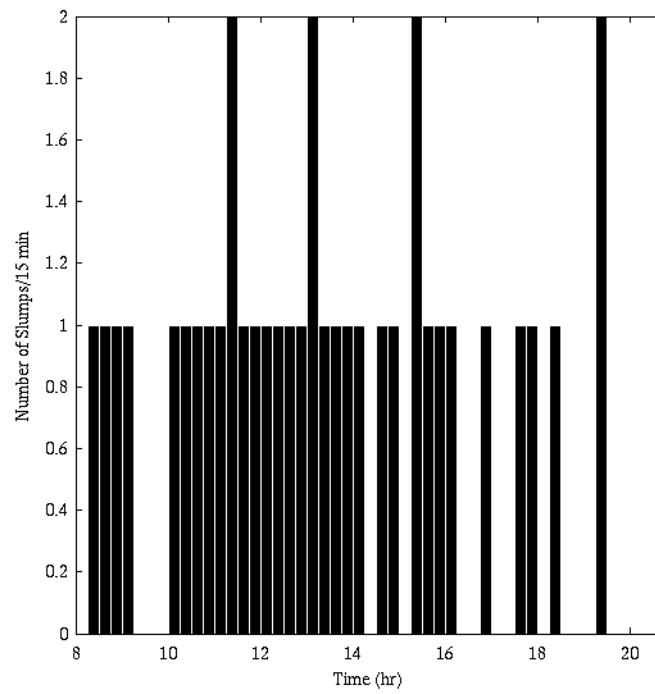
Figure 3.8 Slump frequency for 15 minute intervals throughout the experiment.
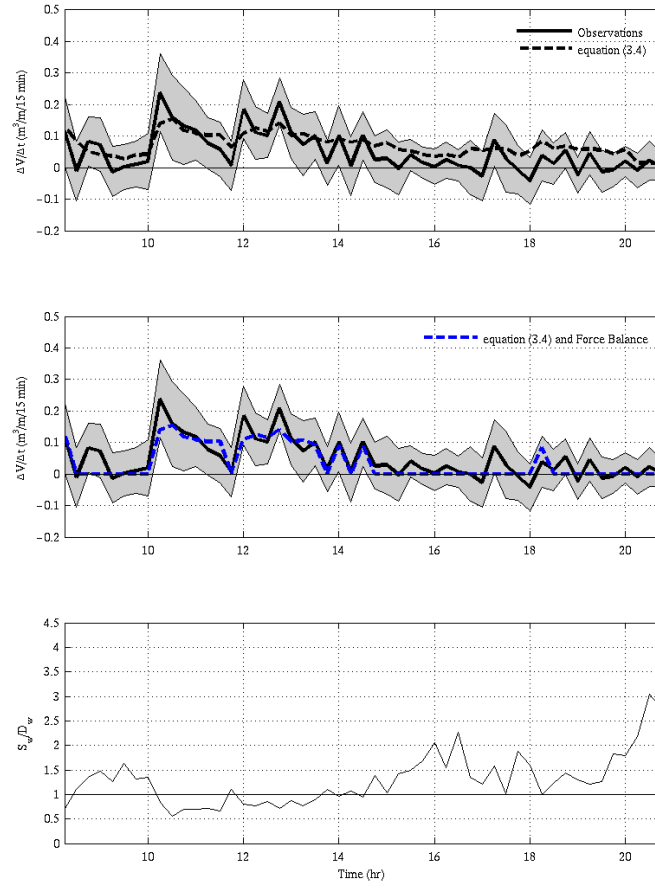
Figure 3.9 Volume of sediment infiltrated using the Richards equation, equation (3.4), and known boundary conditions compared with observed erosion (upper panel), including slope stability (middle panel). Ratio of S_w to D_w throughout the experiment (lower panel).
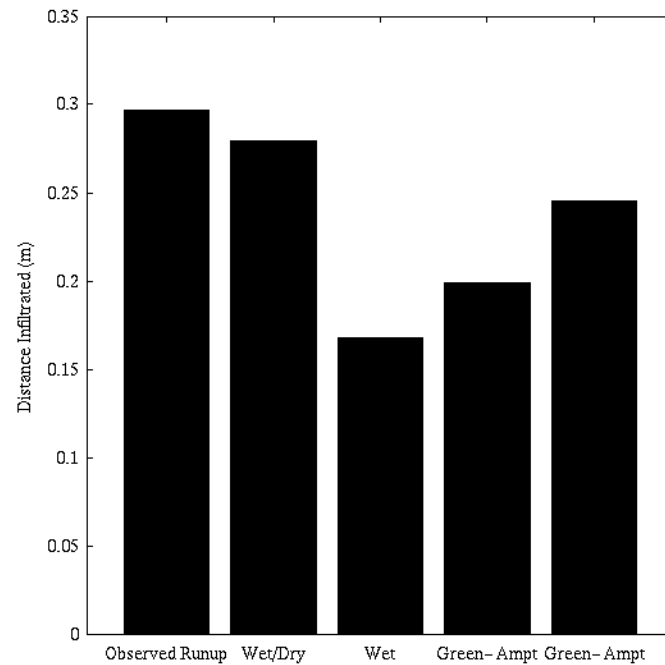
Figure 3.10 Depth of infiltration determined using the Richards equation and known runup conditions (left bar). Depth of infiltration using a boundary condition where the dune is exposed to water continuously for the same period as in known conditions, then the water level is dropped for the remained or the 15 minute period (center left bar). Depth of infiltration when the dune is exposed to water continuously for the same period as in known conditions then the simulation is stopped (center). Depth of infiltration when the dune is exposed for the same period as in known conditions, infiltration is solved for with the Green-Ampt equation, assuming 100% saturation (right bar). Depth of infiltration when the dune is exposed for the same period as in known conditions, infiltration is solved for with the Green-Ampt equation, assuming 70% saturation (right bar).
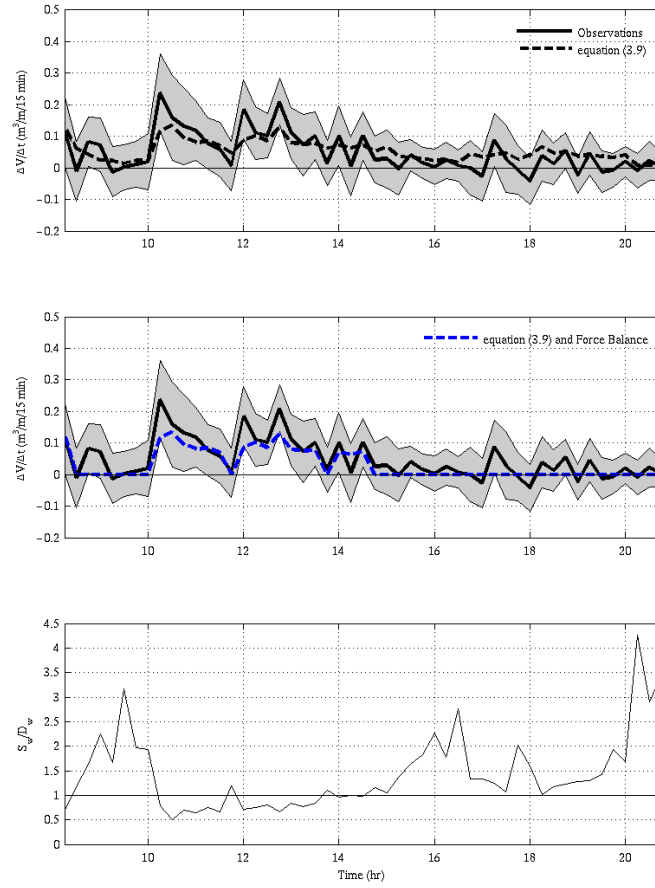
Figure 3.11 Volume of sediment infiltrated using the Green-Ampt equation, equation (3.8), and known boundary conditions compared with observed erosion (upper panel), including slope stability (middle panel). Ratio of S_w to D_w throughout the experiment (lower panel).

Figure 3.12. Mean and standard deviation of swash of swash from equation (3.13) plotted with observations.

Figure 3.13. Volume of sediment infiltrated using the modified Green-Ampt equation, equation (3.9), and boundary conditions from equation (3.13) compared with observed erosion (upper panel), including slope stability (middle panel). Ratio of S_w to D_w throughout the experiment (lower panel).
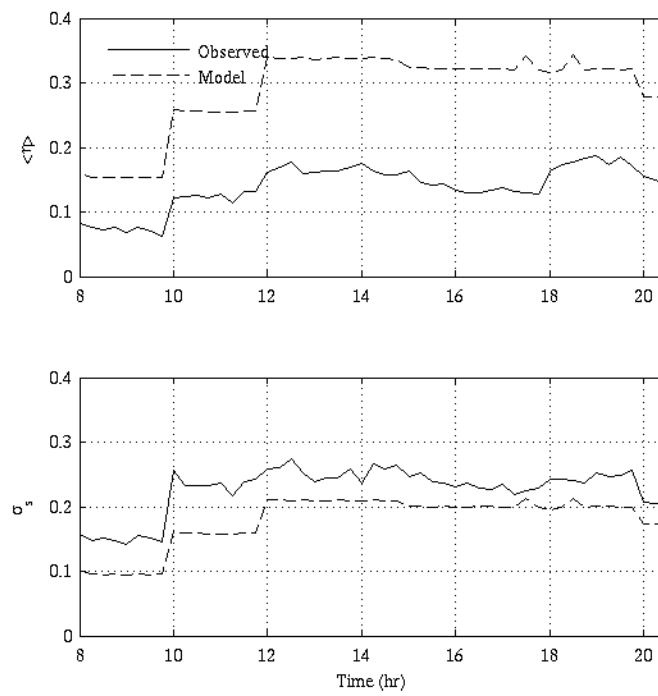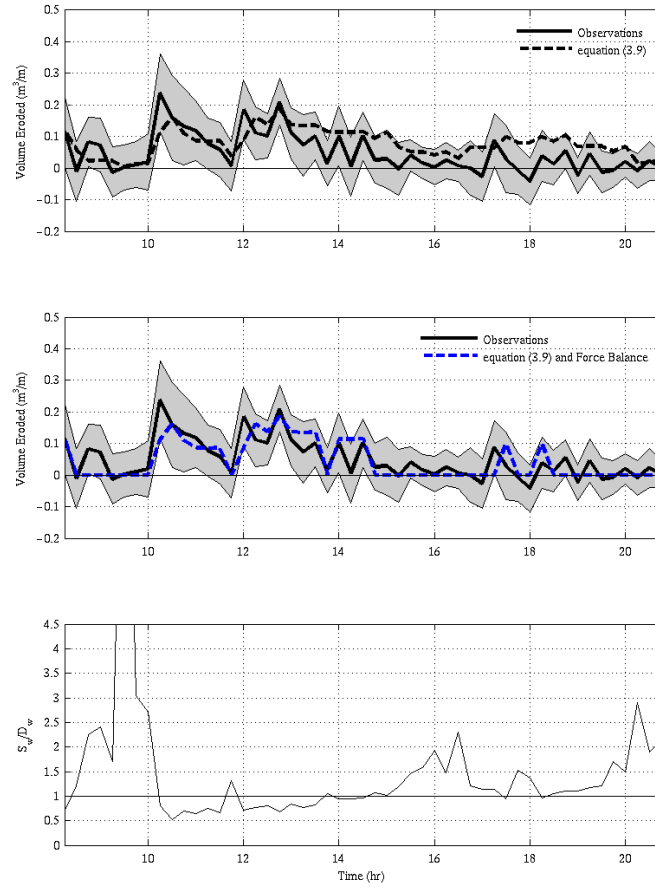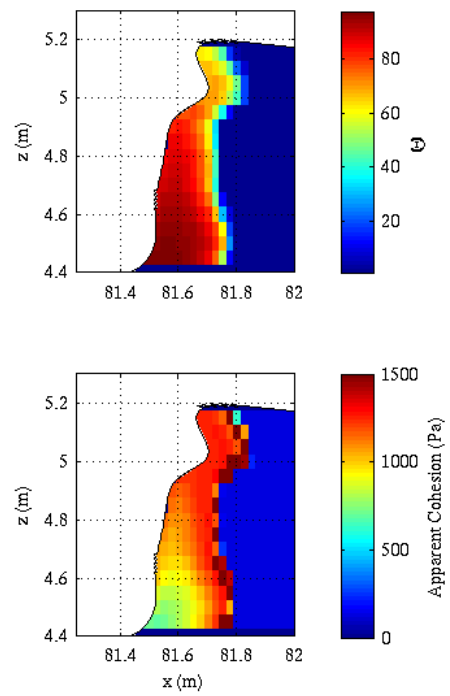
Figure 3.14. Modeled infiltration into the dune suggests that the moisture content was not homogeneous.

4. OPTICAL MEASUREMENTS OF SWASH KINEMATICS

4.1 Abstract

Foreshore bathymetry is known to respond to variations in offshore wave forcing, despite the fact that incident wave heights are typically depth limited in the surf zone, so do not directly represent those wave height variations. In an effort to investigate the nature and dynamics of swash velocity moments under varying wave conditions, we have developed an algorithm for optical measurement of cross-shore swash velocity by exploiting foam traces on waves. The resulting velocities were compared with in situ measurements of swash velocity in the frequency domain. Spectral comparisons of optically derived velocity time series with in-situ velocity measurements showed similar spectral shapes and energies. Coherence between the two times series was high, especially at low frequencies. A time lag identified between velocity records increased towards shore.

4.2 Introduction

Beaches erode during storms and accrete during fair weather. Paradoxically, incident band wave heights in the inner surf zone do not vary between these conditions, since wave height is depth-limited in the surf zone and thus is insensitive to offshore wave conditions. However, previous work has shown that low frequency, infragravity motions become energetic during high-energy periods and these may affect storm-driven sediment transport in the swash zone.

We hypothesize that offshore transport during high energy periods may be the result of offshore-directed swash velocity moments of infragravity motions. Our hypothesis is supported by the in situ measurements of Butt and Russell (1999), where high-energy conditions were associated with negative infragravity skewness and backwash exceeded the sediment transport threshold. During low energy conditions Butt and Russell (1999) observed rapid, turbulent transitions between offshore and onshore flow and advection of sediment onshore.

Our motivation in this work is to develop an understanding of swash velocity moments in an effort to understand swash zone sediment transport. To avoid the complications of traditional swash zone sampling, we have developed a technique for remotely measuring swash velocity, which provides a spatially dense, logistically simple, and non-invasive alternative to in situ measurements of the thin lens of water composing swash. The algorithm will be described, and then applied to optical measurements obtained during infragravity-dominated conditions during the Nearshore Canyon Experiment (NCEX) at La Jolla, CA, USA in Fall 2003. The optically-derived surface cross-shore velocities will be compared with in situ measurements of swash made close to the seabed.

4.3 Algorithm Development

4.3.1 Method

Cross-shore swash velocity was estimated from the movement of foam patterns on breaking waves (Figure 4.1). The bright foam patches act as a tracer,

representative of surface velocity on the breaking wave. The analysis was based on optical image intensity data, collected along a single cross-shore transect of pixels through the swash zone over many video frames. The resulting time stack records the time evolution of cross-shore foam trajectories across the swash zone. The cross-shore transect used in this analysis is shown by the black line through the surf and swash zone in Figure 4.1. The propagation of waves across the cross-shore transect is shown in Figure 4.2. Pixel resolution in the transect is O(0.1 m).

The dominant features in the time stack are the high intensity bore fronts (e.g. Figure 4.2, solid arrow), which progress from the offshore, through the surf zone, until the bore becomes runup on the beach. The slope of these bore front features in the time stack, equivalent to the inverse of the bore front velocity, changes with time as the bore decelerates toward the beach. The other predominant features in the time stack are the trajectories of foam left on the water surface following passage of the bore (Figure 4.2, dashed arrow). Determining the slopes of these foam streaks, equivalent to the inverse of the water velocity, is the central goal of the algorithm described below.

Analysis involves a number of steps. To isolate the foam patch trajectories and reduce the signatures of bores, a band pass filter was applied in the x- direction, passing foam patches with widths of 1 m to 4 m. The cross-shore velocity of any region of foam patches was then calculated from the shift in the cross-shore direction of the foam patches between consecutive samples. A dynamic time warping algorithm

was applied to calculate the movement of foam streaks. This class of algorithm has previously been applied to voice recognition and stereo matching problems (Munich and Perona, 1999) and generates a robust estimate of surface velocity, not influenced by potentially noisy statistics of individual foam patches. A running window, 6.1 m in length, is applied to two consecutive time samples of band-passed image intensity (Figure 4.3, middle panel). Lag correlations between the two consecutive samples are calculated within the window, up to a maximum lag of 0.5 m, which, for the 6 Hz sample rate, is equivalent to allowing a maximum velocity of 3 m/s. The window is shifted to the next pixel in the cross-shore transect and lag correlation for the window at that location is calculated. In this way, lag correlation, R, is calculated for each pixel in the cross-shore transect (Figure 4.3, lower panel). The lag of maximum correlation, D(x,t), is found through the cross-shore transect using the method described by Munich and Perona (1999); white line in the lower panel of Figure 4.3). Cross-shore velocity is then calculated as,

$$u(x,t) = \frac{D(x,t)}{\Delta t} \tag{4.1}$$

where Δt is the time step between samples.

4.3.2 Results

The dynamic time warping algorithm yields a spatially dense measure of cross-shore velocities for the swash and inner surf zone results (Figure 4.4). Cross-shore velocity vectors in Figure 4.4 overlie the time stack of foam traces. High negative

velocities generally align with passage of the bore front. Onshore movement of foam streaks after bore passage matches with negative velocity measurements and positive velocities match with offshore movement of foam tracers. The transition of the foam streaks from onshore movement to offshore movement is associated with 0 m/s velocity.

Velocities near a passing bore are usually biased toward the bore front velocity because the strong bore front signal dominates the correlation window. In Figure 4.4, the width of the bore front is exaggerated from approximately 1 m width in the time stack to the width of the correlation window. This cross-shore shift due to the correlation window causes the bore front to appear to arrive earlier in the velocity record than in the time stack. In addition, time derivatives of foam movements, used to calculate velocity, were computed over 1/6 second frame rates, a process that introduced some high frequency velocity fluctuations, visible in Figure 4.4.

4.4 Comparison with In Situ Data

4.4.1 Field Data

Velocities resulting from the dynamic time warping method were compared with in situ measurements in an effort to validate the algorithm. Video images and in situ measurements were collected October 31, 2006 during the Nearshore Canyon Experiment (NCEX) in La Jolla, CA, USA. The video camera was located on a cliff above the beach overlooking a cross-shore array of 5 quadpods equipped with Acoustic Doppler Velocimeters (ADVs) in the inner-surf and swash zones. Video

images were collected at a rate of 6 Hz and pixel resolution in the vicinity of the

ADVs was approximately 0.1 m. The cross-shore pixel transect (Figure 4.1) used to

generate a time stack (Figure 4.2) was located 3 m north (alongshore) from the ADVs

to avoid influence of the stationary quadpod legs on the optical measurements of

velocity. Assuming shallow water waves and an angle of incidence of less than 20°,

the time lag associated with alongshore nonuniformity will be less than 0.5 s. The

most offshore quadpod (QP5) was located in 0.5 m mean water depth. The two most

onshore quadpods (QP1 and QP2) were frequently subaerially exposed during the

backwash. The in situ velocity time series were collected at 16 Hz, then deglitched to

remove data with low signal to noise ratio and smoothed using 0.5 second moving

window. Velocity was set to 0 m/s during times when the ADVs were not submerged.

4.4.2 Results

The optical and in situ velocity time series data at each cross-shore position were

compared by computing spectra and cross-spectra (Figure 4.5). The results are

qualitatively similar at all cross-shore locations. In situ and optical spectra have

similar structures (Figure 4.5, upper panel), with spectral nodes and anti-nodes at

similar locations, particularly for lower frequencies. Variance is comparable between

0.02 Hz and 0.04 Hz. At higher frequencies, variance is higher for optically measured

velocity.

Coherence–squared values (Figure 4.5, middle panel) are above 0.9 at lower

frequencies and remain significant, although lower, across the entire incident wave

band. Cross-spectral phase values (Figure 4.5, lower panel) show a phase ramp, consistent with a constant time lag between the two time series. The slope of the phase ramp, hence the corresponding time lag between the two series, increases significantly toward shore (Figure 4.6 and Table 4.1).

4.5 Discussion

Observation of a cross-shore variable time lag between the in situ and optically-derived time series has interesting physical consequences. However, three possible causes of lags have been identified. These are due to:

- A vertical gradient in velocity between surface- and near-bed velocities, due to the interaction of an uprush with the previous backwash.

- A constant time lag offset between optical and in situ data logging systems.

- Variable-length drop-outs in the ADV signal associated with the foam in a passing bore front.

To isolate the first potential source of lag, which is of scientific interest, we must resolve the latter two potential sources of lag. The methods and results of this identification are issues of current research and are beyond the scope of this paper.

4.6 Conclusions

A method has been developed for determining cross-shore swash velocities from the statistics of foam trajectories in video imagery. The algorithm relies on the

dynamic time warping approach, previously applied stereo matching and voice recognition problems. The algorithm produced cross-shore velocity estimates with high spatial density but velocity estimates had some contamination associated with bore front passage. Cross-spectral comparisons indicated that the technique works well at low frequencies when compared with in situ measurements. However, a cross-shore variable time lag was identified between the optical and in situ velocity records. The source of the time lag is presently unknown but may be due to vertical structure in the flow resulting from uprush overtaking backwash. Possible contamination due to a lag between measuring systems or drop outs in the ADV record due to passage of the bore front must also be ruled out.

 Figure 4.1 Oblique view of a video frame showing the cross-shore transect used to generate a time stack.
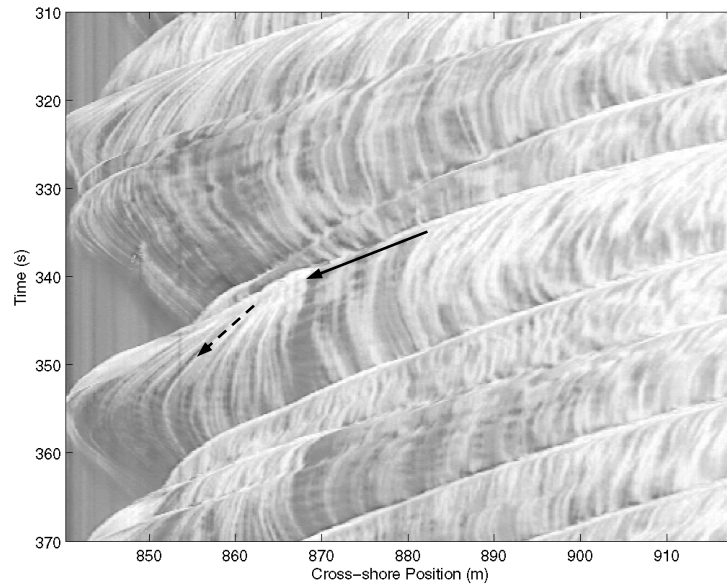
Figure 4.2 A time stack generated from a cross-shore transect of pixels shows the progression of foam streaks in the cross-shore direction. Waves approach the beach from the right side of the time stack, move through the surf and swash zone (solid arrow), then become runup at the left side of the time stack. The slope of the foamy bore front is the inverse of cross-shore celerity. The dashed line identifies an example foam streak trajectory after the bore has passed. The slope of these trajectories correspond to the inverse of the cross-shore water velocity.
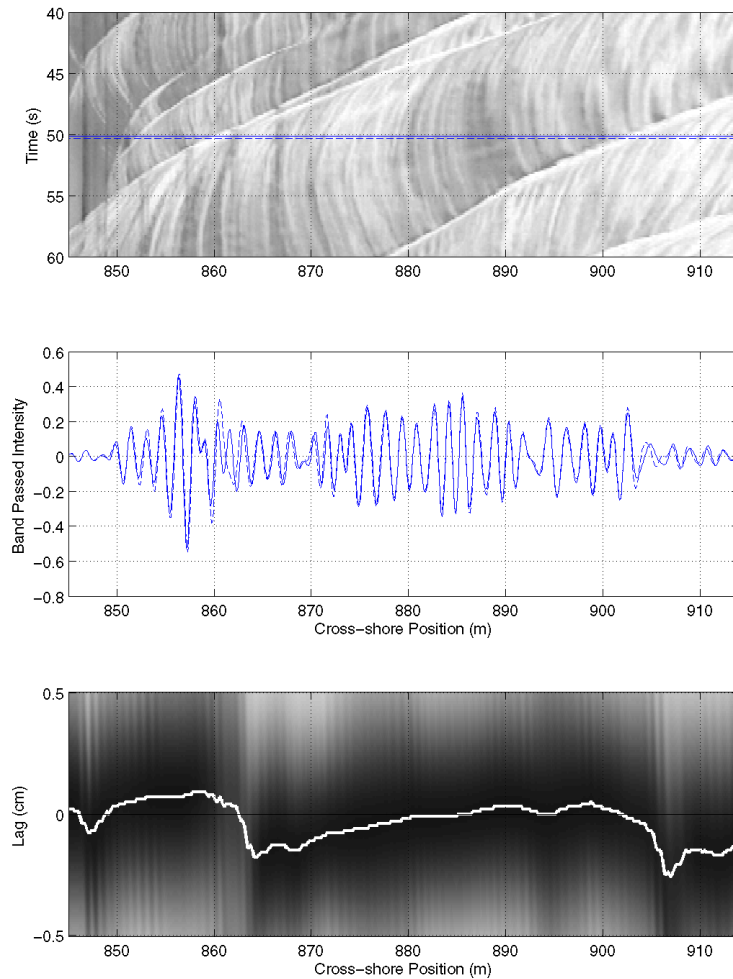
Figure 4.3 (Upper panel) A time stack with foam traces, identifiable as white steaks, moving onshore and offshore in time. Two consecutive time samples are highlighted in solid and dashed lines. (Middle panel) Band passed intensity is plotted for the two time samples shown above. An example of the running window is plotted in the black box. Onshore movement of foam occurred where the dashed line is onshore of the solid line and offshore movement occurred where the solid line is onshore of the dashed line. (Lower panel) Lag correlation is computed for the 6 m running window at each pixel location in the cross-shore transect. Darker colors indicate higher correlation. The path of maximum correlation through the transect is plotted in white.
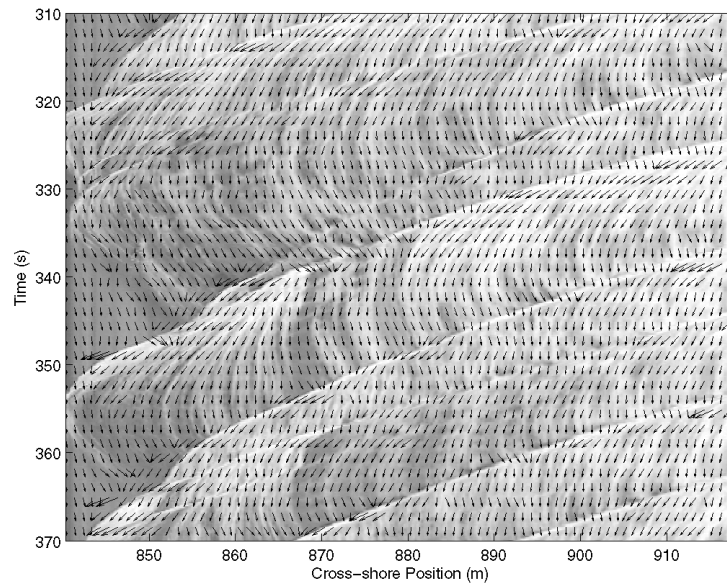
Figure 4.4 Cross-shore velocity vectors are overlain on the image intensity time stack.
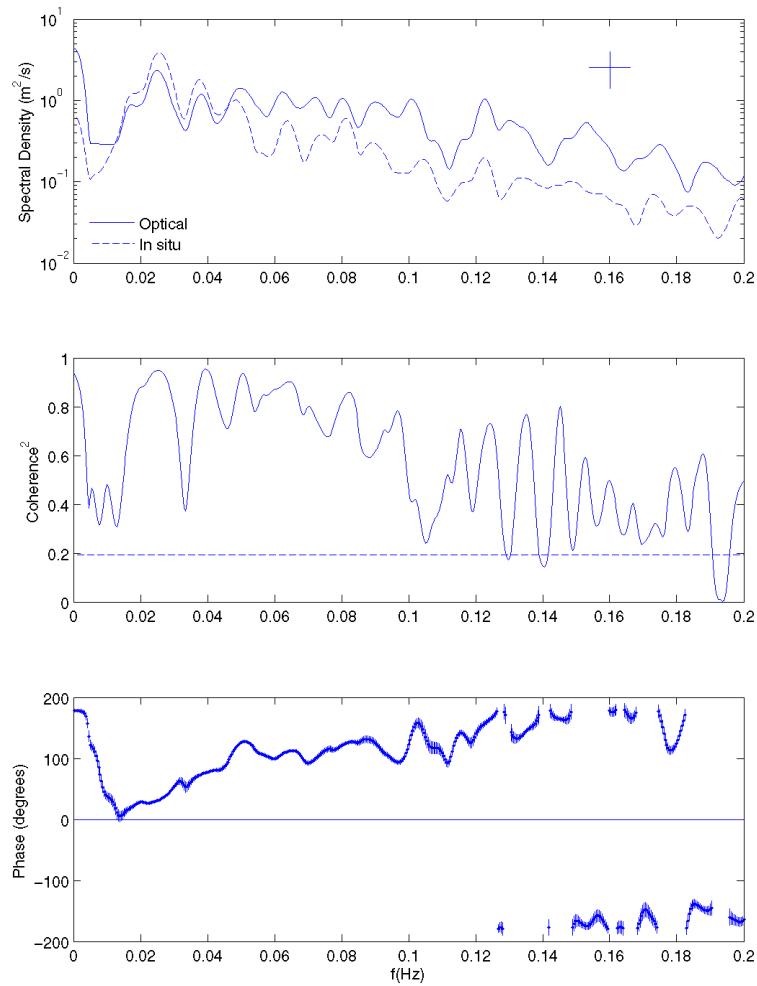
Figure 4.5 (Upper panel) Spectral structures of the optical and in situ velocity time series are similar at the mid-swash position. Variance of the time series is similar at lower frequencies but variance of the optical velocity time series is greater at higher frequencies. A phase ramp indicates a constant time lag between the optical and in situ velocity time series. Phase is plotted with the 95 % confidence interval for frequencies with significant coherence squared.

Figure 4.6 Cross-spectral phase plots for each of the five locations of the in-situ instruments, from landward-most (upper panel) to seaward-most (lower panel). The slope of the phase ramp decreases off shore.

Table 4.1 Time lag associated with phase ramp at each quadpod

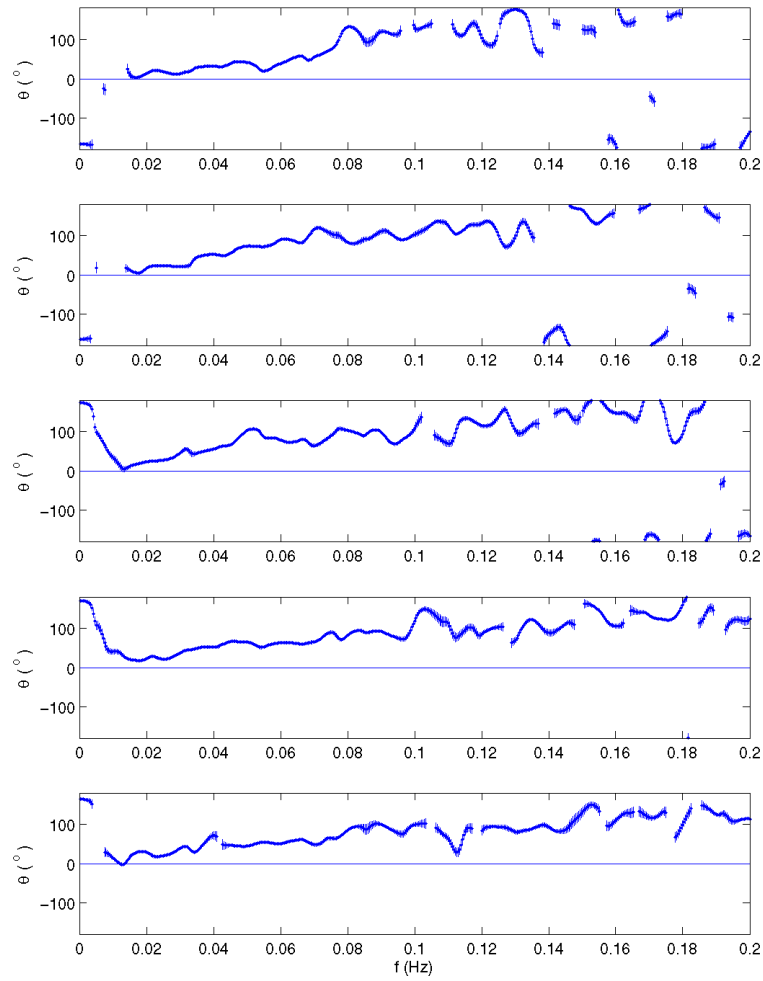| Quadpod	1	2	3	4	5
Lag (s)	5.3	6.1	4.1	2.3	2

5. Conclusions

The overarching goal of this dissertation was to improve our understanding of dune erosion, resulting in the two specific objectives of this dissertation. Limitations in prior datasets were addressed through the development of new methodologies for studying processes on the dune and foreshore. The new methodologies were applied to improve understanding of the processes driving dune erosion and develop new models for predicting dune vulnerability.

The new techniques for studying dune sediment transport and swash zone kinematics are described in Chapters 2 and 4. Both depend on optical remote sensing, a relatively inexpensive and nonintrusive tool that has been developed at the Coastal Imaging Lab at Oregon State University over the last three decades. To improve the temporal and spatial resolution of dune erosion observations, which typically do not capture slump events, we implemented a stereo video method. The technique depends upon matching similar features in two images collected from a pair of cameras. The matching technique was based on a two-step process. First, the images were lag-correlated, then a dynamic programming algorithm (Sun, 2002b) was applied to find the continuous beach surface. Finally, the 3-dimensional location of the dune was determined using established stereo techniques (Hartley and Zisserman, 2004). Resolution of the stereo technique was 0.1 m in the horizontal and 0.04 m in the vertical, and errors in stereo observations were on the order of 0.02m to 0.08 m (1 to 2 pixels) when compared with surveys. We developed a new method for defining

confidence intervals in 3-dimensional space in terms of the curvature of the lag-correlation coefficient relationship at each pixel. 98 % of error bars parameterized scatter to within +/-2 standard deviations of the observed scatter about temporal mean of the stationary dune surface, and 62% of the error bars fell within +/-1 standard deviations of the observed scatter, roughly consistent with a standard normal distribution.

A method for determining cross-shore swash velocities from the statistics of foam trajectories in video imagery was also developed. A lag correlation and dynamic programming algorithm, similar in concept to the stereo matching algorithm, was applied to track the foam. The technique produced velocity estimates with high spatial density compared to traditional in situ point measurements. Coherence-squared between video-derived velocities was 0.9 over the energetic band. A time lag was observed between the video and in situ measurements. However, the source is presently unknown. It may be due to vertical structure in the flow resulting from uprush overtaking and overtopping backwash. Other possible explanations are contamination due to an offset between measuring systems or drop outs in the ADV record due to passage of the bore front.

New observations of dune erosion from the stereo video technique along with observations of wave runup on dunes were used to evaluate a simple model for dune erosion (Larson et al, 2004) in a large scale laboratory experiment. The Larson model was based on the concept that the impact force of waves on the dune face is

proportional to the volume of sediment eroded from the dune. Impact force is represented by combining the magnitude of extreme runup with number of swash impacts on the dune and is assumed to be linearly proportional to the eroded volume.

The model was modified from its original form in two ways. First, based on observations of wave runup on dunes, we determined that R_{16}, the 16% exceedance value of runup, was the most appropriate statistic for quantifying dune erosion, less extreme than the normally-accepted 2% exceedance value, R_2 used in the original model. The model, forced with observed R_{16} and the number of collisions, successfully reproduced 64% of the observed variance (bias = 0.03 m^3/m/15 min, rmse = 0.05 m^3/m/15 min).

Next, we modified the runup equation by Stockdon et al. (2006) to estimate R_{16} based on offshore wave forcing, and proposed a new approximation for the number of swash impacts on the dune, based on Stockdon et al.'s equation. We determined that the appropriate beach slope for parameterizing R_{16} on dunes was defined using a regression over cross shore region defined by +/- 1 standard deviations of swash about the mean water level. In the absence of knowing the time dependent beach slope, a constant beach slope, based on the initial beach slope, defined by a regression between the still water level and the dune base was also a reasonable choice. Given only offshore forcing and a dune base retreat trajectory that was 0.54 of the initial beach slope, the model reproduced 55% (bias = 0.00 m^3/m/15 min, rmse = 0.05 m^3/m/15 min) of the observed variance using parameterized offshore forcing and the total dune

base retreat over the entire experiment was determined to within 7% of the observed retreat.

A new dune erosion model was developed in Chapter 3, based on the same observations of dune erosion described in Chapter 2. In this model the dune becomes unstable due to the added weight of water from infiltrated swash. The increased shear strength due to the horizontal infiltration of swash into the dune causes the dune to slump as a single mass of sediment. Infiltration was modeled using a numerical solution to Darcy's Law for flow through porous media substituted into the continuity equation and was driven by the observed runup on the dune. Slope stability was determined from the balance of resisting and destabilizing forces on the dune. Shear strength of the sediment along the failure plane and tensile strength at the intersection between the infiltrated and uninfiltrated portion of the dune provided resistance to slumping, while the weight of sediment above the plane of failure and the lateral earth force acted to destabilize the potential sliding block. The new model explained 72% of the observed variance in erosion rate (bias = -0.01 $\mathrm{m^3/m/15}$ min, rmse = 0.04 $\mathrm{m^3/m/15}$ min).

A simplified equation for infiltration (Green and Ampt, 1911) was also tested with known forcing, representing the intermittent wetting of the full model in terms of constant exposure for the equivalent cumulative wetting time. The simplified model required introduction of an empirical coefficient to account for continuing diffusion of water into the dune that would have occurred between waves. This coefficient was

calibrated by comparing infiltration distance from the full model solution to

infiltration from the simplified solution. The simplified model reproduced 71% of the

observed variance (bias = -0.02 m^3/m/15 min, rmse = 0.05 m^3/m/15 min).

Finally, the simplified model was applied using offshore forcing to determine

runup at the dune based on the Stockdon et al. (2006) equation for runup. Although

the Stockdon el al. (2006) equation was not based on swash interacting with dunes, it

explained 81% of the observed variance in mean water level (bias = 0.14 m, rmse =

0.14 m) and standard deviation of swash (bias = -0.05 m, rmse = 0.06 m). With

offshore forcing, the model explained 58% of the observed variance (bias = 0.00

m^3/m/15 min, rmse = 0.05 m^3/m/15 min). Because this simplified model only requires

offshore wave conditions, it is useful for practical application to forecast dune erosion.

Although Larson et al. (2004) takes a more parameterized approach to

modeling dune erosion, there is a key link between Larson et al. (2004) tested in

Chapter 2 and the new model described in Chapter 3. Both models depend strongly on

the duration of dune exposure to waves either directly as in Larson et al. (2004) or as

the square root in Green and Ampt (1911). In fact, regression of erosion against the

observed time of exposure alone explains 53% of the observed variance in erosion

rate. Previous field experiments have also found a relationship between duration of

exposure and erosion rate (Pye and Blott, 2008; Ruggiero et al., 2001) Here, we have

shown that this dependence on time of exposure is due to the infiltration of water into

the dune resulting in added weight and changes to shear strength of the dune, ultimately resulting in slumping.

This link between duration of exposure and erosion rate suggests that forecasts of erosion may be produced if duration of exposure can be forecast. The new observations of runup on dunes led to extensive testing of the Stockdon et al. (2006) equation as a means to transform offshore wave conditions to the duration of dune exposure to waves, extending the equation beyond its original purpose. This statistical approach could be developed further by investigating higher moments of runup distributions.

Finally, shear strength of sediment was shown to be a significant factor in dune erosion. Based on these findings, the loss of shear strength may play a role in dune undercutting as the dune base nears saturation. Further extending the idea that shear strength may influence beach morphology, it is possible that the added shear strength due to unsaturated sediments on the foreshore may play a role in critical shear stress necessary for sediment transport on the beach seaward of the dune. Therefore, continued investigation of shear strength variability due to infiltration may provide a key to understanding swash zone sediment transport.

Bibliography

Butt, T. and Russell, P., 1999. Suspended sediment transport mechanisms in high-energy swash. Marine Geology, 161: 361-375.

Committee to Assess the U.S. Army Corps of Engineers Water Resources Project Planning Procedures, 1999. New directions in water resources planning for the us army corps of engineers, National Research Council, Washington, DC.

Dean, R.G. and Dalrymple, R.A., 2002. Coastal processes with engineering applications. Cambridge University Press, Cambridge, UK.

Dette, H.H. et al., 2002. Application of prototype flume tests for beach nourishment assessment. Coastal Engineering, 47(2): 137-177.

Edelman, T., 1968. Dune erosion during storm conditions. Proceedings of the 11th Conference on Coastal Engineering, London, p.^pp. 719-722.

Edelman, T., 1972. Dune erosion during storm conditions. Proceedings of the 13th Conference on Coastal Engineering, Vancouver, p.^pp. 1305-1311.

Egnal, G., Mintz, M. and Wildes, R.P., 2004. A stereo confidence metric using single view imagery with comparison to five alternative approaches. Image and Vision Computing, 22(12): 943-957.

Erikson, L.H., Larson, M. and Hanson, H., 2007. Laboratory investigation of beach scarp and dune recession due to notching and subsequent failure. Marine Geology, 245(1-4): 1-19.

Fisher, J.S., Overton, M.F. and Chisholm, T., 1986. Field measurements of dune erosion. 20th International Conference on Coastal Engineering, Taipei, Taiwan, p.^pp. 1107-1115.

Graham, N.E. and Diaz, H.F., 2001. Evidence for intensification of north pacific winter cyclones since 1948. Bulletin of the American Meteorological Society, 82: 1869-1893.

Green, W.H. and Ampt, G.A., 1911. Studies on soil physics part i - the flow of air and water through soils. Journal of Agricultural Science, 4(1): 1-24.

Hartley, R.I. and Zisserman, A., 2004. Multiple view geometry in computer vision. Cambridge University Press, Cambridge.

Holland, K.T. and Holman, R., 1997. Video estimation of foreshore topography using trinocular stereo. Journal of Coastal Research, 13(1): 81-87.

Holman, R.A. and Stanley, J., 2007. The history and technical capabilities of argus. Coastal Engineering, 54(6-7): 477-491.

Hornbaker, D.J., Albert, R., Albert, I., Barabasi, A.L. and Schiffer, P., 1997. What keeps sandcastles standing? Nature, 387(6635): 765-765.

IPCC, 2007. Climate change 2007: The physical science basis, Cambridge University Press, Cambridge, United Kingdom.

Kriebel, D.L. and Dean, R.G., 1985. Numerical simulation of time-dependent beach and dune erosion. Coastal Engineering, 9(3): 221-245.

Larson, M., Erikson, L. and Hanson, H., 2004. An analytical model to predict dune erosion due to wave impact. Coastal Engineering, 51(8-9): 675-696.

Larson, M. and Kraus, N.C., 1989. Sbeach: Numerical model for simulating storm induced beach change, Army Corps of Engineers Coastal Engineering Research Center, Vicksburg, MS.

Lohnes, R.A. and Handy, R.L., 1968. Slope angles in friable loess. The Journal of Geology, 76(3): 247-258.

Lu, N., Kim, T.-H., Sture, S. and Likos, W.J., 2009. Tensile strength of unsaturated sand. Journal of Engineering Mechanics, 135(12): 1410-1419.

Martínez, M. and Psuty, N., 2004. Coastal dunes: Ecology and conservation. Springer.

McCarthy, D., 2007. Essentials of soil mechanics and foundations: Basic geotechnics. Pearson/Prentice Hall.

Morgenstern, N.R. and Price, V.E., 1965. The analysis of the stability of general slip surfaces. Géotechnique, 15(1): 79-93.

Munich, M.E. and Perona, P., 1999. Continuous dynamic time warping for translation-invariant curve alignment with applications to signature verification. Proceedings of 7th International Conference on Computer Vision, p.^pp.

Overton, M.F. and Fisher, J.S., 1988. Simulation modeling of dune erosion. International Conference on Coastal Engineering, Costa del Sol-Malaga, Spain, p.^pp. 1857-1867.

Overton, M.F., Fisher, J.S. and Hwang, K.N., 1994a. Development of a dune erosion model using supertank data. Proceedings of the Twenty-Fourth International Conference on Coastal Engineering, Kobe Japan, p.^pp. 2488-2502.

Overton, M.F., Pratikto, W.A., Lu, J.C. and Fisher, J.S., 1994b. Laboratory investigation of dune erosion as a function of sand grain-size and dune density. Coastal Engineering, 23(1-2): 151-165.

Palmsten, M. and Holman, R., in review. Laboratory investigation of dune erosion using stereo video. Coastal Engineering.

Plant, N.G., Holland, K.T. and Puleo, J.A., 2002. Analysis of the scale of errors in nearshore bathymetric data. Marine Geology, 191(1-2): 71-86.

Pye, K. and Blott, S.J., 2008. Decadal-scale variation in dune erosion and accretion rates: An investigation of the significance of changing storm tide frequency and magnitude on the sefton coast, uk. Geomorphology, 102(3-4): 652-666.

Rawls, W.J. and Brakensiek, D.L., 1985. Prediction of soil water properties for hydrologic modeling. Proceeding of the Symposium of Watershed Management in the Eighties, New York, NY, p.^pp.

Richards, L.A., 1931. Capillary conduction of liquids through poruous media. Physics, 1(5): 318 - 333.

Roelvink, D. et al., 2009a. Modeling storm impacts on beaches, dunes and barrier islands. Coastal Engineering, submitted.

Roelvink, D. et al., 2009b. Modelling storm impacts on beaches, dunes and barrier islands. Coastal Engineering, 56(11-12): 1133-1152.

Ruggiero, P., Komar, P.D. and Allan, J.C., 2010. Increasing wave heights and extreme value projections: The wave climate of the u.S. Pacific northwest. Coastal Engineering, 57(5): 539-552.

Ruggiero, P., Komar, P.D., McDougal, W.G., Marra, J.J. and Beach, R.A., 2001. Wave runup, extreme water levels and the erosion of properties backing beaches. Journal of Coastal Research, 17(2): 407-419.

Sallenger, A., 2009. Island in a storm: A rising sea, a vanishing coast, and a nineteenth-century disaster that warns of a warmer world. PublicAffairs.

Sallenger, A.H., Jr, 2000. Impact scale for barrier islands. Journal of Coastal Research, 16(3): 890-895.

Schaap, M.G. and Leij, F.J., 2000. Improved prediction of unsaturated hydraulic conductivity with the mualem-van genuchten model. Soil Sci Soc Am J, 64(3): 843-851.

Šimůnek, J., Genuchten, M.T.v. and Šejna, M., 2005. The hydrus-1d software package for simulating the movement of water, heat, and multiple solutes in variably saturated media, version 3.0, *hydrus software series 1*, Department of Environmental Sciences, University of California Riverside, Riverside, California, USA.

Steetzel, H.J., 1993. Cross-shore transport during storm surges, Delft Hydraulics, Delft, The Netherlands.

Stockdon, H.F., Holman, R.A., Howd, P.A. and Sallenger, A.H., 2006. Empirical parameterization of setup, swash, and runup. Coastal Engineering, 53(7): 573-588.

Stockdon, H.F., Sallenger, J.A.H., Holman, R.A. and Howd, P.A., 2007. A simple model for the spatially-variable coastal response to hurricanes. Marine Geology, 238(1-4): 1-20.

Sun, C., 2002a. Fast optical flow using 3d shortest path techniques. Image and Vision Computing, 20(13-14): 981-991.

Sun, C., 2002b. Fast stereo matching using rectangular subregioning and 3d maximum-surface techniques. International Journal of Computer Vision, 47(1): 99-117.

Symonds, G. and Bowen, A., 1984. Interactions of nearshore bars with incoming wave groups. Journal of Geophysical Research, 89(c2): 1953-1959.

Terzaghi, K. and Peck, R., 1967. Soil mechanics in engineering practice. John Wiley and Sons, New York, NY, 729 pp.

van Gent, M.R.A., van Thiel de Vries, J.S.M., Coeveld, E.M., de Vroeg, J.H. and van de Graaff, J., 2008. Large-scale dune erosion tests to study the influence of wave periods. Coastal Engineering, 55(12): 1041-1051.

van Genuchten, R., 1980. A closed-form equation for predicting the hydraulic conductivity of unstaurated soils. Soil Sci Soc Am J, 44(5): 892-898.

van Rijn, L.C., 2009. Prediction of dune erosion due to storms. Coastal Engineering, 56(4): 441-457.

van Thiel de Vries, J.S.M., van Gent, M.R.A., Walstra, D.J.R. and Reniers, A.J.H.M., 2008. Analysis of dune erosion processes in large-scale flume experiments. Coastal Engineering, 55(12): 1028-1040.

Vanapalli, S.K., Fredlund, D.G., Pufahl, D.E. and Clifton, A.W., 1996. Model for the prediction of shear strength with respect to soil suction. Can. Geotech. J., 33(3): 379-392.

Vellinga, P., 1986. Beach and dune erosion during storm surges, Delft University of Technology, Delft.

Vereecken, H., Maes, J. and Feyen, J., 1990. Estimating unsaturated hydraulic conductivity from easily measured soil properties. Soil Science, 149(1): 1-12.

Wösten, J.H.M., Pachepsky, Y.A. and Rawls, W.J., 2001. Pedotransfer functions: Bridging the gap between available basic soil data and missing soil hydraulic characteristics. Journal of Hydrology, 251(3-4): 123-150.